

One Model to Rule them All: Towards Universal Segmentation for Medical Images with Text Prompts

Ziheng Zhao^{1,2}, Yao Zhang², Chaoyi Wu^{1,2}, Xiaoman Zhang^{1,2},
Xiao Zhou², Ya Zhang^{1,2}, Yanfeng Wang^{1,2,†} and Weidi Xie^{1,2,†}

¹Shanghai Jiao Tong University

²Shanghai AI Laboratory

Abstract. In this study, we aim to build up a model that can **Segment Anything** in radiology scans, driven by medical terminologies as **Text prompts**, termed as **SAT**. Our main contributions are three folds: (i) for dataset construction, we construct the first multi-modal knowledge tree on human anatomy, including **6502 anatomical terminologies**; Then, we build up the largest and most comprehensive segmentation dataset for training, by collecting over **22K 3D medical image scans** from **72 segmentation datasets**, across **497 classes**, with careful standardization on both image scans and label space; (ii) for architecture design, we propose to inject medical knowledge into a text encoder via contrastive learning, and then formulate a universal segmentation model, that can be prompted by feeding in medical terminologies in text form; (iii) As a result, we have trained **SAT-Nano** (110M parameters) and **SAT-Pro** (447M parameters), demonstrating superior or comparable performance to **72 specialist models**, *i.e.*, nnU-Nets, U-Mamba or SwinUNETR, trained on each dataset/subsets. We validate SAT as a foundational segmentation model, with better generalization on external (cross-center) datasets, and can be further improved on specific tasks after fine-tuning adaptation. Comparing with state-of-the-art interactive segmentation model MedSAM, SAT demonstrate superior performance, scalability and robustness. We further compare SAT with BiomedParse, another concurrent work of text-prompted universal segmentation model, and observe SAT is significantly superior in both internal and external evaluation. Through extensive ablation study, we validate the benefit of domain knowledge on universal segmentation, especially on tail categories. As a use case, we demonstrate that SAT can act as a powerful out-of-the-box agent for large language models, enabling visual grounding in versatile application scenarios. All the data, codes, and models in this work have been released.

Contents

1	Introduction	2
2	Results	5
2.1	Comparison with Specialist Models on Automatic Segmentation	6
2.2	Comparison with Interactive Universal Segmentation Model	6
2.3	Compare with Text-Prompted Universal Segmentation Model	9
2.4	Evaluation on External Datasets.	9
2.5	Ablation Study	10
2.5.1	Effect of Visual Backbone	11
2.5.2	Effect of Text Encoder	12
2.6	Qualitative Results – SAT as an Interface Between Language and Segmentation	14
3	Discussion	14
4	Method	17
4.1	Dataset Construction	17

† Corresponding Authors.

4.1.1	Domain Knowledge	17
4.1.2	Segmentation Dataset	18
4.2	Universal Segmentation Prompted by Text	20
4.2.1	Problem Formulation	20
4.2.2	Multimodal Knowledge Injection	20
4.2.3	Universal Segmentation Training	22
4.3	Implement Details	23
4.4	Evaluation Settings	24
4.4.1	Evaluation Datasets	24
4.4.2	Baseline	24
4.4.3	Evaluation Protocols	25
4.4.4	Evaluation Metrics	25
5	Conclusion	26
6	Code Availability	26
7	Data Availability of SAT-DS	26
8	Appendix	37
8.1	More Results in Internal Evaluation	37
8.2	More Results in External Evaluation	48
8.3	More Results in Ablation Study	51
8.4	Detailed Architecture of Specialist Models	59
8.5	All classes in SAT-DS	61
8.6	Dataset Details of SAT-DS	65
8.7	Examples From the Knowledge Tree	67

1 Introduction

Medical image segmentation aims to identify and delineate regions of interest (ROIs) like organs, lesions, and tissues in diverse medical images, which plays a crucial role in numerous clinical applications, such as disease diagnosis, treatment planning, and disease progression tracking [93, 100, 7, 67, 27], as well as in medical researches [65, 6]. Traditionally, radiologists perform manual segmentation to measure volume, shape, and location in a slice-wise manner, which is both time-consuming and challenging to scale with the growing volume of medical data. Consequently, there is a pressing need for automated and robust medical image segmentation methods in clinical settings, to enhance efficiency and scalability.

Recent advancements in medical image analysis have been marked by a surge of deep learning. These developments have yielded a spectrum of segmentation models, each trained for specific tasks [59, 58, 4, 68, 7, 23, 57], often referred to as ‘specialist’ models. While these models demonstrate impressive segmentation capabilities, their major drawback lies in the narrow specialization. Designed and optimized for distinct ROIs and imaging modalities, these models [56, 20, 26, 63, 81, 18] require distinct preprocessing methods for each dataset. As a result, they often fall short in diverse and dynamic clinical environments, where adaptability to new conditions and imaging techniques is essential.

There is a growing interest in developing universal models for medical image segmentation [55, 25], by adapting the pre-trained Segment Anything Model (SAM) [34] models from the computer vision community. However,

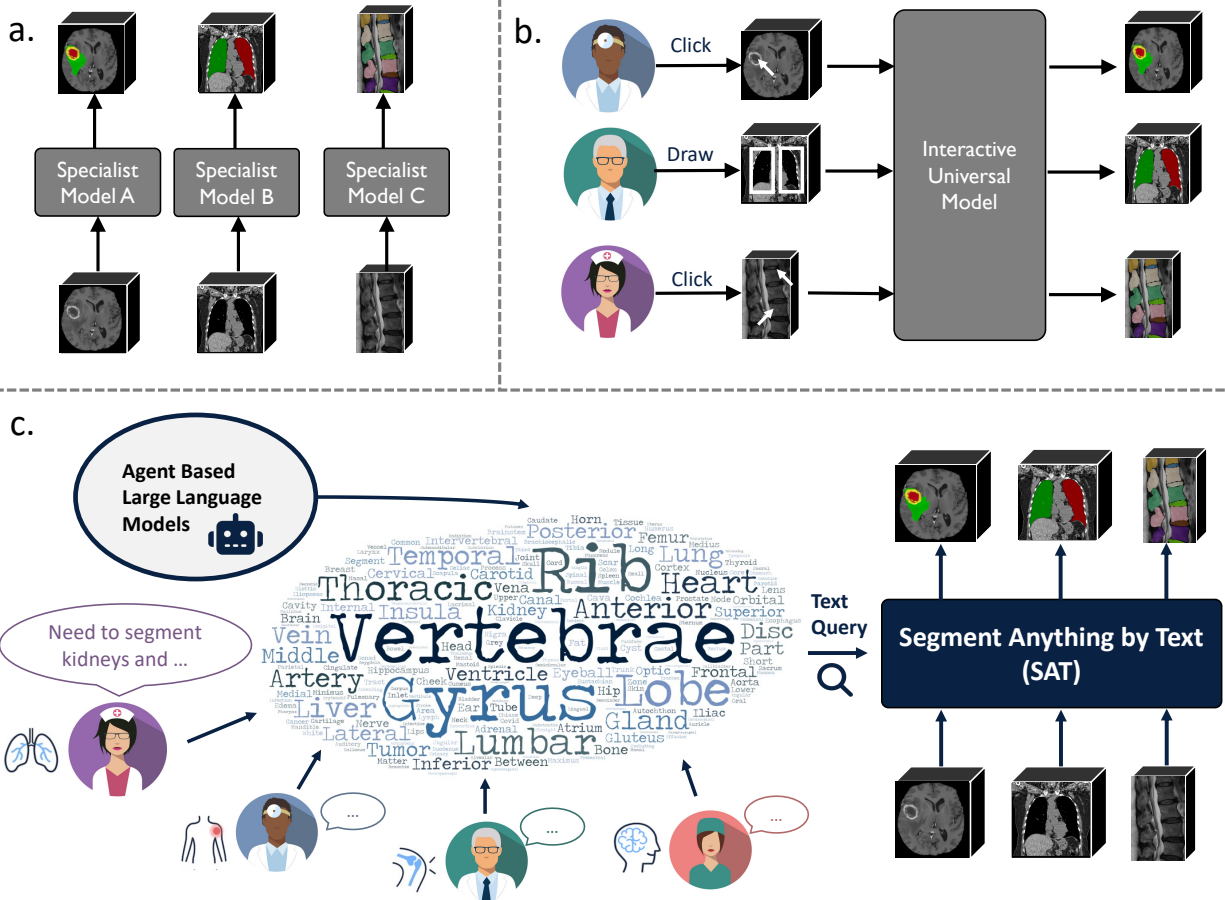


Figure 1 | In contrast to conventional specialist models (a) that develop specialized solution for each task, or recently proposed interactive universal segmentation models (b) relying on real-time human interventions, Segment Anything with Text (SAT) directly takes 3D volumes as inputs, and use text as prompts to perform a wide array of medical image segmentation tasks across different modalities, anatomies, and body regions (c). It can be easily applied to clinics or seamlessly integrated with any agent-based large language model.

while transferring to medical scenarios, these models trained on natural images suffer from fundamental limitations: (i) models typically perform 2D slice segmentation, that are later fused into 3D volumes through post-processing. This approach overlooks the crucial contextual information in 3D radiological imaging; (ii) models often require point or box inputs as prompts, thus is an interactive segmentation model, requiring considerable manual efforts for use in practice; (iii) models suffer from significant domain gaps, from image statistics to domain-specific medical knowledge.

In this paper, we present the **first knowledge-enhanced** universal model for 3D medical volume segmentation, **with medical terminology as text prompt**, termed as SAT. In practice, our model can effectively take 3D volume as visual inputs along with text prompts, to seamlessly tackle various medical image segmentation tasks, across modalities, anatomies, and body regions. As illustrated in Fig. 1, our proposed method distinguishes from previous medical segmentation paradigms, that can be seamlessly applied to clinics or integrated with any large language model. Specifically, we make the following contributions:

On dataset construction, we construct a knowledge tree on anatomy concepts and definitions throughout the human body. On the visual side, we curate over 22K 3D medical image scans with 302K anatomical segmentation annotations, covering 497 categories from 72 publicly available medical segmentation datasets, termed as SAT-DS. To the best of our knowledge, SAT-DS denotes the largest and most comprehensive collection of public 3D medical segmentation datasets. To achieve such goal, we have invested significant

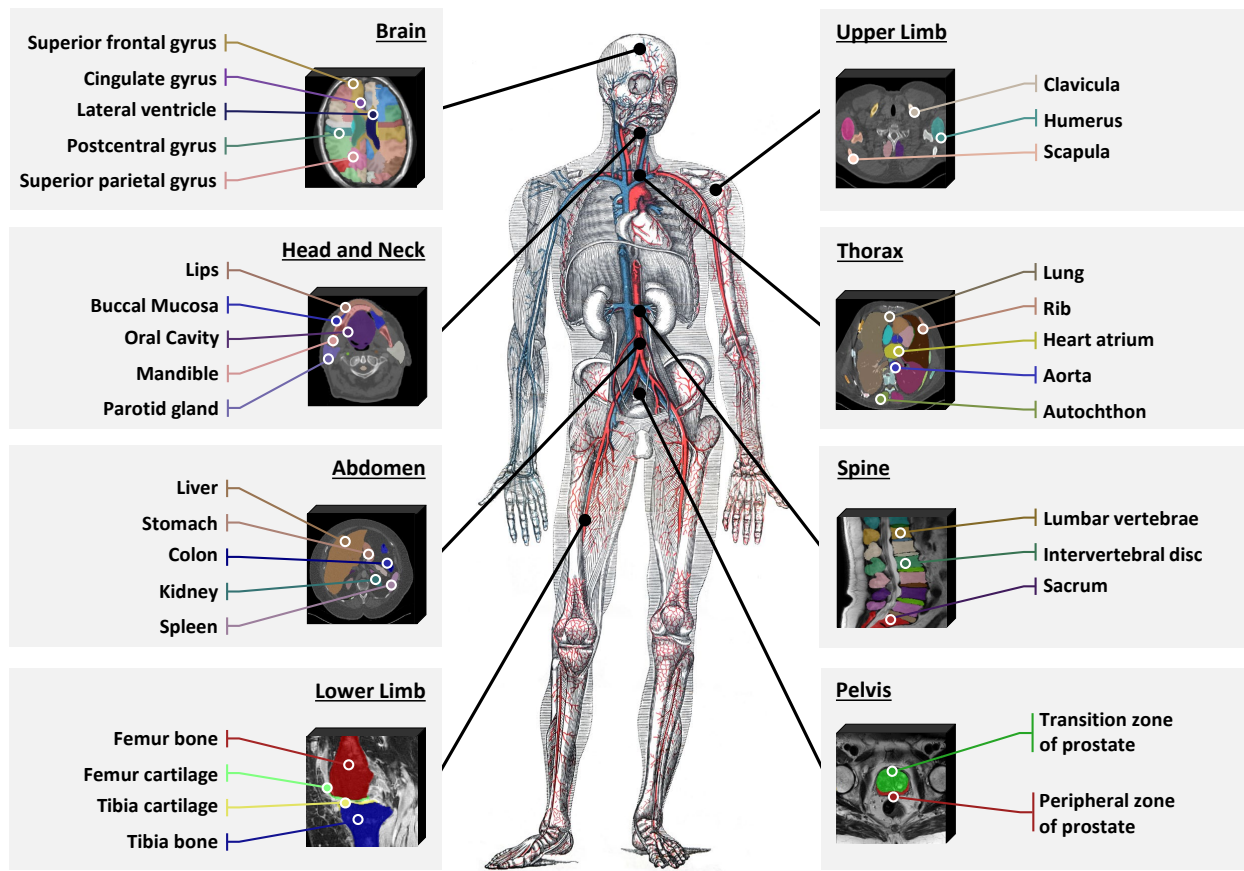


Figure 2 | Overview of our dataset for training universal segmentation model, from a wide range of segmentation tasks across various modalities and anatomical regions of the human body, including the brain, head and neck, thorax, spine, abdomen, upper limb, lower limb, and pelvis.

efforts in standardizing datasets and unifying annotation labels, paving the way for universal segmentation task. For complete list of datasets and download links, we refer the reader to Table 32 and Table 1.

On architecture design and training strategy, we build a universal medical segmentation model, that enables flexible segmentation across a spectrum of medical imaging modalities and anatomies, with text as prompts. Specifically, we adopt knowledge-enhanced representation learning, leveraging textual anatomical knowledge and atlas segmentation of specific anatomical structure to train the visual-language encoders. Through this training process, the visual features of these anatomical structures are aligned with their corresponding text descriptions in the latent space, which is validated to boost the segmentation performance, especially in a long-tail distribution. Later, the text embeddings of anatomy/abnormality are treated as queries in a Transformer-based architecture, iteratively attending the visual features to update queries for precise segmentation of the queried target. To meet the requirements from different computational resources, we train two models of varying sizes, namely, **SAT-Nano** and **SAT-Pro**, and validate the effectiveness of scaling model sizes.

On experiment evaluation, we devise comprehensive metrics for universal medical segmentation across various aspects, including region-wise average, organ-wise average, and dataset-wise average. Through extensive internal and external experiments, we demonstrate that:

- Building on the unprecedented dataset collection, SAT is able to handle a wide range of downstream segmentation tasks with medical terminologies as text prompts, simplifying the training and deployment procedure for conventional specialist models. On internal evaluation, **SAT-Pro** shows superior or comparable performance to 72 specialist models trained individually on each dataset (nnU-Nets, U-Mamba or SwinUNETR), despite being significantly lighter in model size (only 447M parameters); While

on external evaluation, it also demonstrates better generalization ability over all the specialist models.

- As a foundational segmentation model pre-trained on the large-scale and comprehensive data, **SAT-Pro** could be further optimized and adapted to specific tasks, balancing the clinical needs between universal solution and specialist models. Through extensive validation on 72 datasets, it shows superior performance over all the counterpart specialist models.
- Driven by text prompts, SAT outlines a novel universal segmentation paradigm as opposed to previous efforts in building interactive models, which relies on spatial prompts. This could save tremendous manual efforts from prompting in clinical applications. On performance, we demonstrate it can outperform the state-of-the-art interactive universal segmentation model MedSAM, while being robust to targets with ambiguous spatial relationships.
- Compared to the concurrent work BiomedParse [107], which also uses text prompt for biomedical image segmentation, SAT not only demonstrates superior segmentation performance, but also showcases a significantly broader capability on radiology images.
- The text-prompted feature and universality of makes SAT a powerful out-of-box agents for language model. We show SAT can be seamlessly integrated with any large language models such as GPT-4 [1], automatically providing grounding ability in diverse clinical scenarios. This potentially extends the application diagram of medical segmentation models, and advance generalist medical artificial intelligence.

2 Results

The objective of our proposed model, termed **Segment Anything with Text (SAT)**, is to develop a universal segmentation framework for 3D medical images, to handle various segmentation tasks with text prompts. To this end, we have developed a large-scale and comprehensive data collection, termed **SAT-DS**, covering a broad spectrum of medical image segmentation tasks. It includes 497 anatomical targets across 8 regions and various lesions of the human body, assembled from 72 distinct datasets. To balance the computational cost and performance, we train and evaluate two variants **SAT-Pro** and **SAT-Nano**.

In this section, we will detail the experiment results, where **SAT** is comprehensively evaluated against three categories of methods: (i) **specialist models**, that feature optimized configurations and are trained individually for each dataset, as a conventionally mainstream practice for medical image segmentation. We choose nnU-Nets [26], SwinUNETR [18] and U-Mamba [56] for comparison, as they are widely adopted and representatives for CNN-based, Transformer-based and Mamba-based architecture respectively; (ii) **interactive segmentation models**, that have recently investigated, to provide semi-automatic segmentation with spatial prompts. We choose MedSAM [55] as a typical and state-of-the-art baseline; (iii) **text-prompted segmentation model**, which is a paradigm shift from the previous two, capable of performing automatic segmentation across a wide range of tasks with text prompts. BiomedParse [107], is a concurrent work to ours, and compared in this study.

The evaluation are conducted on both **internal** and **external** datasets. Specifically, we split each dataset in SAT-DS into train and test splits in 8:2 ratio, a combination of these test splits are used for internal evaluation, *i.e.*, in-domain data. When comparing to off-the-shelf models, we tailor the scope of datasets to accommodate their varying capabilities, to avoid overlapping the train and test dataset. The external evaluation is conducted on two very recently published datasets, namely, AbdomenAtlas 1.1 [74] and LiQA [50], as they are excluded from SAT-DS and not used in training any of these methods. This simulates the scenario where the models are tested on multi-center images. **Note that**, this do not involve new classes, as the segmentation targets in human body are relatively limited and fixed.

We present evaluation results from various aspects, including **region-wise**, **class-wise**, and **dataset-wise**, to give a deep understanding of the models’ performance on large-scale segmentation. Note that, class-wise and region-wise evaluations are computed by averaging the results from different datasets. For instance, the performance metrics for the ‘brainstem’ in CT images represent the macro average from models trained on datasets, like ‘HAN Seg’, ‘PDDCA’, and ‘SegRap2023 Task 1’, that all include annotations for this anatomical class. Detailed experiment settings can be found in Sec. 4.4.

The following sections start with the experiments on internal datasets in Sec. 2.1, 2.2 and 2.3; Then, we will present the results of different methods on the external datasets in Sec. 2.4; Finally, we demonstrate ablation studies on the key components of SAT in Sec. 2.5, and its potential application scenarios in Sec. 2.6.

2.1 Comparison with Specialist Models on Automatic Segmentation

In this experiment setting, we compare with specialist models (nnU-Nets, U-Mamba, SwinUNETR) on all the 72 datasets in **SAT-DS** as internal evaluation. All specialist models are trained with optimized configuration on each dataset with official codes. While both **SAT-Pro** and **SAT-Nano** are trained and evaluated on all datasets as one model. **Note that**, unless otherwise stated, SAT-Pro and SAT-Nano are trained on all 72 datasets of SAT-DS throughout the following text.

Fig. 3 (a) and Supplementary Table 3 shows the **region-wise results** on 8 regions of human body, including ‘Brain’, ‘Head and Neck’, ‘Thorax’, ‘Abdomen’, ‘Pelvis’, ‘Spine’, ‘Upper Limb’, and ‘Lower Limb’, as well as ‘Lesion’, in terms of DSC and NSD, respectively. Classes existing in multiple regions are specifically grouped as ‘Whole Body’. Supplementary Table 3 provides detailed numbers and the average results on all 497 classes.

Despite having been proposed for a few years, nnU-Nets remains the best-performing specialist model overall. As an universal model, **SAT-Pro** consistently outperforms the most competitive baseline nnU-Nets in four regions: Head and Neck, Thorax, Upper Limb and Lower Limb. On average performance of all 497 categories, SAT-Pro show comparable performance to nnU-Nets and U-Mamba, and surpass SwinUNETR significantly, while SAT-Nano outperforms SwinUNETR.

Fig. 3 (b) and (c) provides another view on the above results, where it can be seen that SAT-Pro shows comparable or segmentation performance to the 72 nnU-Nets, while being of significantly smaller size and more capable, for example, SAT-Pro is approximately 1/5 of the assemble of nnU-Nets, and enable to handle 497 classes, in contrast to 12 classes of the specialist models.

We further finetune **SAT-Pro** on each of the 72 datasets, and report the **region-wise results** in Supplementary Table 3, denoted as **SAT-Ft**. Without bells and whistles, it shows significant improvement on all the regions and lesions, outperforming the most competitive specialist model, for example, nnU-Nets, on both DSC and NSD. This indicate that SAT can be potentially used as a strong pre-trained model, and adapted towards specific downstream dataset easily.

We present more detailed class-wise results in Supplementary Table 9, 10, 11 and 12; dataset-wise results in Supplementary Table 5, 6, 7, 8.

2.2 Comparison with Interactive Universal Segmentation Model

In this section, we compare with MedSAM, which is an out-of-the-box universal segmentation methods trained on large-scale data. Specifically, due to the inconsistent training data, we carefully choose 32 out of 72 datasets for internal evaluation, which are also involved in training MedSAM. **Note that**, even though these datasets are included in training MedSAM, we are unable to align the train-test splits, which means the test set we used might be leaked in training MedSAM. We report **three results**: (i) simulate box prompts based on the ground truth segmentation, with minimum rectangle covering the ground truth (denoted as Tight), *i.e.*, the most accurate prompts; (ii) randomly shift each box corner up to 8% of the image resolution (denoted as Loose), *i.e.*, allow errors to some extent; (iii) directly use the tight box prompts as prediction (denoted as Oracle Box), *i.e.*, the input baseline of MedSAM.

Fig. 4 (a) and Supplementary Table 4 show the **region-wise results** of all methods. Notably, **SAT-Pro** consistently outperforms MedSAM on all human body regions, even if MedSAM is prompted with the most accurate box (Tight). On lesion segmentation, **SAT-Pro** underperforms MedSAM (Tight), due to the small size of lesion, and the box prompts to MedSAM have already provided very strong prior, where oracle box even shows better performance than MedSAM output on DSC score. While perturbing the box prompts, MedSAM (Loose) shows significant performance drop across all regions and metrics.

On **class-wise results**, in Fig. 4 (b), we present the performance difference between SAT-Pro and MedSAM on each category, with respect to the spatial irregularity of regions. Inspired by BiomedParse [107], we define spatial irregularity with two factors: the ratio of ground-truth to the tightest convex, denoted as ‘Convex

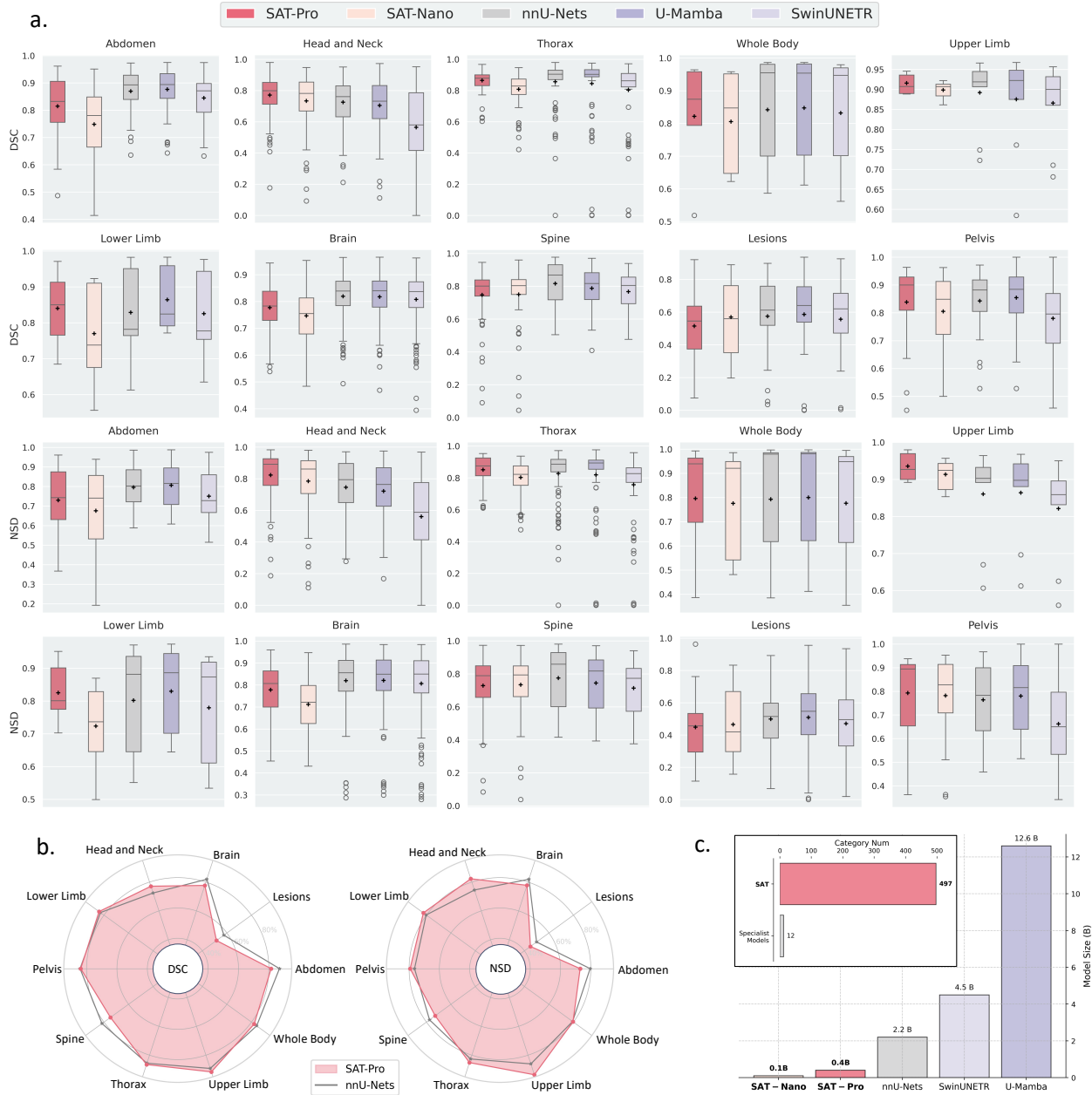


Figure 3 | Internal evaluation between SAT-Pro, SAT-Nano, and three specialist models on 72 datasets from SAT-DS. Results are merged by different human body regions and lesions. **a**, Box plots on DSC and NSD results. The center line within each box indicates the median value; the bottom and top bound indicate the 25th and 75th percentiles respectively. The mean value is marked with a plus sign. The whiskers extend to 1.5 times the interquartile range. Outlier classes are plotted as individual dots. **b**, Comparison between SAT-Pro and the most competitive specialist models nnU-Nets on performance. **c**, Comparison between SAT and specialist models on model size and capability range. SAT has much smaller model size compared to the assemble of specialist models, while capable of segmenting 497 targets in one model. By comparison, each specialist model can only segment 12 targets on average.

Ratio’; the DSC score between oracle box prompt and ground-truth, denoted as ‘Oracle Box DSC’. We observe that SAT-Pro achieves greater improvement on targets with more irregular shapes, while MedSAM outperforms on some relatively regular-shaped targets.

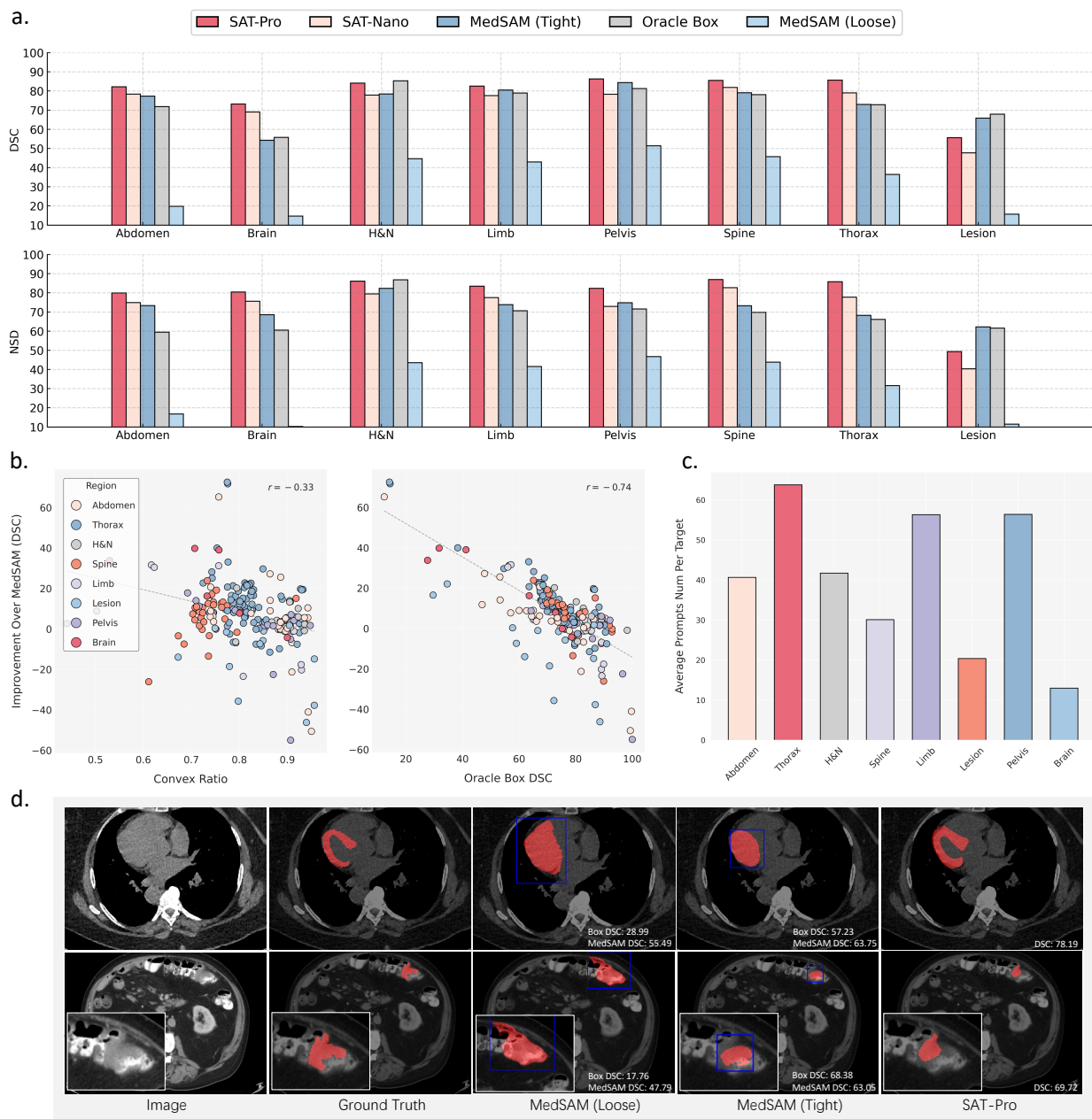


Figure 4 | Internal evaluation between SAT-Pro, SAT-Nano, and MedSAMs on 32 datasets from SAT-DS Results are merged by different human body regions and lesions. **a**, Histograms on DSC and NSD results. **b**, Scatter plots comparing the performance improvement of SAT-Pro over MedSAM on different segmentation targets (DSC score), with two irregularity metrics: convex ratio and oracle box DSC. Each point represents an anatomical structure or lesion, with a fitted line illustrating the trend. **c**, Average prompt numbers required by MedSAM to segment a target in 3D radiology scan, averaged over different human body regions. **d**, Quantitative results of MedSAMs and SAT-Pro on myocardium (upper row) and colon cancer (lower row). The ground truth and segmentation masks are painted in red, while box prompts of MedSAM are plotted in blue. The DSC score is calculated in slice-wise manner.

We further present the **qualitative results** from two representative examples in Fig. 4 (d). The upper row shows segmentation of myocardium with a relatively irregular shape. MedSAM incorrectly includes the left heart ventricle surrounded by the myocardium. By comparison, SAT-Pro generate accurate prediction, simply prompted with the word ‘myocardium’. The lower row demonstrates colon cancer segmentation on a CT

image. The tight box prompt to MedSAM can be viewed as an acceptable segmentation, despite its limitation as a rectangle. While the prediction of MedSAM is worse. In addition, in both cases, we observe a noticeable performance drop when the box prompt contains certain deviations, *i.e.*, MedSAM (Loose).

In Fig. 4 (c), we show the average prompts required by MedSAM to segment a target in 3D image scan. As it only allows slice-wise segmentation, and the morphology of segmentation targets varies across different body regions, the number ranges from 10+ to 60+. By contrast, as a fully automatic segmentation model for 3D radiology images, SAT requires only a single text prompt to segment the entire 3D image scan. And simplicity advantage can be more pronounced for multiple targets segmentation.

We present more detailed **class-wise results** in Supplementary Table 13, **dataset-wise results** in supplementary material Table 5, 6, 7 and 8.

2.3 Compare with Text-Prompted Universal Segmentation Model

In this section, we compare with BiomedParse [107], a concurrent work that proposed universal segmentation tool for general 2D bio-medical images and prompted by text. We choose 11 datasets for internal evaluation. We report two results for BiomedParse: (i) based on the ground truth, we only prompt target present in the current slice, which follows its official evaluation setting. Similar to MedSAM, this approach avoids potential false positives on unannotated slices, and thus represents the performance under ideal conditions. We denote the results as BiomedParse (Oracle); (ii) consistent with SAT, we prompt all the targets available in the dataset and filter out the potential false positive predictions by p-values, suggested by official implementation.

Fig. 5 (a) and Supplementary Table 14 presents the **class-wise** performance of SAT and BiomedParse. Across all categories, BiomedParse (Oracle) consistently achieves higher DSC and NSD scores compared to BiomedParse. This highlights that BiomedParse is prone to generating false positive predictions when prompted with non-existing targets, likely due to BiomedParse being a 2D slice segmentation model, which overlooks critical information from adjacent slices. SAT-Pro consistently outperforms BiomedParse in all categories except for myocardium. Even compared to BiomedParse (Oracle), SAT-Pro demonstrates superior performance on 23 out of 30 categories, and notably excels in overall performance.

Furthermore, as illustrated in Fig. 5 (b), BiomedParse is primarily designed as a segmentation tool for 2D biomedical images. In contrast, SAT, developed as a universal segmentation model specifically for 3D radiology images, demonstrates significantly broader applicability and superior performance on 3D radiology images.

2.4 Evaluation on External Datasets.

Here, we aim to evaluate the generalization performance of segmentation models on images from different medical centers. As universal segmentation models, SAT, MedSAM and BiomedParse are directly evaluated on two unseen datasets; While for specialist models, considering their customized configurations on each dataset, we systematically evaluate 21 out of 72 specialist models on target datasets for shared categories. For example, to evaluate the generalization performance on ‘lung’ in AbdomenAtlas, we use specialist models trained on CT-ORG and LUNA16, as they all involve this class, and then average the results. The details of the overlapped labels spaces are shown in Supplementary Fig. 15. To maintain the performance for specialist models, the pre-processing of target datasets is kept the same as source dataset in evaluation.

We report DSC and NSD results in Fig. 6 and Supplementary Table 15, with the following observations: (i) on specialist models, U-Mamba achieves more competitive results over nnU-Nets on both DSC and NSD scores. While SwinUNETR remains the worst; (ii) on universal model for 2D images, MedSAM (Tight) consistently outperform BiomedParse (Oracle) on all categories, implying that the accurate box prompts provides strong prior when extending to out-of-domain images; (iii) SAT-Pro achieves the best performance on average over all categories, exceeding the second best candidate MedSAM by 2.9 on DSC and 5.52 on NSD. Meanwhile, SAT-Pro consistently outperforms the specialist models on all categories in terms of NSD score, and 17 out of 19 categories in terms of DSC score.

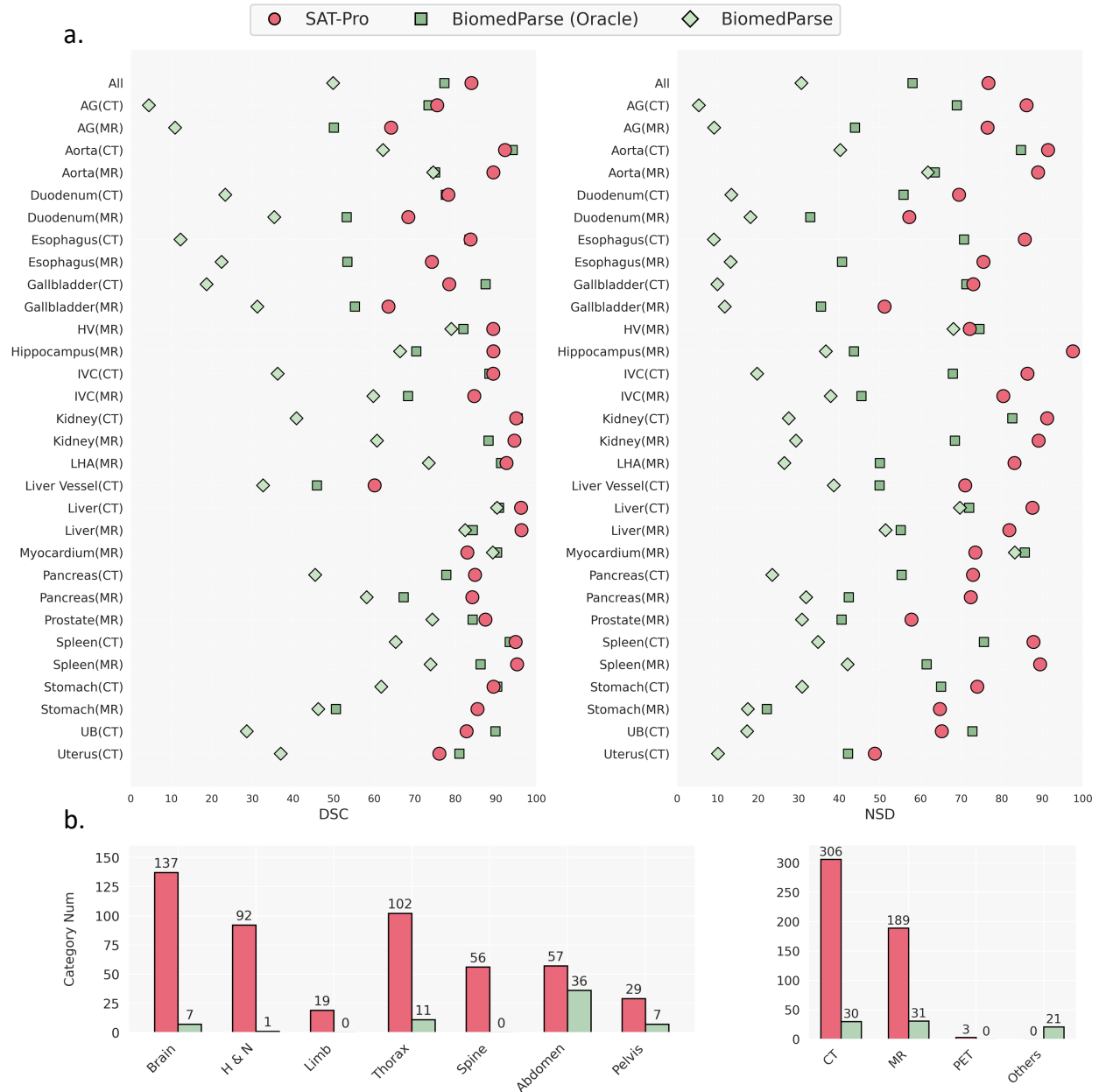


Figure 5 | Internal evaluation between SAT-Pro and BiomedParses on 11 datasets from SAT-DS. (a) DSC and NSD scores. Results are merged and presented in class-wise manner. (b) The number of anatomical structures and lesions SAT and BiomedParse can segment on different human body regions in radiology images, and on different imaging modalities. ‘Others’ denotes non-radiology modalities.

2.5 Ablation Study

As will be illustrated in Sec. 4.2, to build an universal segmentation model driven by text prompts, we devise the visual encoder and decoder to process diverse medical images and perform segmentation; Meanwhile, domain knowledge is injected into the text encoder to provide precise prompts for the target of interest, *i.e.*, the encoding of terminology. In this section, we conduct experiments and discuss the effect of different visual backbones and domain knowledge. To save computational cost, all experiments in this section have been conducted on **SAT-DS-Nano** dataset.



Figure 6 | External experiments between SAT, specialist models, MedSAM and BiomedParse on AbdomenAtlas and LiQA. Both DSC and NSD results are presented for each class in each dataset. We enlarge the size of SAT-Pro in each sub-figure for distinction, and annotated the ranking of SAT on each class.

2.5.1 Effect of Visual Backbone

We investigate three different backbones for universal segmentation, namely, CNN-based U-Net, SwinUNETR [19] and U-Mamba [17]. We configure three **SAT-Nano** variants with SwinUNETR (107M), U-Mamba (114M) and U-Net (110M) in comparable size: For SwinUNETR, we use the same hyper-parameters as in official implementation [18]; For U-Mamba, we refer to the official implementation [56], reserving configuration of the U-Net, and only add mamba layers at the end of last 3 blocks of the U-Net encoder.

To avoid repeating multimodal knowledge injection on each visual backbones, we use MedCPT [30] for all these variants as text encoder, without loss of generality. MedCPT is a text encoder trained on 255 million in-house user click logs from PubMed [80], and shows state-of-the-art performance on various biomedical language tasks, for example, medical language retrieval. Thus, we denote these variants as U-NET-CPT, SwinUNETR-CPT and U-Mamba-CPT. We demonstrate the region-wise evaluation results in Fig. 7. U-Net-CPT outperforms U-Mamba-CPT slightly on both DSC (0.35) and NSD (0.22) scores averaged over all classes. However, both U-Net-CPT and U-Mamba-CPT exceed SwinUNETR-CPT by a significant margin. These observations confirm our choice of U-Net as the visual backbone of **SAT**. For more detailed comparison on each dataset and class, we refer the reader to Supplementary Table 22, 23, 24 and 25.

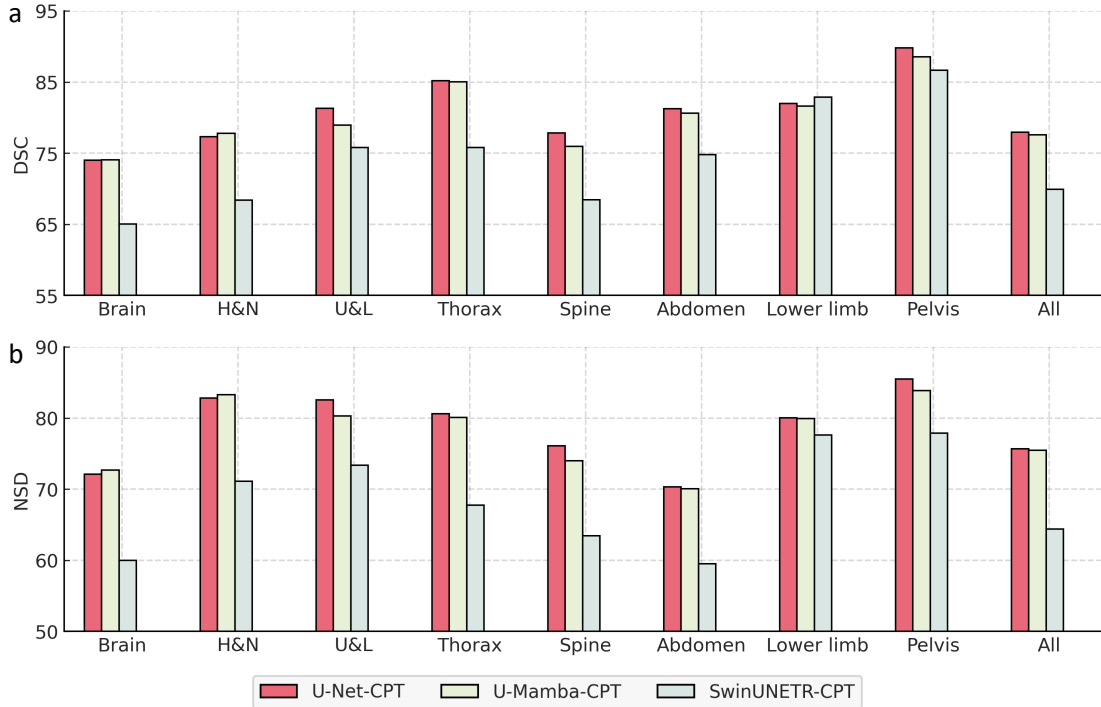


Figure 7 | Evaluations on SAT-DS-Nano variants with different visual backbones. ‘All’ denote the average scores over all the classes ($n=429$), including lesion classes. **a**, DSC comparison; **b**, NSD comparison. U-Net-CPT and U-Mamba-CPT perform very close, while both surpass SwinUNETR-CPT considerably.

2.5.2 Effect of Text Encoder

In this section, we investigate the impact of text encoder for the text-prompted segmentation model. Specifically, we train four **SAT-Nano** variants with different text encoders: (i) BERT-Base, a prevalent text encoder in natural language processing, but not specifically finetuned on medical corpus; (ii) text encoder of CLIP, a state-of-the-art model pretrained on 400M image-text pairs and widely used in vision-language tasks; (iii) the state-of-the-art text encoder for medical retrieval tasks, *e.g.*, MedCPT; (iv) the text encoder pre-trained on our multimodal medical knowledge graph, as illustrated in Sec. 4.2.2; For all the variants, we use U-Net as visual backbone, and denote them as **U-Net-BB**, **U-Net-CLIP**, **U-Net-CPT** and **U-Net-Ours**.

Region-wise Evaluation on Segmentation. As shown in Fig. 8 and Supplementary Table 21, the performance of U-Net-BB, U-Net-CLIP and U-Net-CPT are close. Overall, U-Net-BB performs worst, while U-Net-CPT slightly exceeds on DSC (+0.1) and U-Net-CLIP slightly exceeds on NSD (+0.29) scores averaged over all class. By contrast, U-Net-Ours surpasses all other variants consistently on all regions, with notable margins on both DSC (+1.54) and NSD (+2.36) scores on average over all classes. This demonstrates the effectiveness of our proposed multimodal knowledge injection. For more detailed comparison on each dataset and class, we refer the reader to Supplementary Table 18, 17, 19 and 20.

Medical Concept-to-Definition Retrieval. In addition to segmentation performance, we evaluate the text encoders on ‘concept-to-definition’ retrieval on human anatomy knowledge, in total, we collect 6,502 anatomy concepts and definition pairs. We find that the Recall1 (R1) for BERT-Base is only 0.08%, suggesting it can hardly understand these anatomy concepts or possess almost no domain knowledge; The R1 is 4.13% for CLIP, and 11.19% for MedCPT. Though this is a significant improvement over BERT-Base, they still struggle to distinguish these concepts; By contrast, our proposed text encoder get 99.18% R1, indicating the knowledge is successfully injected into the text embedding for each anatomy concept.

Knowledge Injection Benefits Segmentation of Long-tail Classes. The 429 classes in **SAT-DS-Nano** typically follow a long-tail distribution, as illustrated in Fig. 9 (a) and (b). The 10 ‘head’ classes account for

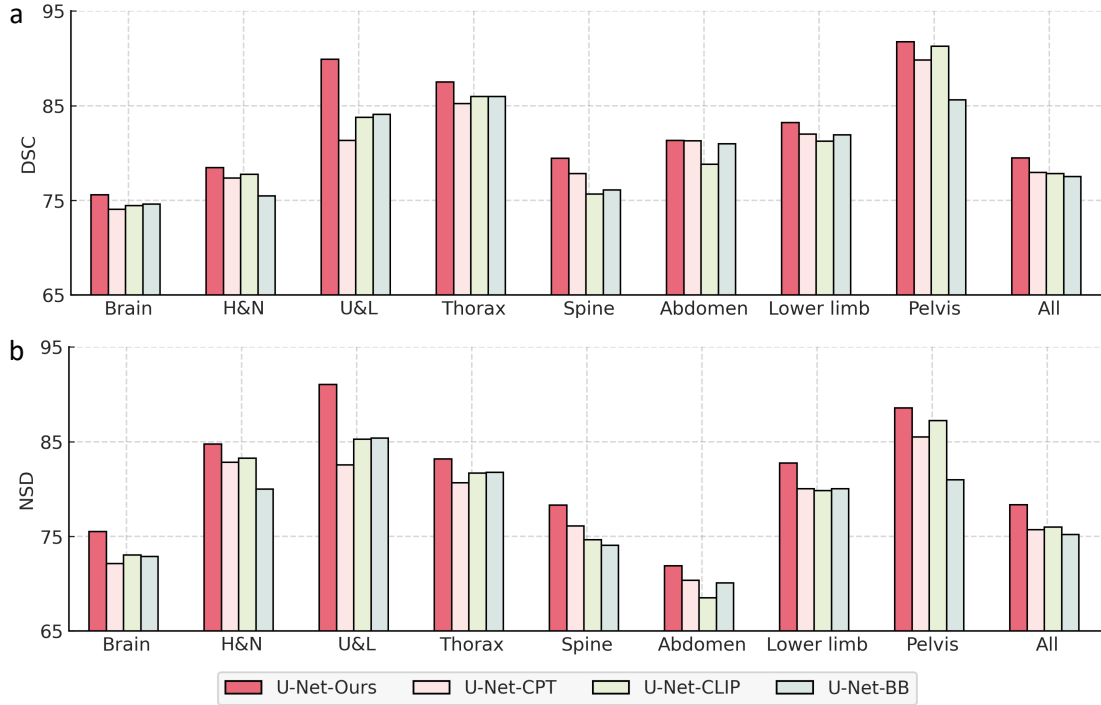


Figure 8 | Evaluations on SAT-DS-Nano variants with different text encoders. ‘All’ denote the average scores over all the classes($n=429$), including lesion classes. **a**, DSC comparison; **b**, NSD comparison.

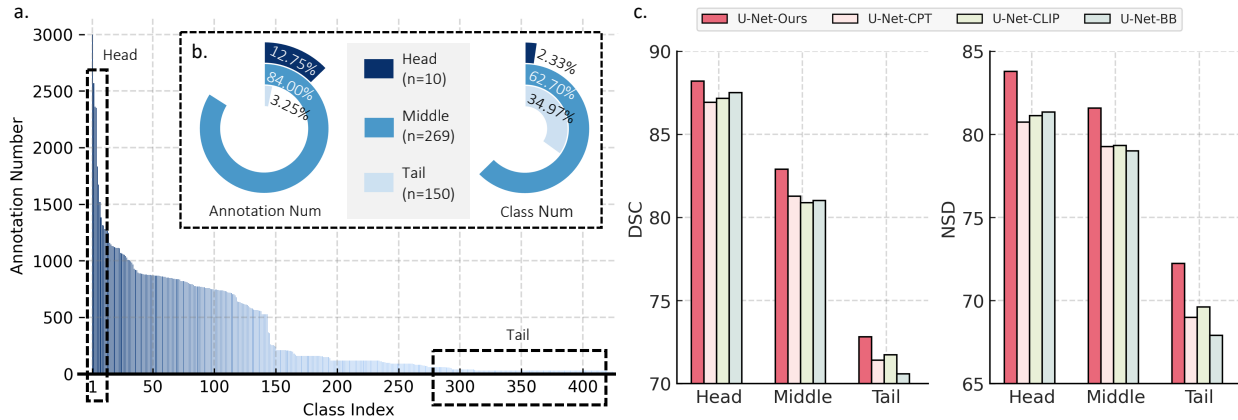


Figure 9 | The impact of domain knowledge on a long-tail distribution. **a**, The annotation number of all the 429 classes in SAT-DS-Nano, sorted from highest to lowest. **b**, The proportion of ‘head’, ‘middle’ and ‘tail’ in class number and annotation number. The DSC and NSD comparison on ‘head’, ‘middle’ and ‘tail’ classes.

12.75% of the annotations in SAT-DS-Nano; In contrast, the 150 classes with minimum annotations accounts for only 3.25%, even though they comprise 34.97% of 429 classes. We compare U-Net-Ours, U-Net-CPT, U-Net-CLIP and U-Net-BB on the ‘head’ classes, ‘tail’ classes and the rest ones (denoted as ‘middle’ classes). In Fig. 9 (c), the performance of the model variants drop from head to tail classes, showing that the long-tailed distribution poses a significant challenge for universal segmentation. While using our proposed knowledge-enhanced text-encoder, U-Net-Ours achieves the best performance on all three scenarios. On ‘head’ classes, it outperforms the second best variant by 0.71 on DSC and 2.44 on NSD. On ‘tail’ classes, the improvement is even more pronounced.

To further validate the necessity of both textual and visual knowledge introduced in Sec. 4.1.1, we conduct an ablation study in Supplementary Table 21. The results show that pre-training with only textual knowledge already outperforms all other baselines, *i.e.*, MedCPT, BERT-Base and CLIP, and incorporating visual knowledge further enhances performance.

2.6 Qualitative Results – SAT as an Interface Between Language and Segmentation

Thanks to the text-driven features of SAT, it can be seamlessly applied as an interface between natural language and segmentation, *i.e.*, acting as a high-performance and efficient agent for language models. Here, we demonstrate three potential applications in Fig. 10: (i) we demonstrate a scenario where GPT-4 [1] analyze and extract the anatomical targets of interests from real clinical report, and prompt SAT to segment them on the clinical image. As can be seen on the upper row, the targets in reports can be well detected by language model (GPT-4) and commendably segmented by SAT-Pro, which provides visual cues for clinic report and enhance its interpretability; (ii) we show that SAT can help LLM handle segmentation request in a free-form conversations with any users. The LLM can easily recognize these requests and leverage SAT to deliver precise segmentation results, which greatly extend the conversational interface. (iii) we explore a more complicated situations, where SAT can ground the lesions based on the comprehensive analysis of the radiology images as well as contextual EHR data such as patient complaint, establishing a whole automated pipeline from diagnosis to segmentation.

3 Discussion

Developing specialist models on individual tasks has been the dominant solution for medical image segmentation for years [26, 15, 44, 101, 110, 83, 106, 20, 11, 18, 98, 105, 12, 109], in this paper, we aim to build effective and flexible universal medical segmentation model, by training on unprecedented dataset collection, and driven by knowledge enhanced text prompt. In this section, we discuss the significance, potential and limitations of the proposed SAT, based on our experiment results in Sec. 2.

A Universal Model is Worth 72 Specialist Models. Despite the diverse image and segmentation targets from different clinical scenarios, SAT can flexibly handle them with one model, which denotes an important step towards universal segmentation model in medical scenario. Through comprehensive internal evaluation, SAT-Pro has demonstrated superior or comparable results to the assemble of 72 specialist models, *i.e.*, nnU-Net, U-Mamba or SwinUNETR. While evaluating external multi-center datasets, SAT-Pro exhibits superior generalization ability than all specialist models, highlighting its superior cross-center generalisation. With dataset-specific fine-tuning, SAT-Ft can further improve the performance, thus, it naturally acts a foundational segmentation model, pre-trained on large-scale and diverse data.

Text-prompted Universal Segmentation Can Be User Friendly. As an automatic method prompted by text, SAT outlines an alternative approach from recent works, for example, interactive universal segmentation [55, 91]. Through both qualitative and quantitative comparisons, SAT demonstrates superior performance, particularly on targets of irregular shapes. Unlike interactive methods relying on spatial prompts, that may suffer from inaccurate prompts, and lead to performance fluctuations, SAT can effectively automate segmentation on 3D images with text prompts, significantly reducing the cost from users inference time. In addition, comparing to our concurrent work on text-prompted 2D universal segmentation model, namely BiomedParse [107], SAT demonstrates significantly broader applicability in 3D radiology images, and consistently shows superior performance in both in-domain and out-of-domain scenarios.

Scaling Models Lead to Better Performance. Increasing model capacity has been demonstrated to effectively enhance model’s performance in large language models [95, 88], yet such scaling law remains to be verified in segmentation tasks. In this work, we build SAT-Nano (110M) and SAT-Pro (447M), in both region-wise and class-wise evaluations, SAT-Pro shows clear performance boost over SAT-Nano, outperforming the latter on most region and classes. This implies that scaling law is also applicable to universal medical segmentation, indicating a promising way to continuously improve the performance.

Domain Knowledge Are Beneficial for Universal Segmentation. We construct the first multimodal knowledge graph on human anatomy and demonstrate that knowledge injection can significantly improve

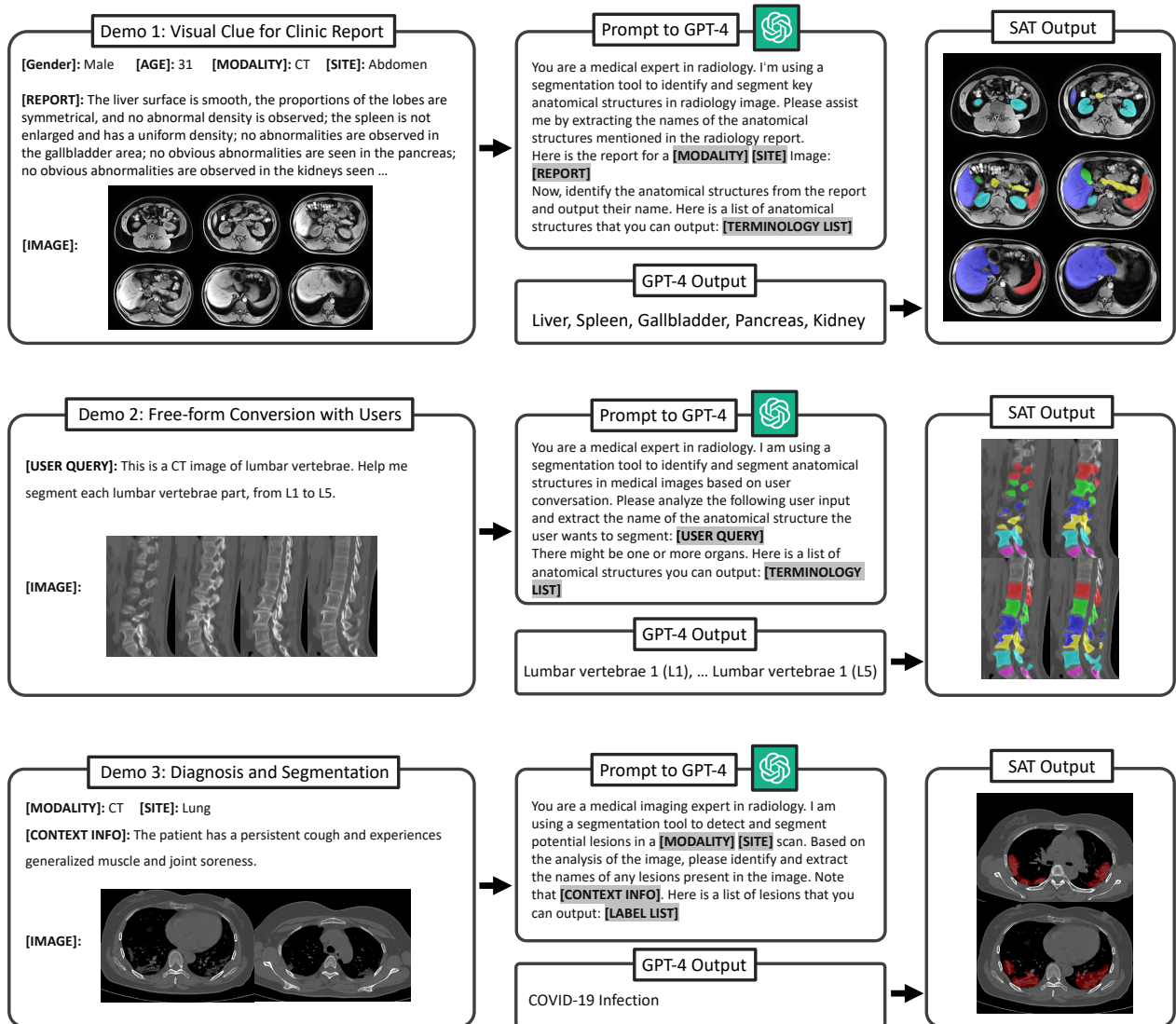


Figure 10 | SAT as agent for large language models. Combining SAT-Pro and GPT4, we demonstrate three potential applications: providing visual clues for clinic report, handling segmentation request in free-form conversation, and an automated pipeline from diagnosis to segmentation. For each case, We extract representative slices from the image volume for demonstration. In real application, the prompt templates and the terminology lists can be modified upon users' requirement.

segmentation performance, particularly for ‘tail’ classes. As the scope of universal segmentation expands to include an increasing number of targets, the long-tail problem will become more pronounced, underscoring the critical importance of knowledge enhancement in addressing this challenge.

SAT Can Be Used As An Agent to Bridge Language and Segmentation. In Sec. 2.6, we show that SAT can be applied to segment targets based on the output from language model and support visual grounding across various clinical scenarios. This highlights the potential of SAT as a high-performance, efficient, and out-of-the-box tool agent, seamlessly collaborating with the ever evolving large language models. In addition, SAT has recently been applied to provide comprehensive grounding annotations for medical visual-language datasets in a scalable manner [104, 99].

Future Work. As one of the first exploratory work in this field, we have shown the potential to build one model for universal segmentation, and propose the following future work: (i) the performance of SAT-Pro still lags behind some specialist models, *e.g.*, nnU-Nets, in some region. Further scaling up the model can be a

promising direction; (ii) for practical deployment, we will explore approach for efficient inference, for example, our subsequent work [42]; (iii) to make the model more flexible, it would be interesting to combine various prompts, for example, texts, boxes, points, scribbles; (iv) SAT is built and used with medical terminology as text prompts, it would be interesting to incorporate powerful medical LLMs to understand user's free-form input, for example, the ones that have been investigated by our group [95, 73, 96].

4 Method

4.1 Dataset Construction

Toward building a universal segmentation model for medical imaging, with text as prompts, we collect two types of data in this work: medical domain knowledge to train the text encoder, and medical segmentation data, which includes both images and segmentation masks. In this section, we will describe them sequentially.

4.1.1 Domain Knowledge

To acquire textual knowledge, we mainly exploit two sources of domain knowledge: the Unified Medical Language System (UMLS)¹, a comprehensive medical knowledge graph consisting of concept definitions and their interrelations; search engines, which are prompted to organize knowledge into a graph of the same format, specifically refined for the human anatomy corpus. Regarding visual knowledge, we have compiled 72 medical segmentation datasets, creating an atlas that covers over 497 anatomical structures of the human body. All sources of knowledge are systematically categorized, encompassing anatomies and concepts from all regions of the human body. Two examples of these sources are illustrated in Fig. 11 (a) and (b).

UMLS. Unified Medical Language System (UMLS) [10] is a knowledge source of biomedical vocabulary developed by the US National Library of Medicine². It integrates a wide range of concepts from more than 60 families of biomedical vocabularies, each equipped with a Concept Unique Identifier (CUI) and definition. It also contains the relations among these concepts. Following [103], we extract 229,435 biomedical terminologies and definitions, as well as 1,048,575 relationship triplets, composing a knowledge graph on these terminologies.

Domain Knowledge from Search Engine. Although UMLS is widely acknowledged and adopted as a general medical knowledge corpus [97, 103, 41, 108], it lacks a fine-grained description of anatomy concepts critical for segmentation tasks. For example, for ‘liver’, the definition is ‘A large lobed glandular organ in the abdomen of vertebrates that is responsible for detoxification, metabolism, synthesis, and storage of various substances.’, which erases the morphological features and focuses on functionality. Meanwhile, more comprehensive knowledge on human anatomy may be scattered across various authoritative websites online, *e.g.*, Wikipedia³, ScienceDirect⁴, *etc.*. To harvest such knowledge, we select 6,502 anatomy concepts, and prompt a search engine⁵ to retrieve and summarize definitions for them. We use the following prompt template:

Definition of xxx. Include the location, shape, appearance, structure and spatial relations to other anatomy structures. No need to include functionality. End with ‘END’.

For illustration, the search engine referred to authority websites including Columbiasurgery⁶, Hopkins Medicine⁷ and summarized definition for ‘liver’ as: ‘A large organ found in the upper right quadrant of the abdomen, it stands as the largest gland within the human body, with a weight of about 1.5 kilograms. This structure exhibits a reddish-brown hue and is cone or wedge-shaped’. While constructing the knowledge graph, we also adopt GPT4 [1] to extract 38,344 relations between anatomical structures in the generated information-dense definitions with the following prompt:

This is the description of xxx. Please help me find its relations with other anatomical structures in radiological images. Summarize them with the template: Relation: xxx (relational preposition), Anatomical structure: xxx (name of another anatomical structure).

¹<https://www.nlm.nih.gov/research/umls>

²<https://www.nlm.nih.gov>

³<https://www.wikipedia.org>

⁴<https://www.sciencedirect.com/browse/journals-and-books?subject=medicine-and-dentistry>

⁵<https://you.com>

⁶<https://columbiasurgery.org/liver/liver-and-its-functions>

⁷<https://www.hopkinsmedicine.org/health/conditions-and-diseases/liver-anatomy-and-functions>

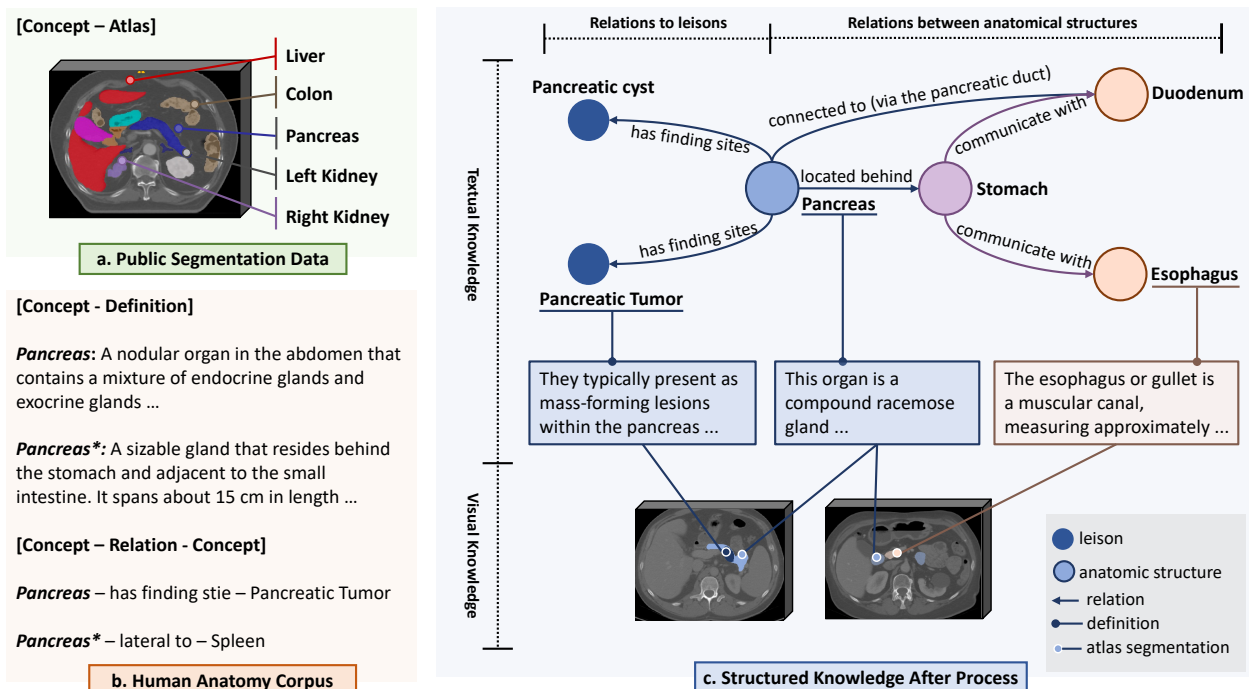


Figure 11 | The medical knowledge used in the visual-language pretraining. (a) Segmentation datasets provide an atlas for extensive anatomy concepts. In this example, atlas segmentation is marked with different colors. (b) Knowledge generated from UMLS and search engines encompasses a broad array of concept-definition pairs and extensive relationships. (c) By integrating all collected knowledge sources, a medical knowledge tree is constructed. All definitions are partially displayed for conciseness. Definition and relation denoted with * are derived from the search engine, otherwise from UMLS.

For example, “Relation: situated below, Anatomical structure: xxx”, “Relation: connected to (via xxx), Anatomical structure: xxx”

Visual Atlas. Segmentation datasets naturally provide visual features for anatomy concepts corresponding or complementary to the textual description, such as the texture, spatial location, shape and so on. Details on our collected segmentation datasets are described in Sec. 4.1.2. Here, we use them as a large-scale and diverse visual atlas library, and link the visual regions to corresponding concepts in textual knowledge graph, bridging the knowledge between visual and language modality.

In summary, by mixing these data, we construct a multimodal medical knowledge tree. As demonstrated in Fig. 11 (c), the concepts (including both anatomical structures and lesions) are linked via the relations and further extended with their definitions, containing their characteristics. Additionally, some are further mapped to the visual atlas, demonstrating their visual features that may hardly be described purely by text. For more examples on the curated knowledge dataset, we refer the reader to Supplementary Table 35, 36 and 34.

4.1.2 Segmentation Dataset

To train our segmentation model with the ability to handle segmentation tasks of different targets, across various modalities and anatomical regions, we collect and integrate 72 diverse publicly available medical segmentation datasets, totaling 22,186 scans including CT, MRI and PET, and 302,033 segmentation annotations spanning 8 different regions of the human body: Brain, Head and Neck, Upper Limb, Thorax, Abdomen, Plevis, and Lower Limb. The dataset is termed as **SAT-DS**. More details are present in Table 32 and Table 1. **Note that**, some public datasets are not mutually exclusive, *e.g.*, KiTS23 and KiTS21 [23], we thus only collect the latest version, to avoid redundancy and potential data leakage in train-test split.

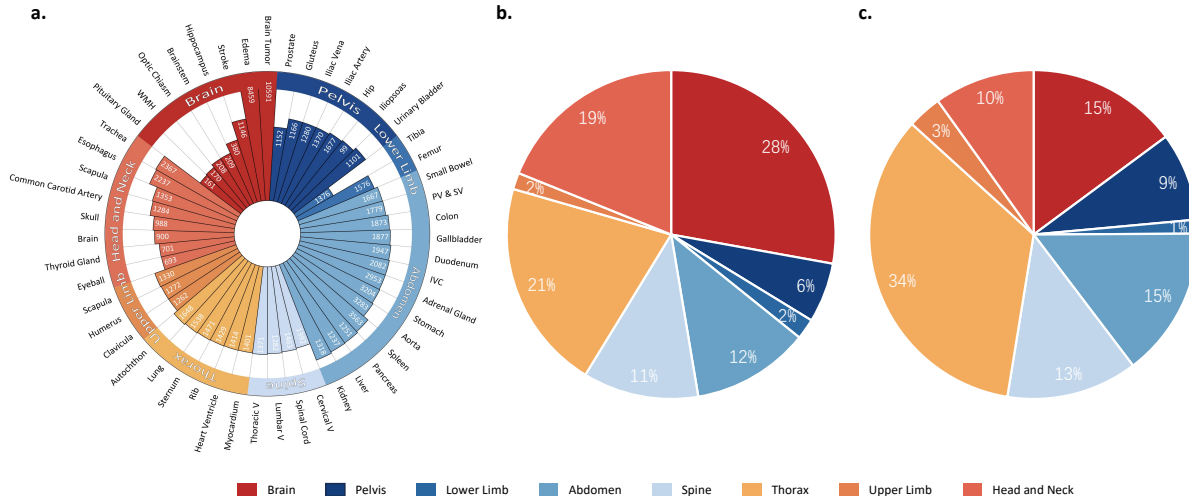


Figure 12 | Statistics of SAT-DS across different anatomical regions. (a) Annotation num of some representative classes in each anatomical region; (b) Number of classes in each anatomical region; (c) Number of annotations in each anatomical region. LC/HC: laryngeal/hypopharyngeal cancer, WHM: white matter hyperintensities, PV&SV: portal vein and splenic vein, IVC: inferior vena cava, Thoracic V: thoracic vertebrae, Cervical V: cervical vertebrae, Lumbar V: lumbar vertebrae.

Before mixing these datasets for training, two challenges remain: (i) the anatomical targets from each dataset must be integrated into a unified annotation system. The clinic demands beneath each dataset collection might be different, resulting in different annotation standards and granularity. Meanwhile, since most datasets are annotated for training specialist models like nnU-Net [26], precise and consistent terminology or expression for anatomical targets is often ignored. Therefore, a unified label system is demanded to avoid potential contradictions when training on mixed datasets. (ii) some critical image statistics, such as intensity distribution and voxel spacing vary from dataset to dataset, hindering the model from learning consistent image representations across datasets. In the following, we present details for dataset integration and pre-processing, and how we address the abovementioned challenges.

Unifying Label System. While integrating different datasets, three procedures are performed to ensure a unified annotation system: (i) we manually check each anatomical target in each dataset and assign a medical term to it, which is guaranteed to be precise and unambiguous across datasets. For instance, the targets that require distinction between orientations, such as the left lung and right lung, are always identified according to the left and right of the human body. And the same anatomical targets from different datasets are named consistently. For example, the i -th lumbar vertebrae in both TotalSegmentator [94] and MRSpineSeg [68] are named with format “lumbar vertebrae i (Li)”; (ii) we adjust the annotations to minimize contradictions between overlapped classes. For example, considering that many organ segmentation datasets do not exclude lesions within organs, *e.g.*, AbdomenCT-1K and CT-ORG, we merged the lesion annotations with the corresponding infected organ annotations in other datasets to maintain consistency. (iii) the same anatomy may have been annotated with different hierarchies in different datasets. In such cases, we manually merge the fine-grained classes to generate additional classes as a complement to close the gap between datasets. For example, sub-regions of liver in Couinaud Liver [87] are merged and added as a new class “liver”. As we will keep collecting datasets to scale up SAT-DS, such a label system will be maintained and updated continuously.

Dataset Pre-processing. As properties of each dataset may greatly impact the training of the segmentation network [26], such as intensity distribution and voxel spacing, we deliberately apply some normalization procedures to all the datasets to ensure uniformity and compatibility between them. *Firstly*, all the images are reoriented to specific axcodes, respaced to a voxel size of $1 \times 1 \times 3 \text{ mm}^2$ and cropped to non-zero region. *Secondly*, we apply different intensity normalization strategies to CT, MRI and PET images, specifically, for CT images, intensity values are truncated to $[-500, 1000]$ and applied z-score normalization. For MRI and PET images, intensity values are clipped by 0.5% and 99.5% of the image, and then z-score normalized. During training, we randomly crop the image patch with a fixed size of $288 \times 288 \times 96$. Random zoom-in,

zoom-out, and intensity scaling are applied for data augmentation.

Dataset Statistics. After integrating datasets, we derive a segmentation data collection that covers 497 segmentation classes, far outpacing each single dataset in both diversity and scale. We divide human body into eight regions, and classify each class into them manually. Fig. 12 (b) and (c) show the distribution of classes and annotations across different human body regions. We further show the distribution of some example classes in each region in Fig. 12 (a). The extensive range of categories and regions lays the foundation for the SAT’s wide application scenarios. The data collection is more than **fourth times** the size of the largest dataset (BraTS2023-GLI) in terms of volume number, and nearly **triple** the most comprehensive dataset (DAP Atlas) in terms of the class number.

Discussion. In the process of building SAT-DS, we merge a wide range of segmentation tasks, and establishing a unified label system by using natural language/text. Generally speaking, there are three advantages to do this: (i) natural language is powerful and discriminative, that enables better differentiation of the medical terminologies in the language embedding space; (ii) as shown in previous work [97, 103, 41, 108], knowledge-enhanced representation learning for the text encoder demonstrates promising performance, allowing to learn the implicit or explicit relationships between these segmentation targets. For example, segmenting a specific lobe of the liver requires the exact segmentation of liver as an organ in abdomen cavity, and shall be facilitated by referring to other parts of the liver. Therefore, establishing such connections via systematic medical knowledge shall be beneficial. (iii) text prompt can be given automatically without any human intervention, for instance, from large language model. This would pave the way for building a universal segmentation model that can be flexibly integrated into foundation models for generalist medical artificial intelligence, as a powerful grounding tool.

4.2 Universal Segmentation Prompted by Text

Towards building up our universal segmentation model by text prompt, we consider two main stages, namely, multimodal knowledge injection and universal segmentation training. In the following, we start by defining the problem scenario (Sec. 4.2.1). Then, we show how to structure multimodal medical knowledge and inject it into a text encoder (Sec. 4.2.2). Lastly, we employ the text encoder to guide our universal segmentation model training on SAT-DS dataset (Sec. 4.2.3).

4.2.1 Problem Formulation

Assuming we have a segmentation dataset collection, *i.e.*, $\mathcal{D} = \{(x_1, y_1; T_1), \dots, (x_K, y_K; T_K)\}$, where $x_i \in \mathbb{R}^{H \times W \times D \times C}$ denotes the image scan, $y_i \in \mathbb{R}^{H \times W \times D \times M}$ is the binary segmentation annotations of the anatomical targets in the image and $T_i = \{t_1, t_2, \dots, t_M\}$ denote the corresponding medical terminology set. The universal segmentation task can be formulated as:

$$\hat{y}_i = \Phi_{\text{SAT}}(\Phi_{\text{visual}}(x_i), \Phi_{\text{text}}(T_i)), \quad (1)$$

where Φ_{visual} is a visual encoder, Φ_{text} is a text encoder, Φ_{SAT} is a universal segmentation model and ideally Note that x_i can be an image scan from any modality of the anatomical region, and T_i can contain an arbitrary number of text-based medical terminologies of interest.

4.2.2 Multimodal Knowledge Injection

Here, we aim to inject rich multimodal medical knowledge into the visual and text encoders. The section starts from the procedure for structuring the multimodal medical knowledge data, and further presents details to use them for visual-language pre-training.

Multimodal Domain Knowledge Construction. As shown in Fig. 13 (a), the data from UMLS, search engine, and segmentation datasets can be aggregated into two formats:

- **Textual Medical Concept Pair.** For text-only knowledge, each concept t_i is associated with a definition p_i , constructing pairs of text $(t_i; p_i)$. We also derive a knowledge graph that connects the medical concepts through abundant triplet relationships (t_i, r_{ij}, t_j) . This graph can be alternatively

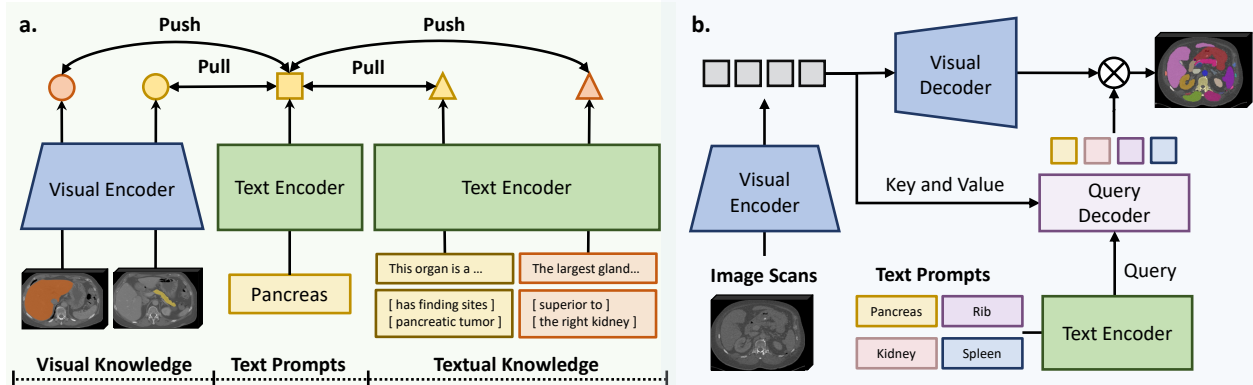


Figure 13 | Overview of SAT. (a) We inject multi-modal medical knowledge into knowledge encoders via contrastive learning. The knowledge is in different formats: atlas segmentation, concepts(terminologies), definitions, and relationships between concepts. We devise visual and text encoder to embed them; (b) We train a universal segmentation network based on the text prompts from the pre-trained text encoder. It is capable of segmenting a wide range of targets for image scans from different modalities and anatomical regions.

seen as a specialized text pair, $(t_i + r_{ij}; t_j)$ or $(t_i; r_{ij} + t_j)$, where ‘+’ refers to string concatenation. In this way, we can thus unify the two kinds of textual knowledge.

- **Visual Medical Concept Pair.** To align with the segmentation task, we gather pairs consisting of a concept (can be either an anatomical structure or lesion) and its image atlas. Note that, multiple pairs could be extracted from a single image. These pairs share a similar format to the segmentation data, denoted as $(x_i, y_i; t_i)$, where x_i and t_i are consistent with their definition in Sec. 4.2.1 and $y_i \in \mathbb{R}^{H \times W \times D \times 1}$ is a binary segmentation mask for t_i .

In summary, all the knowledge can either be represented as pure text description, *e.g.*, $t_i, p_i, t_i + r_{ij}, r_{ij} + t_j$, or atlas segmentation (x_i, y_i) , and paired further.

Visual-Language Pre-training. As shown in Fig. 13 (a), for pure text description, we encode them with a BERT [33] pre-trained on PubMed abstract [39]:

$$z = \Phi_{\text{text}}(\mathbf{t}), \mathbf{t} \in [t_i, p_i, t_i + r_{ij}, r_{ij} + t_j], z \in \mathbb{R}^d, \quad (2)$$

where d refers to the feature dimension. For visual concepts, we adopt the visual encoder Φ_{visual} . Given the excellent robustness and performance of U-Net [26, 81], we apply a standard 3D U-Net encoder to extract multi-scale image embeddings:

$$V_i = \{v_{i1}, v_{i2}, \dots, v_{iS}\} = \Phi_{\text{visual}}(x_i), v_{is} \in \mathbb{R}^{H_s \times W_s \times D_s \times d_s}, \quad (3)$$

where V_i is the multi-scale feature maps from U-Net encoder layers, and H_s, W_s, D_s, d_s are the spatial resolutions and channel width at different layers. We further average ROI pooling on these feature maps respectively, based on the down-sampled segmentation mask fitting resolutions at different layers. The concatenated pooled features can thus be treated as representation of the anatomical target on this image, containing multi-scale visual clues for it.

$$z = \mathcal{F}_{\text{pooling}}(\Phi_{\text{visual}}(x_i); y_i), z \in \mathbb{R}^d. \quad (4)$$

We train the visual encoder and text encoder by maximizing the similarities between all positive knowledge pairs, linked by text prompts (medical terminology names), as shown in Fig. 13. Specifically, given $(x_i, y_i; t_i), (t_i; p_i), (t_i + r_{ij}; t_j), (t_i; r_{ij} + t_j)$, for simplicity, we denote all the encoded features as z , regardless

of their modality format. For a batch of N pairs $\{(z_1, z'_1), \dots, (z_N, z'_N)\}$, we have:

$$\mathcal{L}_{\text{knowledge}} = -\frac{1}{N} \sum_{i=1}^N \left(\log \frac{\exp(z_i \cdot z'_i / \tau)}{\sum_{k=1}^N \mathbb{1}_{i \neq k} \exp(z_i \cdot z'_k / \tau)} + \log \frac{\exp(z_i \cdot z'_i / \tau)}{\sum_{k=1}^N \mathbb{1}_{i \neq k} \exp(z_k \cdot z'_i / \tau)} \right), \quad (5)$$

with $\tau = 0.07$ as temperature.

Discussion. On formulation, this procedure resembles a typical contrastive learning pipeline [76, 47, 102]. However, different from previous work that directly contrasting the paired visual-language data, we aim for knowledge-enhanced representation learning. By maximizing the similarities between the constructed positive textual and visual feature pairs, we force the text encoders to construct neural representations for medical concepts based on domain knowledge from two aspects: (i) through the well-established knowledge graph in text form, the text encoder enables to encode relationships between concepts in the latent space; (ii) the model captures the characteristics of anatomical structures and lesions via both visual atlas segmentations and detailed definitions. Therefore, in contrast to the one-hot labeling that treats each anatomical target as if being independent, such continuous neural representation shall provide more helpful guidance for the segmentation task.

4.2.3 Universal Segmentation Training

With the pre-trained visual and text encoder, we now continue the procedure for building the universal segmentation model with text as prompts. Fig. 13 (b) demonstrates the overall framework. Specifically, apart from the pre-trained visual and text encoders, the segmentation model consists of three more components: a visual decoder Φ_{dec} , a query decoder Φ_{query} , and a mask generator.

Although a sample in the segmentation dataset collection $(x_i, y_i; T_i)$ may contain multiple annotations, *i.e.*, $T_i = \{t_1, t_2, \dots, t_M\}$, for simplicity, we first describe the segmentation procedure for one target (t_i) .

Terminology Encoding. We use the pre-trained text encoder to generate neural embedding for the anatomical target as a text prompt for segmentation:

$$z_i = \Phi_{\text{text}}(t_i), \quad z_i \in \mathbb{R}^d. \quad (6)$$

Note that, after pre-training the text encoder with domain knowledge injection, z_i should contain both the textual background information and visual information from atlas samples.

Visual Encoding. We adopt the pre-trained visual encoder as explained in Sec. 4.2.2, Equa. 3, and continue training it.

Visual Decoding. In the visual decoder, the feature maps from the encoder are gradually upsampled with skip connections, effectively following the U-Net architecture [26, 81], ending up with per-pixel dense feature:

$$u_i = \Phi_{\text{dec}}(V_i), \quad u_i \in \mathbb{R}^{H \times W \times D \times d'}, \quad (7)$$

where d' is the dimension for the per-pixel dense feature after recovering to the original resolution.

Query Decoder. Although a general representation of the anatomical target is derived from the pre-trained text encoder with a text prompt, visual variations may still exist from patient to patient, we thus insert a transformer-based query module to further enhance the text prompts with visual clues. In practice, this module consists of 6 standard transformer decoders [90], that treats text embedding as query, and the pooled multi-scale visual features from the U-Net encoder as key, values, formulated as:

$$q_i = \Phi_{\text{query}}(V_i, z_i), \quad q_i \in \mathbb{R}^d. \quad (8)$$

Where z_i is consistent with z in Equa. 4. Therefore q_i can be seen as an adapted representation of the anatomical target in specific image scan x_i .

Mask Generator. By conducting pixel-wise dot-product between the representation of the anatomical target and the fine-grained per-pixel embedding, we can acquire a per-pixel prediction:

$$\hat{y}_i = \sigma(g(q_i) \cdot u_i), \hat{y}_i \in \mathbb{R}^{H \times W \times D}, \quad (9)$$

where $g(\cdot)$ is a feed-forward layer projecting q_i to a consistent dimension with the dense feature map u_i , and $\sigma(\cdot)$ denotes the sigmoid function. Note that, the whole forward procedure do not involve any operation between different text prompts. Therefore, for input with multiple text prompts or segmentation targets, *i.e.*, $T_i = \{t_1, t_2, \dots, t_M\}$, the processes described in Equation 6, 8 and 9 will be executed for each targets in parallel, and we could derive $\hat{y}_i \in \mathbb{R}^{H \times W \times D \times M}$.

Training Objective. Following [26], we adopt a loss function as the sum of binary cross-entropy loss and dice loss. For a sample with M classes and C voxels, we denote $p_{c,m}$ and $s_{c,m}$ the prediction and ground-truth for c -th pixel respectively on class m , the loss is:

$$\mathcal{L} = \underbrace{-\frac{1}{M} \sum_{m=1}^M \frac{1}{C} \sum_{c=1}^C p_{c,m} \cdot \log s_{c,m}}_{\text{Binary Cross Entropy Loss}} + \underbrace{\left(1 - \frac{2 \sum_{i=1}^M \sum_{c=1}^C p_{c,m} \cdot s_{c,m}}{\sum_{m=1}^M \sum_{c=1}^C p_{c,m}^2 + \sum_{m=1}^M \sum_{c=1}^C s_{c,m}^2}\right)}_{\text{Dice Loss}} \quad (10)$$

4.3 Implement Details

We encounter several challenges in training on the combined large number of heterogeneous medical datasets in 3D format. In this section, we provide details on the adopted training strategies.

Progressive Multimodal Knowledge Injection. For the stability of training, we implement the multimodal knowledge injection procedure introduced in Sec. 4.2.2 progressively. At the beginning, the text encoder is pretrained on the text knowledge via contrastive learning, *i.e.*, the textual medical concept pairs. The maximal sequence length after tokenization is 256, for even longer text input, we apply random truncation to fully exploit the knowledge in the long text. After convergence, to align text representations and visual features, we apply contrastive learning between the finetuned text encoder and the visual encoder on the visual medical concept pair.

Pre-processing Segmentation Dataset. We take voxel spacing as $1 \times 1 \times 3 \text{ mm}^2$ and patch size $288 \times 288 \times 96$, based on two empirical considerations: (i) when mixing the various datasets, scans with a wide range of voxel spacings ought to be normalized before processing in the same convolutional network. While resampling to larger voxel spacing may lose information, smaller voxel spacing will generate artifacts; (ii) a larger receptive field generally ensures better segmentation performance for most targets, however, increasing patch size will result in higher computational cost. We strike a balance between them based on the computational resources in use.

Balancing Segmentation Datasets. To balance between all datasets, we set the sampling strategy for each scan based on two intuitions respectively: (i) training case number varies significantly from dataset to dataset, which should be alleviated. We follow [89] and set the sampling weight of all scans in a dataset as the inverse proportion to \sqrt{N} , N is the number of training cases in the dataset; (ii) scans with larger annotation areas or more annotated classes should be sampled more as they are often harder to learn. Thus, we repeat such scans for R times in the sampling pool, where $R = \frac{S_{roi}}{288 \times 288 \times 96} \times \frac{M}{32}$. S_{roi} is size of the annotated area in a image scan, namely, its foreground area; $288 \times 288 \times 96$ is the patch size to crop; c is the number of annotated classes on it; and 32 is the maximal number of text prompts in a batch.

Balancing Segmentation Classes. While cropping the image scan, it’s a common practice [26] to over-sample foreground crops, *i.e.*, crops containing at least one segmentation target. However, weighting these crops evenly may ignore the unbalanced spatial distribution of segmentation targets. For example, in large scans with numerous annotations, tiny targets are harder to sample and thus may be ignored by the model. Thus, in foreground oversampling, we give more weight on regions with more segmentation targets.

Difference between SAT-Pro and SAT-Nano. We devise two variants of SAT with different model sizes

in visual backbone. For SAT-Nano, we adopt a U-Net with 6 blocks in-depth, each block has 2 convolutional layers and 3×3 size each kernel. The channel widths for each stage are [64, 64, 128, 256, 512, 768]; SAT-Pro share the same architecture with SAT-Nano, except that each block consists of 3 convolutional layers, and the channel widths are doubled to [128, 128, 256, 512, 1024, 1536].

Other Hyperparameter Details. The query decoder is a 6-layer standard transformer decoder with 8 heads in each attention module. Feature dimensions of a text prompt $d = 768$ and per-pixel embedding $d' = 64$. To unify the features from visual backbone variants with varying channel widths, they are projected to $d = 768$ with different feed-forward layers, and input as key and value to query decoder. For images with multiple segmentation targets, we set the maximal text prompts sampled in a batch of up to 32. A combination of cross-entropy loss and dice loss is applied as supervision at training time. We use AdamW [51] as the optimizer with cosine annealing schedule, maximal $lr = 1 \times 10^{-4}$, 10000 steps for warm-up. The SAT-Nano is trained on 8 NVIDIA A100 GPUs with 80GB memory, using maximal batch size 2; while the SAT-Pro is trained on 16 NVIDIA A100 GPUs with 80GB memory, using maximal batch size 1.

4.4 Evaluation Settings

4.4.1 Evaluation Datasets

To strike a balance between extensive experiments and computational cost, we utilize two collection of datasets:

- **SAT-DS.** As describe in Sec. 4.1.2, this contains all the 72 datasets, 497 classes from all human body regions, 22,186 image scans and 302,033 segmentation annotations.
- **SAT-DS-Nano.** A subset of SAT-DS, including only 49 datasets, 13,303 images and 151,461 annotations. Note that SAT-DS-Nano also covers 429 classes from all human body regions, adequate to evaluate universal segmentation task.

The detailed composition of SAT-DS and SAT-DS-Nano can be found in supplementary material Table 32 and Table 33. As there is no existing benchmark for evaluating the universal segmentation model, we randomly split each dataset into 80% for training and 20% for testing: (i) datasets may share the same images but with different classes. For example, Couinaud Liver provides fine-grained liver segmentation on a subset of MSD Hepatic Vessel. We carefully split the Couinaud Liver to make sure the test set will not be leaked in the train set of MSD Hepatic Vessel; (ii) scans of the same patient but different modalities are treated as different samples during training and evaluation. For example, MSD Prostate contains T2 and ADC scans of each patient. However, they share the same structure on the image. To avoid potential data leaking, we carefully split such datasets by patient id. Note that when involving segmentation datasets in the visual-language pretraining, we only use the training data to avoid potential data leaking. For datasets involved in SAT-DS-Nano, we keep their splits the same as in SAT-DS. The download link for each datasets can be found in Sec. 7, and we have released our dataset processing code and train-test splits to the research community for reproduction and benchmarking.

4.4.2 Baseline

Specialist Model. We take nnU-Net [26], U-Mamba [56] and SwinUNETR [18] as representative and strong baselines for comparison, which specializes in a series of configurations for each dataset. For a comprehensive evaluation, we train one specialist model on each of the datasets. Note that, following [94], we split Totalsegmentator into 6 subsets and train 6 different nnU-Net models. Similarly, datasets such as CHAOS with both MRI and CT images are treated as two different datasets. When training specialist models on each dataset, we adopt a multi-class segmentation setting and deliver the masks of all categories in this dataset at once. We derive the optimal network architecture and pre-processing pipeline with the default setting of each specialist model. We present the detailed network design of nnU-Nets in supplementary material Table 26 and Table 27 for a straightforward comparison. In summary, we train an assemble of 72 models for specialist model, that are customized on each dataset and serve as the competitive baseline for

evaluation. We adopt the latest official implementation of nnU-Net v2⁸ and U-Mamba⁹ in practice. The SwinUNETR is adopted to the same auto-configuration framework as U-Mamba.

Interactive Segmentation Model. We take MedSAM [55] as a representative interactive universal segmentation model as baseline. MedSAM finetunes SAM [34] on 86 segmentation datasets, and supports 2D medical image segmentation with box prompts. We follow the official implement¹⁰ to process and infer image slice by slice, and calculate the metrics on the finally stacked 3D prediction. For each single target on a slice, to simulate box prompts towards it, we both take the minimum rectangle containing the ground truth segmentation (Tight), and following the official data augmentation procedure, randomly shift each corner up to 8% of the whole image resolution (Loose). In addition, we consider directly use the tight box prompts as prediction (Oracle Box).

Text-Prompted Segmentation Model. We take BiomedParse [107], a concurrent work for universal 2D bio-medical images segmentation, as baseline. We follow the official implement¹¹ for data processing, inference and post-filtering. Similar to MedSAM, we process and infer image slice by slice, and calculate the metrics on the finally stacked 3D prediction. As BiomedParse may fail to detect the target on the slice, we evaluate it under two settings: only prompt target present in the current slice (Oracle) and prompt all the targets available in the dataset and post-filter out potential false positive predictions by p-values.

4.4.3 Evaluation Protocols

Given our goal is to develop a universal medical segmentation model, this provides opportunities to evaluate novel perspectives in addition to the traditional evaluation per dataset. Specifically, we conduct the internal evaluations from three dimensions:

- **Class-wise Evaluation.** As SAT is capable of segmenting a wide range of anatomical targets across the human body, we merge the results from the same classes across datasets to indicate the performance on each anatomical target. Specifically, we follow macro-average method: for a class annotated in multiple datasets, we first calculate its average scores within each dataset, and then average them over all datasets. Note that, the same anatomical structures or lesions from different modalities are treated as different classes in this work, *e.g.*, liver in both CT and MRI images.
- **Region-wise Evaluation.** In general, anatomical structures from the same human body region are closely connected and more likely to be involved in diagnosis within the same hospital department. Here, we consider the region-wise evaluation: based on class-wise evaluation, we merge results from all classes in the same body region, as to indicate the general performance in this region. For classes existing in multiple regions, we classify them into ‘Whole Body’ category. In addition, we report results for lesions classes independently as a category ‘lesion’, instead of merging them into specific regions.
- **Dataset-wise Evaluation.** Results of the classes within the same dataset are averaged to indicate the performance on this dataset. This is the same as the conventional evaluation protocol of specialist segmentation models trained on a single dataset.

4.4.4 Evaluation Metrics

We quantitatively evaluate the segmentation performance from the perspective of region and boundary metrics [60], *e.g.*, Dice Similarity Coefficient (DSC) and Normalized Surface Distance (NSD) respectively.

DSC. Dice Similarity Coefficient (DSC) is a standard region-based metric for medical image segmentation evaluation. It measures the overlap between model’s prediction P and ground truth G , formally defined as:

$$DSC(P, G) = \frac{2|P \cap G|}{|P| + |G|}. \quad (11)$$

NSD. Normalized Surface Distance (NSD) [66] is a boundary-based metric that measures the consistency at

⁸<https://github.com/MIC-DKFZ/nnUNet/>

⁹<https://github.com/bowang-lab/U-Mamba/>

¹⁰<https://github.com/bowang-lab/MedSAM>

¹¹<https://github.com/microsoft/BiomedParse>

the boundary area of the model’s prediction P and ground truth G , which is defined as:

$$NSD(P, G) = \frac{|\partial P \cap B_{\partial G}| + |\partial G \cap B_{\partial P}|}{|\partial P| + |\partial G|}, \quad (12)$$

where $B_{\partial P} = \{x \in \mathbf{R}^3 | \exists \hat{x} \in \partial P, \|x - \hat{x}\| \leq \tau\}$ and $B_{\partial G} = \{x \in \mathbf{R}^3 | \exists \hat{x} \in \partial G, \|x - \hat{x}\| \leq \tau\}$ are the boundary area of model’s prediction and ground truth at a tolerance τ , respectively. We set τ as 1 in the experiments.

5 Conclusion

In this paper, we promote the progress of medical universal segmentation with medical terminologies as text prompt, and knowledge enhancement. We build up the largest and most comprehensive 3D medical segmentation dataset, and the first multi-modal knowledge tree for human anatomy. In contrast to existing segmentation methods that requires training and deploying a series of specialized models, or limited to box/point prompts, our model, **SAT**, enables text-driven universal segmentation on 3 radiological modalities, 497 anatomical structures or lesions, across 8 main human body parts in just one model, demonstrates great efficiency and flexibility in application. We proposed SAT-Nano (110M parameters) and SAT-Pro (447M parameters), demonstrating superior or comparable performance to 72 specialist models, *i.e.*, nnU-Nets, U-Mamba or SwinUNETR, with billions of parameters and trained individually on each datasets, and showing even superior generalization ability on external datasets. SAT-Pro can also act as a foundation segmentation model, adapted to specific tasks for improved performance. Compared with the state-of-the-art interactive segmentation model, *i.e.*, MedSAM, SAT achieves superior performance, scalability and robustness with text as prompts. SAT is superior over BiomedParse, another concurrent work on text-prompted universal segmentation model, in both internal and external experiments. We further demonstrate the usage of SAT as a powerful out-of-the-box agent for large language models, seamlessly providing grounding ability in versatile applications. In summary, we believe our work can enhance high-performance, versatile, efficient and user-friendly medical segmentation in a wide range of applications, and contribute substantially to the development of generalist medical artificial intelligence.

6 Code Availability

The code is available at <https://github.com/zhaoziheng/SAT>.

7 Data Availability of SAT-DS

The access to each dataset can be found in Tab. 1 and Tab. 2. The data process code to build SAT-DS and our train-test splits for reproducibility and benchmarking are available at <https://github.com/zhaoziheng/SAT-DS>.

Table 1 | Download links of the 72 datasets in SAT-DS.

Dataset	Download Link
AbdomenCT1K [59]	https://github.com/JunMa11/AbdomenCT-1K
ACDC [9]	https://humanheart-project.creatis.insa-lyon.fr/database/
AMOS CT [29]	https://zenodo.org/records/7262581
AMOS MRI [29]	https://zenodo.org/records/7262581
ATLASR2 [46]	http://fcon_1000.projects.nitrc.org/indi/retro/atlas.html
ATLAS [75]	https://atlas-challenge.u-bourgogne.fr
autoPET [16]	https://wiki.cancerimagingarchive.net/pages/viewpage.action?pageId=93258287
Brain Atlas [85]	http://brain-development.org/
BrainPTM [5]	https://braiptm-2021.grand-challenge.org/
BraTS2023 GLI [62]	https://www.synapse.org/#!Synapse:syn51514105
BraTS2023 MEN [36]	https://www.synapse.org/#!Synapse:syn51514106
BraTS2023 MET [64]	https://www.synapse.org/#!Synapse:syn51514107
BraTS2023 PED [32]	https://www.synapse.org/#!Synapse:syn51514108
BraTS2023 SSA [2]	https://www.synapse.org/#!Synapse:syn51514109
BTCV Abdomen [38]	https://www.synapse.org/#!Synapse:syn3193805/wiki/217789
BTCV Cervix [38]	https://www.synapse.org/#!Synapse:syn3193805/wiki/217790
CHAOS CT [31]	https://chaos.grand-challenge.org/
CHAOS MRI [31]	https://chaos.grand-challenge.org/
CMRxMotion [92]	https://www.synapse.org/#!Synapse:syn28503327/files/
Couinaud [87]	https://github.com/GLCUnet/dataset
COVID-19 CT Seg [57]	https://github.com/JunMa11/COVID-19-CT-Seg-Benchmark
CrossMoDA2021 [14]	https://crossmoda.grand-challenge.org/Data/
CT-ORG [79]	https://wiki.cancerimagingarchive.net/pages/viewpage.action?pageId=61080890
CTPelvic1K [49]	https://zenodo.org/record/4588403#YEyLq_0zaCo
DAP Atlas [28]	https://github.com/alexanderjaus/AtlasDataset
FeTA2022 [69]	https://feta.grand-challenge.org/data-download/
FLARE22 [58]	https://flare22.grand-challenge.org/
FUMPE [61]	https://www.kaggle.com/datasets/andrewmvd/pulmonary-embolism-in-ct-images
HAN Seg [71]	https://zenodo.org/record/
HECKTOR2022 [3]	https://hecktor.grand-challenge.org/Data/
INSTANCE [45]	https://instance.grand-challenge.org/Dataset/
ISLES2022 [24]	http://www.isles-challenge.org/
KiPA22 [21]	https://kipa22.grand-challenge.org/dataset/
KiTS23 [23]	https://github.com/neheller/kits23
LAScarQS2022 Task 1 [43]	https://zmiclab.github.io/projects/lascarqs22/data.html
LAScarQS2022 Task 2 [43]	https://zmiclab.github.io/projects/lascarqs22/data.html
LNDb [70]	https://zenodo.org/record/7153205#Yz_oVHbMJPZ
LUNA16 [86]	https://luna16.grand-challenge.org/
MM-WHS CT [111]	https://mega.nz/folder/UNMF2YYI#1cqJVzo4p_wESv9P_pc8uA
MM-WHS MR [111]	https://mega.nz/folder/UNMF2YYI#1cqJVzo4p_wESv9P_pc8uA
MRSpineSeg [68]	https://www.cg.informatik.uni-siegen.de/en/spine-segmentation-and-analysis
MSD Cardiac [4]	http://medicaldecathlon.com/
MSD Colon [4]	http://medicaldecathlon.com/
MSD HepaticVessel [4]	http://medicaldecathlon.com/
MSD Hippocampus [4]	http://medicaldecathlon.com/

Table 2 | (Continued) Download links of the 72 datasets in SAT-DS.

Dataset	Download Link
MSD Liver [4]	http://medicaldecathlon.com/
MSD Lung [4]	http://medicaldecathlon.com/
MSD Pancreas [4]	http://medicaldecathlon.com/
MSD Prostate [4]	http://medicaldecathlon.com/
MSD Spleen [4]	http://medicaldecathlon.com/
MyoPS2020 [72]	https://mega.nz/folder/BRdnDISQ#FnCg9ykPITWYe5hrRZxi-w
NSCLC [8]	https://wiki.cancerimagingarchive.net/pages/viewpage.action?pageId=68551327
Pancreas CT [82]	https://wiki.cancerimagingarchive.net/display/public/pancreas-ct
Parse2022 [52]	https://parse2022.grand-challenge.org/Dataset/
PDDCA [78]	https://www.imagenglab.com/newsite/pddca/
PROMISE12 [48]	https://promise12.grand-challenge.org/Details/
SEGA [77]	https://multicenteraorta.grand-challenge.org/data/
SegRap2023 Task1 [53]	https://segrap2023.grand-challenge.org/
SegRap2023 Task2 [53]	https://segrap2023.grand-challenge.org/
SegTHOR [37]	https://competitions.codalab.org/competitions/21145#learn_the_details
SKII0 [40]	https://ambellan.de/sharing/QjrnLwah
SLIVER07 [22]	https://sliver07.grand-challenge.org/
ToothFairy [13]	https://ditto.ing.unimore.it/toothfairy/
TotalSegmentator Cardiac [94]	https://zenodo.org/record/6802614
TotalSegmentator Muscles [94]	https://zenodo.org/record/6802614
TotalSegmentator Organs [94]	https://zenodo.org/record/6802614
TotalSegmentator Ribs [94]	https://zenodo.org/record/6802614
TotalSegmentator Vertebrae [94]	https://zenodo.org/record/6802614
TotalSegmentator V2 [94]	https://zenodo.org/record/6802614
VerSe [84]	https://github.com/anjany/verse
WMH [35]	https://wmh.isi.uu.nl/
WORD [54]	https://github.com/HiLab-git/WORD

References

- [1] OpenAI (2023). Gpt-4 technical report, 2023.
- [2] Maruf Adewole, Jeffrey D. Rudie, Anu Gbadamosi, Oluyemisi Toyobo, Confidence Raymond, Dong Zhang, Olubukola Omidiji, Rachel Akinola, Mohammad Abba Suwaid, Adaobi Emegoakor, Nancy Ojo, Kenneth Aguh, Chinasa Kalaiwo, Gabriel Babatunde, Afolabi Ogunleye, Yewande Gbadamosi, Kator Iorpagher, Evan Calabrese, Mariam Aboian, Marius Linguraru, Jake Albrecht, Benedikt Wiestler, Florian Kofler, Anastasia Janas, Dominic LaBella, Anahita Fathi Kzerooni, Hongwei Bran Li, Juan Eugenio Iglesias, Keyvan Farahani, James Eddy, Timothy Bergquist, Verena Chung, Russell Takeshi Shinohara, Walter Wiggins, Zachary Reitman, Chunhao Wang, Xinyang Liu, Zhifan Jiang, Ariana Familiar, Koen Van Leemput, Christina Bukas, Maire Piraud, Gian-Marco Conte, Elaine Johansson, Zeke Meier, Bjoern H Menze, Ujjwal Baid, Spyridon Bakas, Farouk Dako, Abiodun Fatade, and Udunna C Anazodo. The brain tumor segmentation (brats) challenge 2023: Glioma segmentation in sub-saharan africa patient population (brats-africa), 2023.
- [3] V. Andrearczyk, V. Oreiller, M. Hatt, and A. Depeursinge. Overview of the hecktor challenge at miccai 2022: Automatic head and neck tumor segmentation and outcome prediction in pet/ct. In V. Andrearczyk, V. Oreiller, M. Hatt, and A. Depeursinge, editors, *Head and Neck Tumor Segmentation and Outcome Prediction. HECKTOR 2022. Lecture Notes in Computer Science*, volume 13626. Springer, Cham, 2023.
- [4] Michela Antonelli, Annika Reinke, Spyridon Bakas, Keyvan Farahani, Annette Kopp-Schneider, Bennett A Landman, Geert Litjens, Bjoern Menze, Olaf Ronneberger, Ronald M Summers, et al. The medical segmentation decathlon. *Nature communications*, 13(1):4128, 2022.
- [5] Itzik Avital, Ilya Nelkenbaum, Galia Tsarfaty, Eli Konen, Nahum Kiryati, and Arnaldo Mayer. Neural segmentation of seeding rois (srois) for pre-surgical brain tractography. *IEEE Transactions on Medical Imaging*, 39(5):1655–1667, 2019.
- [6] Wenjia Bai, Hideaki Suzuki, Jian Huang, Catherine Francis, Shuo Wang, Giacomo Tarroni, Florian Guitton, Nay Aung, Kenneth Fung, Steffen E Petersen, et al. A population-based phenome-wide association study of cardiac and aortic structure and function. *Nature medicine*, 26(10):1654–1662, 2020.
- [7] Ujjwal Baid, Satyam Ghodasara, Suyash Mohan, Michel Bilello, Evan Calabrese, Errol Colak, Keyvan Farahani, Jayashree Kalpathy-Cramer, Felipe C Kitamura, Sarthak Pati, et al. The rsna-asnr-miccai brats 2021 benchmark on brain tumor segmentation and radiogenomic classification. *arXiv preprint arXiv:2107.02314*, 2021.
- [8] Shaimaa Bakr, Olivier Gevaert, Sebastian Echegaray, Kelsey Ayers, Mu Zhou, Majid Shafiq, Hong Zheng, Jalen Anthony Benson, Weiruo Zhang, Ann NC Leung, et al. A radiogenomic dataset of non-small cell lung cancer. *Scientific Data*, 5(1):1–9, 2018.
- [9] Olivier Bernard, Alain Lalande, Clement Zotti, Frederick Cervenansky, Xin Yang, Pheng-Ann Heng, Irem Cetin, Karim Lekadir, Oscar Camara, Miguel Angel Gonzalez Ballester, et al. Deep learning techniques for automatic mri cardiac multi-structures segmentation and diagnosis: is the problem solved? *IEEE Transactions on Medical Imaging*, 37(11):2514–2525, 2018.
- [10] Olivier Bodenreider. The unified medical language system (umls): integrating biomedical terminology. *Nucleic acids research*, 32(suppl_1):D267–D270, 2004.
- [11] Hu Cao, Yueyue Wang, Joy Chen, Dongsheng Jiang, Xiaopeng Zhang, Qi Tian, and Manning Wang. Swin-unet: Unet-like pure transformer for medical image segmentation. In *European Conference on Computer Vision*, pages 205–218. Springer, 2022.
- [12] Jieneng Chen, Jieru Mei, Xianhang Li, Yongyi Lu, Qihang Yu, Qingyue Wei, Xiangde Luo, Yutong Xie, Ehsan Adeli, Yan Wang, et al. 3d transunet: Advancing medical image segmentation through vision transformers. *arXiv preprint arXiv:2310.07781*, 2023.
- [13] Marco Cipriano, Stefano Allegretti, Federico Bolelli, Mattia Di Bartolomeo, Federico Pollastri, Arrigo Pellacani, Paolo Minafra, Alexandre Anesi, and Costantino Grana. Deep segmentation of the mandibular canal: a new 3d annotated dataset of cbct volumes. *IEEE Access*, 10:11500–11510, 2022.

- [14] Reuben Dorent, Aaron Kujawa, Marina Ivory, Spyridon Bakas, Nicola Rieke, Samuel Joutard, Ben Glocker, Jorge Cardoso, Marc Modat, Kayhan Batmanghelich, Arseniy Belkov, Maria Baldeon Calisto, Jae Won Choi, Benoit M. Dawant, Hexin Dong, Sergio Escalera, Yubo Fan, Lasse Hansen, Mattias P. Heinrich, Smriti Joshi, Victoriya Kashtanova, Hyeon Gyu Kim, Satoshi Kondo, Christian N. Kruse, Susana K. Lai-Yuen, Hao Li, Han Liu, Buntheng Ly, Ipek Oguz, Hyungseob Shin, Boris Shirokikh, Zixian Su, Guotai Wang, Jianghao Wu, Yanwu Xu, Kai Yao, Li Zhang, Sébastien Ourselin, Jonathan Shapey, and Tom Vercauteren. Crossmoda 2021 challenge: Benchmark of cross-modality domain adaptation techniques for vestibular schwannoma and cochlea segmentation. *Medical Image Analysis*, 83:102628, 2023.
- [15] Qi Dou, Lequan Yu, Hao Chen, Yueming Jin, Xin Yang, Jing Qin, and Pheng-Ann Heng. 3d deeply supervised network for automated segmentation of volumetric medical images. *Medical Image Analysis*, 41:40–54, 2017.
- [16] Sergios Gatidis, Tobias Hepp, Marcel Früh, Christian La Fougère, Konstantin Nikolaou, Christina Pfannenbergl, Bernhard Schölkopf, Thomas Küstner, Clemens Cyran, and Daniel Rubin. A whole-body fdg-pet/ct dataset with manually annotated tumor lesions. *Scientific Data*, 9(1):601, 2022.
- [17] Albert Gu and Tri Dao. Mamba: Linear-time sequence modeling with selective state spaces. *arXiv preprint arXiv:2312.00752*, 2023.
- [18] Ali Hatamizadeh, Vishwesh Nath, Yucheng Tang, Dong Yang, Holger R Roth, and Daguang Xu. Swin unetr: Swin transformers for semantic segmentation of brain tumors in mri images. In *International MICCAI Brainlesion Workshop*, pages 272–284. Springer, 2021.
- [19] Ali Hatamizadeh, Vishwesh Nath, Yucheng Tang, Dong Yang, Holger R Roth, and Daguang Xu. Swin unetr: Swin transformers for semantic segmentation of brain tumors in mri images. In *International MICCAI Brainlesion Workshop*, pages 272–284. Springer, 2021.
- [20] Ali Hatamizadeh, Yucheng Tang, Vishwesh Nath, Dong Yang, Andriy Myronenko, Bennett Landman, Holger R Roth, and Daguang Xu. Unetr: Transformers for 3d medical image segmentation. In *Proceedings of the IEEE/CVF Winter Conference on Applications of Computer Vision*, pages 574–584, 2022.
- [21] Yuting He, Guanyu Yang, Jian Yang, Rongjun Ge, Youyong Kong, Xiaomei Zhu, Shaobo Zhang, Pengfei Shao, Huazhong Shu, Jean-Louis Dillenseger, et al. Meta grayscale adaptive network for 3d integrated renal structures segmentation. *Medical image analysis*, 71:102055, 2021.
- [22] Tobias Heimann, Bram Van Ginneken, Martin A Styner, Yulia Arzhaeva, Volker Aurich, Christian Bauer, Andreas Beck, Christoph Becker, Reinhard Beichel, György Bekes, et al. Comparison and evaluation of methods for liver segmentation from ct datasets. *IEEE Transactions on Medical Imaging*, 28(8):1251–1265, 2009.
- [23] Nicholas Heller, Fabian Isensee, Dasha Trofimova, Resha Tejpal, Zhongchen Zhao, Huai Chen, Lisheng Wang, Alex Golts, Daniel Khapun, Daniel Shats, et al. The kits21 challenge: Automatic segmentation of kidneys, renal tumors, and renal cysts in corticomedullary-phase ct. *arXiv preprint arXiv:2307.01984*, 2023.
- [24] Moritz R Hernandez Petzsche, Ezequiel de la Rosa, Uta Hanning, Roland Wiest, Waldo Valenzuela, Mauricio Reyes, Maria Meyer, Sook-Lei Liew, Florian Kofler, Ivan Ezhov, et al. Isles 2022: A multi-center magnetic resonance imaging stroke lesion segmentation dataset. *Scientific data*, 9(1):762, 2022.
- [25] Yuhao Huang, Xin Yang, Lian Liu, Han Zhou, Ao Chang, Xinrui Zhou, Rusi Chen, Junxuan Yu, Jiongquan Chen, Chaoyu Chen, et al. Segment anything model for medical images? *Medical Image Analysis*, 92:103061, 2024.
- [26] Fabian Isensee, Paul F Jaeger, Simon AA Kohl, Jens Petersen, and Klaus H Maier-Hein. nnu-net: a self-configuring method for deep learning-based biomedical image segmentation. *Nature Methods*, 18(2):203–211, 2021.
- [27] David A Jaffray, Felicia Knaul, Michael Baumann, and Mary Gospodarowicz. Harnessing progress in radiotherapy for global cancer control. *Nature Cancer*, 4(9):1228–1238, 2023.
- [28] Alexander Jaus, Constantin Seibold, Kelsey Hermann, Alexandra Walter, Kristina Giske, Johannes Haubold, Jens Kleesiek, and Rainer Stiefelhagen. Towards unifying anatomy segmentation: automated

generation of a full-body ct dataset via knowledge aggregation and anatomical guidelines. *arXiv preprint arXiv:2307.13375*, 2023.

- [29] Yuanfeng Ji, Haotian Bai, Chongjian Ge, Jie Yang, Ye Zhu, Ruimao Zhang, Zhen Li, Lingyan Zhanng, Wanling Ma, Xiang Wan, et al. Amos: A large-scale abdominal multi-organ benchmark for versatile medical image segmentation. *Advances in neural information processing systems*, 35:36722–36732, 2022.
- [30] Qiao Jin, Won Kim, Qingyu Chen, Donald C Comeau, Lana Yeganova, W John Wilbur, and Zhiyong Lu. Medcpt: Contrastive pre-trained transformers with large-scale pubmed search logs for zero-shot biomedical information retrieval. *Bioinformatics*, 39(11):btad651, 2023.
- [31] A Emre Kavur, N Sinem Gezer, Mustafa Barış, Sinem Aslan, Pierre-Henri Conze, Vladimir Groza, Duc Duy Pham, Soumick Chatterjee, Philipp Ernst, Savaş Özkan, et al. Chaos challenge-combined (ct-mr) healthy abdominal organ segmentation. *Medical Image Analysis*, 69:101950, 2021.
- [32] Anahita Fathi Kazerooni, Nastaran Khalili, Xinyang Liu, Debanjan Haldar, Zhifan Jiang, Syed Muhammed Anwar, Jake Albrecht, Maruf Adewole, Uduinna Anazodo, Hannah Anderson, Sina Bagheri, Ujjwal Baid, Timothy Bergquist, Austin J. Borja, Evan Calabrese, Verena Chung, Gian-Marco Conte, Farouk Dako, James Eddy, Ivan Ezhov, Ariana Familiar, Keyvan Farahani, Shuvanjan Haldar, Juan Eugenio Iglesias, Anastasia Janas, Elaine Johansen, Blaise V Jones, Florian Kofler, Dominic LaBella, Hollie Anne Lai, Koen Van Leemput, Hongwei Bran Li, Nazanin Maleki, Aaron S McAllister, Zeke Meier, Bjoern Menze, Ahmed W Moawad, Khanak K Nandolia, Julija Pavaine, Marie Piraud, Tina Poussaint, Sanjay P Prabhu, Zachary Reitman, Andres Rodriguez, Jeffrey D Rudie, Ibraheem Salman Shaikh, Lubdha M. Shah, Nakul Sheth, Russel Taki Shinohara, Wenxin Tu, Karthik Viswanathan, Chunhao Wang, Jeffrey B Ware, Benedikt Wiestler, Walter Wiggins, Anna Zapaishchykova, Mariam Aboian, Miriam Bornhorst, Peter de Blank, Michelle Deutsch, Maryam Fouladi, Lindsey Hoffman, Benjamin Kann, Margot Lazow, Leonie Mikael, Ali Nabavizadeh, Roger Packer, Adam Resnick, Brian Rood, Arastoo Vossough, Spyridon Bakas, and Marius George Linguraru. The brain tumor segmentation (brats) challenge 2023: Focus on pediatrics (cbtbn-connect-dipgr-asnr-miccai brats-peds), 2023.
- [33] Jacob Devlin Ming-Wei Chang Kenton and Lee Kristina Toutanova. Bert: Pre-training of deep bidirectional transformers for language understanding. In *Proceedings of Annual Conference of the North American Chapter of the Association for Computational Linguistics: Human Language Technologies (NAACL-HLT)*, pages 4171–4186, 2019.
- [34] Alexander Kirillov, Eric Mintun, Nikhila Ravi, Hanzi Mao, Chloe Rolland, Laura Gustafson, Tete Xiao, Spencer Whitehead, Alexander C Berg, Wan-Yen Lo, et al. Segment anything. In *Proceedings of the IEEE/CVF International Conference on Computer Vision*, pages 4015–4026, 2023.
- [35] Hugo J Kuijff, J Matthijs Biesbroek, Jeroen De Bresser, Rutger Heinen, Simon Andermatt, Mariana Bento, Matt Berseth, Mikhail Belyaev, M Jorge Cardoso, Adria Casamitjana, et al. Standardized assessment of automatic segmentation of white matter hyperintensities and results of the wmh segmentation challenge. *IEEE Transactions on Medical Imaging*, 38(11):2556–2568, 2019.
- [36] Dominic LaBella, Maruf Adewole, Michelle Alonso-Basanta, Talissa Altes, Syed Muhammad Anwar, Ujjwal Baid, Timothy Bergquist, Radhika Bhalerao, Sully Chen, Verena Chung, Gian-Marco Conte, Farouk Dako, James Eddy, Ivan Ezhov, Devon Godfrey, Fathi Hilal, Ariana Familiar, Keyvan Farahani, Juan Eugenio Iglesias, Zhifan Jiang, Elaine Johanson, Anahita Fathi Kazerooni, Collin Kent, John Kirkpatrick, Florian Kofler, Koen Van Leemput, Hongwei Bran Li, Xinyang Liu, Aria Mahtabfar, Shan McBurney-Lin, Ryan McLean, Zeke Meier, Ahmed W Moawad, John Mongan, Pierre Nedelec, Maxence Pajot, Marie Piraud, Arif Rashid, Zachary Reitman, Russell Takeshi Shinohara, Yury Velichko, Chunhao Wang, Pranav Warman, Walter Wiggins, Mariam Aboian, Jake Albrecht, Uduinna Anazodo, Spyridon Bakas, Adam Flanders, Anastasia Janas, Goldey Khanna, Marius George Linguraru, Bjoern Menze, Ayman Nada, Andreas M Rauschecker, Jeff Rudie, Nourel Hoda Tahon, Javier Villanueva-Meyer, Benedikt Wiestler, and Evan Calabrese. The asnr-miccai brain tumor segmentation (brats) challenge 2023: Intracranial meningioma, 2023.
- [37] Zoé Lambert, Caroline Petitjean, Bernard Dubray, and Su Kuan. Segthor: Segmentation of thoracic organs at risk in ct images. In *2020 Tenth International Conference on Image Processing Theory, Tools and Applications (IPTA)*, pages 1–6. IEEE, 2020.

- [38] Bennett Landman, Zhoubing Xu, J Igelsias, Martin Styner, T Langerak, and Arno Klein. Miccai multi-atlas labeling beyond the cranial vault—workshop and challenge. In *Proc. MICCAI Multi-Atlas Labeling Beyond Cranial Vault—Workshop Challenge*, volume 5, page 12, 2015.
- [39] Jinhyuk Lee, Wonjin Yoon, Sungdong Kim, Donghyeon Kim, Sunkyu Kim, Chan Ho So, and Jaewoo Kang. Biobert: a pre-trained biomedical language representation model for biomedical text mining. *Bioinformatics*, 36(4):1234–1240, 2020.
- [40] Soochahn Lee, Hackjoon Shim, Sang Hyun Park, Il Dong Yun, and Sang Uk Lee. Learning local shape and appearance for segmentation of knee cartilage in 3d mri. In *Medical Image Computing and Computer Assisted Intervention (MICCAI)*, pages 231–240, 2010.
- [41] Jiayu Lei, Lisong Dai, Haoyun Jiang, Chaoyi Wu, Xiaoman Zhang, Yao Zhang, Jiangchao Yao, Weidi Xie, Yanyong Zhang, Yuehua Li, et al. Unibrain: Universal brain mri diagnosis with hierarchical knowledge-enhanced pre-training. *arXiv preprint arXiv:2309.06828*, 2023.
- [42] Haolin Li, Yuhang Zhou, Ziheng Zhao, Siyuan Du, Jiangchao Yao, Weidi Xie, Ya Zhang, and Yanfeng Wang. Lorkd: Low-rank knowledge decomposition for medical foundation models. *arXiv preprint arXiv:2409.19540*, 2024.
- [43] Lei Li, Veronika A Zimmer, Julia A Schnabel, and Xiahai Zhuang. Atrialjsqnet: a new framework for joint segmentation and quantification of left atrium and scars incorporating spatial and shape information. *Medical image analysis*, 76:102303, 2022.
- [44] Xiaomeng Li, Hao Chen, Xiaojuan Qi, Qi Dou, Chi-Wing Fu, and Pheng-Ann Heng. H-denseunet: hybrid densely connected unet for liver and tumor segmentation from ct volumes. *IEEE Transactions on Medical Imaging*, 37(12):2663–2674, 2018.
- [45] Xiangyu Li, Gongning Luo, Kuanquan Wang, Hongyu Wang, Jun Liu, Xinjie Liang, Jie Jiang, Zhenghao Song, Chunyue Zheng, Haokai Chi, et al. The state-of-the-art 3d anisotropic intracranial hemorrhage segmentation on non-contrast head ct: The instance challenge. *arXiv preprint arXiv:2301.03281*, 2023.
- [46] Sook-Lei Liew, Bethany P Lo, Miranda R Donnelly, Artemis Zavalianos-Petropulu, Jessica N Jeong, Giuseppe Barisano, Alexandre Hutton, Julia P Simon, Julia M Juliano, Anisha Suri, et al. A large, curated, open-source stroke neuroimaging dataset to improve lesion segmentation algorithms. *Scientific data*, 9(1):320, 2022.
- [47] Weixiong Lin, Ziheng Zhao, Xiaoman Zhang, Chaoyi Wu, Ya Zhang, Yanfeng Wang, and Weidi Xie. Pmc-clip: Contrastive language-image pre-training using biomedical documents. In *International Conference on Medical Image Computing and Computer-Assisted Intervention*, pages 525–536. Springer, 2023.
- [48] Geert Litjens, Robert Toth, Wendy Van De Ven, Caroline Hoeks, Sjoerd Kerkstra, Bram Van Ginneken, Graham Vincent, Gwenael Guillard, Neil Birbeck, Jindang Zhang, et al. Evaluation of prostate segmentation algorithms for mri: the promise12 challenge. *Medical Image Analysis*, 18(2):359–373, 2014.
- [49] Pengbo Liu, Hu Han, Yuanqi Du, Heqin Zhu, Yinhao Li, Feng Gu, Honghu Xiao, Jun Li, Chunpeng Zhao, Li Xiao, Xinbao Wu, and S. Kevin Zhou. Deep learning to segment pelvic bones: large-scale ct datasets and baseline models. *International Journal of Computer Assisted Radiology and Surgery*, 16(5):749, 2021.
- [50] Yuanye Liu, Zheyao Gao, Nannan Shi, Fuping Wu, Yuxin Shi, Qingchao Chen, and Xiahai Zhuang. Merit: Multi-view evidential learning for reliable and interpretable liver fibrosis staging. *arXiv preprint arXiv:2405.02918*, 2024.
- [51] Ilya Loshchilov and Frank Hutter. Decoupled weight decay regularization. In *International Conference on Learning Representations*, 2018.
- [52] Gongning Luo, Kuanquan Wang, Jun Liu, Shuo Li, Xinjie Liang, Xiangyu Li, Shaowei Gan, Wei Wang, Suyu Dong, Wenyi Wang, et al. Efficient automatic segmentation for multi-level pulmonary arteries: The parse challenge. *arXiv preprint arXiv:2304.03708*, 2023.
- [53] Xiangde Luo, Jia Fu, Yunxin Zhong, Shuolin Liu, Bing Han, Mehdi Astaraki, Simone Bendazzoli, Iuliana Toma-Dasu, Yiwen Ye, Ziyang Chen, et al. Segrap2023: A benchmark of organs-at-risk and gross tumor volume segmentation for radiotherapy planning of nasopharyngeal carcinoma. *Medical Image Analysis*, page 103447, 2025.

- [54] X Luo, W Liao, J Xiao, J Chen, T Song, X Zhang, K Li, DN Metaxas, G Wang, and S Zhang. Word: A large scale dataset, benchmark and clinical applicable study for abdominal organ segmentation from ct image. *Medical Image Analysis*, 82:102642–102642, 2022.
- [55] Jun Ma, Yuting He, Feifei Li, Lin Han, Chenyu You, and Bo Wang. Segment anything in medical images. *Nature Communications*, 15(1):654, 2024.
- [56] Jun Ma, Feifei Li, and Bo Wang. U-mamba: Enhancing long-range dependency for biomedical image segmentation. *arXiv preprint arXiv:2401.04722*, 2024.
- [57] Jun Ma, Yixin Wang, Xingle An, Cheng Ge, Ziqi Yu, Jianan Chen, Qiongjie Zhu, Guoqiang Dong, Jian He, Zhiqiang He, et al. Toward data-efficient learning: A benchmark for covid-19 ct lung and infection segmentation. *Medical physics*, 48(3):1197–1210, 2021.
- [58] Jun Ma, Yao Zhang, Song Gu, Cheng Ge, Shihao Mae, Adamo Young, Cheng Zhu, Xin Yang, Kangkang Meng, Ziyang Huang, et al. Unleashing the strengths of unlabelled data in deep learning-assisted pancreatic abdominal organ quantification: the flare22 challenge. *The Lancet Digital Health*, 6(11):e815–e826, 2024.
- [59] Jun Ma, Yao Zhang, Song Gu, Cheng Zhu, Cheng Ge, Yichi Zhang, Xingle An, Congcong Wang, Qiyuan Wang, Xin Liu, et al. Abdomenct-1k: Is abdominal organ segmentation a solved problem? *IEEE Transactions on Pattern Analysis and Machine Intelligence*, 44(10):6695–6714, 2021.
- [60] Lena Maier-Hein, Annika Reinke, Patrick Godau, Minu D Tizabi, Florian Buettner, Evangelia Christodoulou, Ben Glocker, Fabian Isensee, Jens Kleesiek, Michal Kozubek, et al. Metrics reloaded: recommendations for image analysis validation. *Nature methods*, 21(2):195–212, 2024.
- [61] Mojtaba Masoudi, Hamid-Reza Pourreza, Mahdi Saadatmand-Tarzjan, Noushin Eftekhari, Fateme Shafiee Zargar, and Masoud Pezeshki Rad. A new dataset of computed-tomography angiography images for computer-aided detection of pulmonary embolism. *Scientific Data*, 5, 2018.
- [62] Bjoern H Menze, Andras Jakab, Stefan Bauer, Jayashree Kalpathy-Cramer, Keyvan Farahani, Justin Kirby, Yuliya Burren, Nicole Porz, Johannes Slotboom, Roland Wiest, et al. The multimodal brain tumor image segmentation benchmark (brats). *IEEE transactions on medical imaging*, 34(10):1993–2024, 2014.
- [63] Fausto Milletari, Nassir Navab, and Seyed-Ahmad Ahmadi. V-net: Fully convolutional neural networks for volumetric medical image segmentation. In *International Conference on 3D Vision (3DV)*, pages 565–571. Ieee, 2016.
- [64] Ahmed W. Moawad, Anastasia Janas, Ujjwal Baid, Divya Ramakrishnan, Leon Jekel, Kiril Krantchev, Harrison Moy, Rachit Saluja, Klara Osenberg, Klara Wilms, Manpreet Kaur, Arman Avesta, Gabriel Cassinelli Pedersen, Nazanin Maleki, Mahdi Salimi, Sarah Merkaç, Marc von Reppert, Niklas Tillmans, Jan Lost, Khaled Bousabarah, Wolfgang Holler, MingDe Lin, Malte Westerhoff, Ryan Maresca, Katherine E. Link, Nourel hoda Tahon, Daniel Marcus, Aristeidis Sotiras, Pamela LaMontagne, Strajit Chakrabarty, Oleg Teytelboym, Ayda Youssef, Ayaman Nada, Yuri S. Velichko, Nicolo Gennaro, Connectome Students, Group of Annotators, Justin Cramer, Derek R. Johnson, Benjamin Y. M. Kwan, Boyan Petrovic, Satya N. Patro, Lei Wu, Tiffany So, Gerry Thompson, Anthony Kam, Gloria Guzman Perez-Carrillo, Neil Lall, Group of Approvers, Jake Albrecht, Udunna Anazodo, Marius George Lingaru, Bjoern H Menze, Benedikt Wiestler, Maruf Adewole, Syed Muhammad Anwar, Dominic Labella, Hongwei Bran Li, Juan Eugenio Iglesias, Keyvan Farahani, James Eddy, Timothy Bergquist, Verena Chung, Russel Takeshi Shinohara, Farouk Dako, Walter Wiggins, Zachary Reitman, Chunhao Wang, Xinyang Liu, Zhifan Jiang, Koen Van Leemput, Marie Piraud, Ivan Ezhov, Elaine Johanson, Zeke Meier, Ariana Familiar, Anahita Fathi Kazerooni, Florian Kofler, Evan Calabrese, Sanjay Aneja, Veronica Chiang, Ichiro Ikuta, Umber Shafique, Fatima Memon, Gian Marco Conte, Spyridon Bakas, Jeffrey Rudie, and Mariam Aboian. The brain tumor segmentation (brats-mets) challenge 2023: Brain metastasis segmentation on pre-treatment mri, 2023.
- [65] Victor Nauffal, Marcus DR Klarqvist, Matthew C Hill, Danielle F Pace, Paolo Di Achille, Seung Hoan Choi, Joel T Rämö, James P Pirruccello, Pulkit Singh, Shinwan Kany, et al. Noninvasive assessment of organ-specific and shared pathways in multi-organ fibrosis using t1 mapping. *Nature Medicine*, pages 1–12, 2024.

- [66] Stanislav Nikolov, Sam Blackwell, Alexei Zverovitch, Ruheena Mendes, and et al. Clinically applicable segmentation of head and neck anatomy for radiotherapy: deep learning algorithm development and validation study. *Journal of Medical Internet Research*, 23(7):e26151, 2021.
- [67] Saman Nouranian, Mahdi Ramezani, Ingrid Spadinger, William J Morris, Septimu E Salcudean, and Purang Abolmaesumi. Learning-based multi-label segmentation of transrectal ultrasound images for prostate brachytherapy. *IEEE transactions on medical imaging*, 35(3):921–932, 2015.
- [68] Shumao Pang, Chunlan Pang, Lei Zhao, Yangfan Chen, Zhihai Su, Yujia Zhou, Meiyan Huang, Wei Yang, Hai Lu, and Qianjin Feng. Spineparsenet: spine parsing for volumetric mr image by a two-stage segmentation framework with semantic image representation. *IEEE Transactions on Medical Imaging*, 40(1):262–273, 2020.
- [69] Kelly Payette, Priscille de Dumast, Hamza Kebiri, Ivan Ezhov, Johannes C Paetzold, Suprosanna Shit, Asim Iqbal, Romesa Khan, Raimund Kottke, Patrice Grehten, et al. An automatic multi-tissue human fetal brain segmentation benchmark using the fetal tissue annotation dataset. *Scientific data*, 8(1):167, 2021.
- [70] João Pedrosa, Guilherme Aresta, Carlos Ferreira, Gurraj Atwal, Hady Ahmady Phoulady, Xiaoyu Chen, Rongzhen Chen, Jiaoliang Li, Liansheng Wang, Adrian Galdran, et al. Lndb challenge on automatic lung cancer patient management. *Medical image analysis*, 70:102027, 2021.
- [71] Gašper Podobnik, Primož Strojjan, Primož Peterlin, Bulat Ibragimov, and Tomaž Vrtovec. Han-seg: The head and neck organ-at-risk ct and mr segmentation dataset. *Medical physics*, 50(3):1917–1927, 2023.
- [72] Junyi Qiu, Lei Li, Sihan Wang, Ke Zhang, Yinyin Chen, Shan Yang, and Xiahai Zhuang. Myops-net: Myocardial pathology segmentation with flexible combination of multi-sequence cmr images. *Medical Image Analysis*, 84:102694, 2023.
- [73] Pengcheng Qiu, Chaoyi Wu, Xiaoman Zhang, Weixiong Lin, Haicheng Wang, Ya Zhang, Yanfeng Wang, and Weidi Xie. Towards building multilingual language model for medicine. *Nature Communications*, 15(1):8384, 2024.
- [74] Chongyu Qu, Tiezheng Zhang, Hualin Qiao, Yucheng Tang, Alan L Yuille, Zongwei Zhou, et al. Abdomenatlas-8k: Annotating 8,000 ct volumes for multi-organ segmentation in three weeks. *Advances in Neural Information Processing Systems*, 36, 2023.
- [75] Félix Quinton, Romain Popoff, Benoît Presles, Sarah Leclerc, Fabrice Meriaudeau, Guillaume Nodari, Olivier Lopez, Julie Pellegrinelli, Olivier Chevallier, Dominique Ginhac, et al. A tumour and liver automatic segmentation (atlas) dataset on contrast-enhanced magnetic resonance imaging for hepatocellular carcinoma. *Data*, 8(5):79, 2023.
- [76] Alec Radford, Jong Wook Kim, Chris Hallacy, Aditya Ramesh, Gabriel Goh, Sandhini Agarwal, Girish Sastry, Amanda Askell, Pamela Mishkin, Jack Clark, et al. Learning transferable visual models from natural language supervision. In *International conference on machine learning*, pages 8748–8763. PMLR, 2021.
- [77] Lukas Radl, Yuan Jin, Antonio Pepe, Jianning Li, Christina Gsaxner, Fen-hua Zhao, and Jan Egger. Avt: Multicenter aortic vessel tree cta dataset collection with ground truth segmentation masks. *Data in brief*, 40:107801, 2022.
- [78] Patrik F Raudaschl, Paolo Zaffino, Gregory C Sharp, Maria Francesca Spadea, Antong Chen, Benoit M Dawant, Thomas Albrecht, Tobias Gass, Christoph Langguth, Marcel Lüthi, et al. Evaluation of segmentation methods on head and neck ct: auto-segmentation challenge 2015. *Medical physics*, 44(5):2020–2036, 2017.
- [79] Blaine Rister, Darvin Yi, Kaushik Shivakumar, Tomomi Nobashi, and Daniel L Rubin. Ct-org, a new dataset for multiple organ segmentation in computed tomography. *Scientific Data*, 7(1):381, 2020.
- [80] Richard J Roberts. Pubmed central: The genbank of the published literature, 2001.
- [81] Olaf Ronneberger, Philipp Fischer, and Thomas Brox. U-net: Convolutional networks for biomedical image segmentation. In *Medical Image Computing and Computer-Assisted Intervention (MICCAI)*, pages 234–241. Springer, 2015.

- [82] Holger R Roth, Le Lu, Amal Farag, Hoo-Chang Shin, Jiamin Liu, Evrim B Turkbey, and Ronald M Summers. Deeporgan: Multi-level deep convolutional networks for automated pancreas segmentation. In *Medical Image Computing and Computer-Assisted Intervention–MICCAI 2015: 18th International Conference, Munich, Germany, October 5-9, 2015, Proceedings, Part I 18*, pages 556–564. Springer, 2015.
- [83] Jo Schlemper, Ozan Oktay, Michiel Schaap, Mattias Heinrich, Bernhard Kainz, Ben Glocker, and Daniel Rueckert. Attention gated networks: Learning to leverage salient regions in medical images. *Medical Image Analysis*, 53:197–207, 2019.
- [84] Anjany Sekuboyina, Malek E Hussein, Amirhossein Bayat, Maximilian Löffler, Hans Liebl, Hongwei Li, Giles Tetteh, Jan Kukačka, Christian Payer, Darko Štern, et al. Verse: A vertebrae labelling and segmentation benchmark for multi-detector ct images. *Medical image analysis*, 73:102166, 2021.
- [85] Ahmed Serag, Paul Aljabar, Gareth Ball, Serena J Counsell, James P Boardman, Mary A Rutherford, A David Edwards, Joseph V Hajnal, and Daniel Rueckert. Construction of a consistent high-definition spatio-temporal atlas of the developing brain using adaptive kernel regression. *Neuroimage*, 59(3):2255–2265, 2012.
- [86] Arnaud Arindra Adiyoso Setio, Alberto Traverso, Thomas De Bel, Moira SN Berens, Cas Van Den Bogaard, Piergiorgio Cerello, Hao Chen, Qi Dou, Maria Evelina Fantacci, Bram Geurts, et al. Validation, comparison, and combination of algorithms for automatic detection of pulmonary nodules in computed tomography images: the luna16 challenge. *Medical image analysis*, 42:1–13, 2017.
- [87] Jiang Tian, Li Liu, Zhongchao Shi, and Feiyu Xu. Automatic couinaud segmentation from ct volumes on liver using glc-unet. In *International Workshop on Machine Learning in Medical Imaging*, pages 274–282. Springer, 2019.
- [88] Hugo Touvron, Louis Martin, Kevin Stone, Peter Albert, Amjad Almahairi, Yasmine Babaei, Nikolay Bashlykov, Soumya Batra, Prajjwal Bhargava, Shruti Bhosale, et al. Llama 2: Open foundation and fine-tuned chat models. *arXiv preprint arXiv:2307.09288*, 2023.
- [89] Constantin Ulrich, Fabian Isensee, Tassilo Wald, Maximilian Zenk, Michael Baumgartner, and Klaus H Maier-Hein. Multitalent: A multi-dataset approach to medical image segmentation. In *International Conference on Medical Image Computing and Computer-Assisted Intervention*, pages 648–658. Springer, 2023.
- [90] Ashish Vaswani, Noam Shazeer, Niki Parmar, Jakob Uszkoreit, Llion Jones, Aidan N Gomez, Łukasz Kaiser, and Illia Polosukhin. Attention is all you need. *Advances in Neural Information Processing Systems*, 30, 2017.
- [91] Haoyu Wang, Sizheng Guo, Jin Ye, Zhongyi Deng, Junlong Cheng, T Li, J Chen, Y Su, Z Huang, Y Shen, et al. Sam-med3d: towards general-purpose segmentation models for volumetric medical images. *arXiv preprint*, 2023.
- [92] Shuo Wang, Chen Qin, Chengyan Wang, Kang Wang, Haoran Wang, Chen Chen, Cheng Ouyang, Xutong Kuang, Chengliang Dai, Yuanhan Mo, Zhang Shi, Chenchen Dai, Xinrong Chen, He Wang, and Wenjia Bai. The extreme cardiac mri analysis challenge under respiratory motion (cmrxmotion), 2022.
- [93] Yueyue Wang, Liang Zhao, Manning Wang, and Zhijian Song. Organ at risk segmentation in head and neck ct images using a two-stage segmentation framework based on 3d u-net. *IEEE Access*, 7:144591–144602, 2019.
- [94] Jakob Wasserthal, Hanns-Christian Breit, Manfred T Meyer, Maurice Pradella, Daniel Hinck, Alexander W Sauter, Tobias Heye, Daniel T Boll, Joshy Cyriac, Shan Yang, et al. Totalsegmentator: Robust segmentation of 104 anatomic structures in ct images. *Radiology: Artificial Intelligence*, 5(5), 2023.
- [95] Chaoyi Wu, Weixiong Lin, Xiaoman Zhang, Ya Zhang, Weidi Xie, and Yanfeng Wang. Pmc-llama: toward building open-source language models for medicine. *Journal of the American Medical Informatics Association*, page ocae045, 2024.
- [96] Chaoyi Wu, Pengcheng Qiu, Jinxin Liu, Hongfei Gu, Na Li, Ya Zhang, Yanfeng Wang, and Weidi Xie. Towards evaluating and building versatile large language models for medicine. *arXiv preprint arXiv:2408.12547*, 2024.

- [97] Chaoyi Wu, Xiaoman Zhang, Ya Zhang, Yanfeng Wang, and Weidi Xie. Medklip: Medical knowledge enhanced language-image pre-training for x-ray diagnosis. In *Proceedings of the IEEE/CVF International Conference on Computer Vision*, pages 21372–21383, October 2023.
- [98] Yutong Xie, Jianpeng Zhang, Chunhua Shen, and Yong Xia. Cotr: Efficiently bridging cnn and transformer for 3d medical image segmentation. In *Medical Image Computing and Computer-Assisted Intervention (MICCAI)*, pages 171–180. Springer, 2021.
- [99] Yunfei Xie, Ce Zhou, Lang Gao, Juncheng Wu, Xianhang Li, Hong-Yu Zhou, Sheng Liu, Lei Xing, James Zou, Cihang Xie, et al. Medtrinity-25m: A large-scale multimodal dataset with multigranular annotations for medicine. *arXiv preprint arXiv:2408.02900*, 2024.
- [100] Ke Yan, Xiaosong Wang, Le Lu, and Ronald M Summers. Deeplesion: automated mining of large-scale lesion annotations and universal lesion detection with deep learning. *Journal of medical imaging*, 5(3):036501–036501, 2018.
- [101] Qihang Yu, Lingxi Xie, Yan Wang, Yuyin Zhou, Elliot K Fishman, and Alan L Yuille. Recurrent saliency transformation network: Incorporating multi-stage visual cues for small organ segmentation. In *Proceedings of the IEEE Conference on Computer Vision and Pattern Recognition*, pages 8280–8289, 2018.
- [102] Sheng Zhang, Yanbo Xu, Naoto Usuyama, Hanwen Xu, Jaspreet Bagga, Robert Tinn, Sam Preston, Rajesh Rao, Mu Wei, Naveen Valluri, et al. A multimodal biomedical foundation model trained from fifteen million image–text pairs. *NEJM AI*, page AIOa2400640, 2024.
- [103] Xiaoman Zhang, Chaoyi Wu, Ya Zhang, Weidi Xie, and Yanfeng Wang. Knowledge-enhanced visual-language pre-training on chest radiology images. *Nature Communications*, 14(1):4542, 2023.
- [104] Xiaoman Zhang, Chaoyi Wu, Ziheng Zhao, Jiayu Lei, Ya Zhang, Yanfeng Wang, and Weidi Xie. Radgenome-chest ct: A grounded vision-language dataset for chest ct analysis. *arXiv preprint arXiv:2404.16754*, 2024.
- [105] Yao Zhang, Nanjun He, Jiawei Yang, Yuexiang Li, Dong Wei, Yawen Huang, Yang Zhang, Zhiqiang He, and Yefeng Zheng. mmformer: Multimodal medical transformer for incomplete multimodal learning of brain tumor segmentation. In *International Conference on Medical Image Computing and Computer-Assisted Intervention (MICCAI)*, pages 107–117. Springer, 2022.
- [106] Yao Zhang, Jiawei Yang, Yang Liu, Jiang Tian, Siyun Wang, Cheng Zhong, Zhongchao Shi, Yang Zhang, and Zhiqiang He. Decoupled pyramid correlation network for liver tumor segmentation from ct images. *Medical Physics*, 49(11):7207–7221, 2022.
- [107] Theodore Zhao, Yu Gu, Jianwei Yang, Naoto Usuyama, Ho Hin Lee, Sid Kiblawi, Tristan Naumann, Jianfeng Gao, Angela Crabtree, Jacob Abel, et al. A foundation model for joint segmentation, detection and recognition of biomedical objects across nine modalities. *Nature Methods*, pages 1–11, 2024.
- [108] Qiaoyu Zheng, Weike Zhao, Chaoyi Wu, Xiaoman Zhang, Lisong Dai, Hengyu Guan, Yuehua Li, Ya Zhang, Yanfeng Wang, and Weidi Xie. Large-scale long-tailed disease diagnosis on radiology images. *Nature Communications*, 15(1):10147, 2024.
- [109] Hong-Yu Zhou, Jiansen Guo, Yinghao Zhang, Xiaoguang Han, Lequan Yu, Liansheng Wang, and Yizhou Yu. nnformer: volumetric medical image segmentation via a 3d transformer. *IEEE Transactions on Image Processing*, 2023.
- [110] Zongwei Zhou, Md Mahfuzur Rahman Siddiquee, Nima Tajbakhsh, and Jianming Liang. Unet++: Redesigning skip connections to exploit multiscale features in image segmentation. *IEEE Transactions on Medical Imaging*, 39(6):1856–1867, 2019.
- [111] Xiahai Zhuang and Juan Shen. Multi-scale patch and multi-modality atlases for whole heart segmentation of mri. *Medical image analysis*, 31:77–87, 2016.

8 Appendix

8.1 More Results in Internal Evaluation

Table 3 | Region-wise results of SAT-Nano, SAT-Pro, SAT-Ft, nnU-Nets, U-Mamba, and SwinUNETR on different human body regions and lesions. H&N: head and neck, LL: lower limb, UL: upper limb, WB: whole body, All: average over all the 497 classes. The best results are **bolded**.

Metric	Method	Brain	H&N	UL	Thorax	Spine	Abdomen	LL	Pelvis	WB	Lesion	All
DSC \uparrow	SAT-Nano	73.90	74.08	89.58	82.09	75.55	77.12	81.79	79.50	77.80	46.04	75.51
	SAT-Pro	77.70	77.29	91.34	86.38	74.73	81.47	84.01	83.01	82.19	51.39	78.81
	SAT-Ft	78.80	78.36	93.78	89.43	82.48	84.11	87.12	86.84	84.24	53.71	81.41
	nnU-Nets	81.93	72.45	89.20	85.60	81.62	86.96	82.89	84.29	84.20	57.52	80.54
	U-Mamba	81.73	70.44	87.54	84.46	78.82	87.65	86.43	85.45	84.74	58.64	79.80
	SwinUNETR	80.76	56.46	86.60	80.34	76.74	84.47	82.56	78.01	83.21	55.65	75.01
NSD \uparrow	SAT-Nano	72.95	79.15	90.94	79.68	73.68	67.83	78.42	74.89	75.36	38.17	73.76
	SAT-Pro	77.77	82.45	93.56	85.15	72.87	72.94	82.50	78.66	79.61	44.87	77.82
	SAT-Ft	80.43	84.01	95.64	86.38	82.37	78.42	87.25	82.92	82.48	47.74	81.60
	nnU-Nets	81.96	74.51	86.04	82.66	77.47	79.54	80.20	76.41	79.30	49.89	78.15
	U-Mamba	82.06	72.19	86.40	81.94	74.45	80.63	82.98	78.02	79.99	50.88	77.59
	SwinUNETR	80.66	56.04	82.11	75.72	71.37	75.03	77.94	66.20	77.65	47.05	71.15

Table 4 | Region-wise results of SAT-Pro, SAT-Nano and MedSAMs on different human body regions and lesion. H&N: head and neck, All: average over all the classes. The best results are bolded. **Note that SAT-Pro and SAT-Nano are fully automatic methods, while MedSAM is interactive.**

Metric	Method	Brain	H&N	Thorax	Spine	Abdomen	Limb	Pelvis	Lesion	All
DSC \uparrow	SAT-Pro	73.23	84.16	85.72	85.52	82.23	82.56	86.35	55.69	82.47
	SAT-Nano	69.05	77.93	79.06	81.88	78.43	77.6	78.31	47.7	76.66
	Oracle Box	55.84	85.32	72.85	78.11	71.92	78.96	81.3	67.94	63.57
	MedSAM (Tight)	54.35	78.48	73.01	79.09	77.35	80.53	84.42	65.85	75.39
	MedSAM (Loose)	14.7	44.68	36.49	45.72	19.79	42.97	51.42	15.71	35.18
	NSD \uparrow	SAT-Pro	80.46	86.12	85.87	87.01	79.98	83.53	82.39	49.35
SAT-Nano		75.62	79.44	77.74	82.7	74.96	77.58	72.98	40.38	74.82
Oracle Box		60.55	86.83	66.16	69.86	59.51	70.67	71.59	61.59	48.93
MedSAM (Tight)		68.62	82.37	68.26	73.29	73.39	73.84	74.9	62.28	70.99
MedSAM (Loose)		10.29	43.57	31.61	43.84	16.81	41.54	46.74	11.46	31.50

Table 5 | Dataset-wise **DSC** scores of SAT-Ft, SAT-Pro, SAT-Nano, nnU-Nets, U-Mamba, SwinUNETR and MedSAMs on 72 datasets in SAT-DS. Datasets uninvolved in training MedSAM are excluded when evaluating MedSAM and marked as /. ‘SwinU’ stands for SwinUNETR, ‘MS-T’ stands for MedSAM Tight (with Oracle Box as prompt) while ‘MS-L’ stands for MedSAM Loose.

Dataset	SAT-Ft	SAT-Pro	SAT-Nano	nnU-Net	U-Mamba	SwinU	MS-T	MS-L
AbdomenCT1K [59]	94.9	94.28	93.32	95.09	95.35	93.73	86.03	10.97
ACDC [9]	89.64	87.74	85.5	90.76	90.83	86.49	/	/
AMOS22 CT [29]	88.75	86.37	84.93	89.77	90.57	87.32	81.21	5.27
AMOS22 MRI [29]	84.82	78.9	78.76	86.43	87.06	84.08	79.17	10.97
ATLAS [75]	76.26	76.02	68.32	78.83	78.33	70.88	/	/
ATLASR2 [46]	61.77	61.44	53.95	53.69	68.94	65.0	61.19	3.96
autoPET [16]	71.66	68.56	62.27	74.98	74.48	71.46	/	/
Brain Atlas [85]	79.71	78.57	74.89	83.78	83.81	83.56	/	/
BrainPTM [5]	65.33	66.8	64.42	68.37	67.74	66.31	/	/
BraTS2023 GLI [62]	68.18	67.92	65.05	73.22	73.87	71.67	64.49	14.28
BraTS2023 MEN [36]	63.89	58.04	52.75	64.4	70.47	66.41	77.03	35.96
BraTS2023 MET [64]	44.22	43.76	40.6	47.54	51.95	48.28	49.98	15.5
BraTS2023 PED [32]	59.74	51.83	49.02	57.48	61.56	55.55	72.04	24.83
BraTS2023 SSA [2]	55.68	55.73	53.19	59.02	57.15	52.6	65.61	20.12
BTCV [38]	81.6	80.71	79.6	77.66	74.88	71.82	/	/
BTCV Cervix [38]	74.86	73.73	72.99	71.57	78.7	75.0	/	/
CHAOS CT [31]	97.24	97.02	96.54	97.08	97.34	96.88	/	/
CHAOS MRI [31]	87.99	87.28	82.07	88.8	87.27	80.84	/	/
CMRxMotion [92]	90.28	88.19	87.45	91.14	91.94	88.06	/	/
Couinaud Liver [87]	85.54	81.23	72.01	87.86	87.8	86.16	/	/
COVID19 [57]	87.09	83.18	71.51	91.53	91.78	88.58	61.45	58.22
CrossMoDA2021 [14]	79.15	78.34	73.16	81.77	83.94	82.45	90.41	0.87
CT ORG [79]	92.21	90.12	85.44	75.27	76.05	71.43	74.24	31.87
CTPelvic1K [49]	96.58	95.86	95.14	76.43	77.26	77.81	/	/
DAP Atlas [28]	85.79	85.79	84.39	87.73	88.33	80.81	/	/
FeTA2022 [69]	76.24	73.23	69.05	75.83	75.39	75.05	54.35	14.7
FLARE22 [58]	91.78	91.12	88.79	93.36	93.46	90.91	/	/
FUMPE [61]	22.94	22.04	36.13	47.65	34.19	35.74	/	/
HAN Seg [71]	73.15	72.11	69.73	62.18	61.23	54.59	/	/
Hecktor2022 [3]	61.99	58.3	55.75	64.52	65.68	62.29	/	/
Instance22 [45]	67.84	70.18	55.7	81.53	80.43	71.9	71.22	3.85
ISLES2022 [24]	53.7	55.12	43.64	64.95	64.59	63.77	54.74	9.61
KiPA22 [21]	76.59	74.87	64.39	90.34	90.5	89.61	60.9	20.0
KiTS23 [23]	71.53	67.98	55.96	74.69	74.33	68.86	67.93	18.54
LAScarQS22 Task1 [43]	66.83	68.97	66.45	71.47	70.25	69.09	/	/
LAScarQS22 Task2 [43]	92.36	92.03	90.0	85.28	92.73	91.59	/	/
LNDb [70]	36.2	37.08	28.0	24.45	/	23.91	/	/
LUNA16 [86]	97.16	96.32	95.97	96.64	96.88	95.94	/	/
MM WHS CT [111]	91.14	89.97	88.23	88.64	91.56	91.25	/	/
MM WHS MRI [111]	87.73	86.7	84.37	30.88	21.20	20.87	/	/
MRSpineSeg [68]	79.78	71.97	74.06	68.97	67.96	66.3	/	/

Table 6 | (Continued) Dataset-wise **DSC** scores of SAT-Ft, SAT-Pro, SAT-Nano, nnU-Nets, U-Mamba, SwinUNETR and MedSAMs on 72 datasets in SAT-DS. Datasets uninvolved in training MedSAM are excluded when evaluating MedSAM and marked as /. ‘SwinU’ stands for SwinUNETR, ‘MS-T’ stands for MedSAM Tight (with Oracle Box as prompt) while ‘MS-L’ stands for MedSAM Loose. ‘TS’ stands for TotalSegmentator.

Dataset	SAT-Ft	SAT-Pro	SAT-Nano	nnU-Net	U-Mamba	SwinUNETR	MS-T	MS-L
MSD Cardiac [4]	93.38	92.61	90.28	94.28	93.8	93.46	83.6	3.11
MSD Colon [4]	38.45	35.29	23.43	54.39	54.25	41.4	71.02	2.59
MSD HepaticVessel [4]	63.43	63.14	53.56	67.74	68.73	66.07	/	/
MSD Hippocampus [4]	87.62	87.62	86.25	89.18	89.03	89.03	/	/
MSD Liver [4]	78.86	76.63	68.16	77.92	77.99	75.46	/	/
MSD Lung [4]	61.28	62.65	51.01	71.74	66.07	64.59	68.43	1.23
MSD Pancreas [4]	59.23	59.32	58.2	68.64	69.7	57.87	69.96	2.84
MSD Prostate [4]	77.98	78.33	73.38	71.32	77.72	67.73	74.09	69.18
MSD Spleen [4]	94.97	94.12	93.5	92.95	86.11	84.83	93.33	81.14
MyoPS2020 [72]	61.06	58.69	59.77	14.85	12.41	11.94	/	/
NSCLC [8]	77.97	77.51	75.48	78.58	78.83	78.56	77.51	49.94
Pancreas CT [82]	84.69	85.57	84.35	87.52	87.6	86.89	/	/
PARSE2022 [52]	79.41	74.9	71.04	85.85	85.77	85.03	/	/
PDDCA [78]	73.75	76.68	72.83	57.45	53.07	51.65	/	/
PROMISE12 [48]	87.28	86.51	84.55	88.86	89.53	87.46	85.51	8.67
SEGA [77]	89.59	83.9	81.48	89.43	89.95	87.23	/	/
SegRap2023 Task1 [53]	86.46	84.86	82.8	79.98	76.78	57.32	/	/
SegRap2023 Task2 [53]	72.01	70.9	65.98	74.48	74.69	71.09	/	/
SegTHOR [37]	88.98	86.69	82.6	91.32	91.37	89.92	74.9	5.37
SKI10 [40]	84.7	83.36	80.51	88.15	88.27	87.23	/	/
SLIVER07 [22]	97.63	97.43	97.03	97.3	96.77	93.56	/	/
ToothFairy [13]	78.17	77.95	63.65	83.08	83.28	79.85	/	/
TS Cardiac [94]	92.52	88.96	76.77	93.3	93.73	91.23	81.26	36.35
TS Muscles [94]	93.33	88.04	82.17	91.6	92.0	90.21	82.23	43.74
TS Organs [94]	90.42	87.53	83.4	93.22	93.23	90.41	82.71	35.52
TS Ribs [94]	91.53	83.73	75.78	92.1	90.85	88.51	68.85	30.54
TS v2 [94]	86.71	78.46	72.48	92.39	91.53	88.85	80.11	65.89
TS Vertebrae [94]	90.42	85.21	81.92	95.37	95.68	94.08	79.13	44.83
VerSe [84]	81.01	61.55	61.18	81.82	69.13	70.17	/	/
WMH [35]	69.22	69.05	62.55	77.02	77.77	75.22	/	/
WORD [54]	87.92	86.77	86.57	85.49	87.75	85.27	/	/

Table 7 | Dataset-wise NSD scores of SAT-Ft, SAT-Pro, SAT-Nano, nnU-Nets, U-Mamba, SwinUNETR and MedSAMs on 72 datasets in SAT-DS. Datasets uninvolved in training MedSAM are excluded when evaluating MedSAM and marked as /. ‘SwinU’ stands for SwinUNETR, ‘MS-T’ stands for MedSAM Tight (with Oracle Box as prompt) while ‘MS-L’ stands for MedSAM Loose.

Dataset	SAT-Ft	SAT-Pro	SAT-Nano	nnU-Net	U-Mamba	SwinU	MS-T	MS-L
AbdomenCT1K [59]	89.53	87.3	84.41	88.24	88.7	85.38	72.85	2.37
ACDC [9]	78.79	72.47	66.77	97.62	80.89	73.92	/	/
AMOS22 CT [29]	87.66	82.98	80.21	87.11	88.44	82.52	75.72	2.25
AMOS22 MRI [29]	83.39	75.22	74.01	79.56	80.59	75.07	74.32	7.71
ATLAS [75]	48.93	46.99	40.21	45.19	45.99	35.88	/	/
ATLASR2 [46]	62.14	61.24	51.57	48.93	69.06	63.26	66.74	1.11
autoPET [16]	60.47	56.3	48.17	57.94	58.58	55.37	/	/
Brain Atlas [85]	81.28	78.48	73.34	85.35	85.66	85.11	/	/
BrainPTM [5]	54.62	54.02	50.68	33.9	34.08	32.5	/	/
BraTS2023 GLI [62]	63.79	62.27	58.26	68.25	69.3	66.55	62.66	4.83
BraTS2023 MEN [36]	60.84	54.55	47.95	61.57	67.09	61.53	76.31	31.25
BraTS2023 MET [64]	42.18	41.62	37.22	45.95	50.21	45.63	57.26	11.78
BraTS2023 PED [32]	54.09	45.94	42.89	51.38	55.86	48.81	70.69	19.75
BraTS2023 SSA [2]	45.96	46.35	42.94	46.73	45.09	41.16	59.84	9.26
BTCV [38]	79.52	77.19	76.22	74.85	54.5	50.12	/	/
BTCV Cervix [38]	51.85	50.93	49.21	48.31	76.26	69.28	/	/
CHAOS CT [31]	85.88	84.63	81.12	81.04	81.33	79.71	/	/
CHAOS MRI [31]	59.78	53.4	47.39	64.35	64.02	52.99	/	/
CMRxMotion [92]	80.54	73.09	70.39	86.47	87.88	80.66	/	/
Couinaud Liver [87]	64.95	53.05	42.72	70.44	70.58	66.72	/	/
COVID19 [57]	78.44	72.83	48.68	77.02	80.23	73.61	27.03	19.29
CrossMoDA2021 [14]	96.24	95.69	93.06	93.16	96.57	95.24	96.49	1.38
CT ORG [79]	82.5	77.57	72.0	66.15	67.32	61.97	57.13	20.85
CTPelvic1K [49]	98.48	97.57	96.28	73.45	79.43	73.42	/	/
DAP Atlas [28]	86.51	86.51	85.49	87.35	88.3	76.86	/	/
FeTA2022 [69]	84.31	80.46	75.62	81.34	81.01	80.19	68.62	10.29
FLARE22 [58]	90.88	89.47	85.76	91.15	91.44	87.0	/	/
FUMPE [61]	21.7	18.07	32.15	42.02	28.31	29.32	/	/
HAN Seg [71]	79.93	77.76	74.29	63.52	62.04	53.43	/	/
Hecktor2022 [3]	49.97	45.49	43.21	43.84	45.59	40.88	/	/
Instance22 [45]	64.65	66.74	45.25	79.73	78.76	66.88	70.73	1.95
ISLES2022 [24]	53.53	54.67	42.15	60.1	59.88	58.85	58.6	5.66
KiPA22 [21]	77.58	74.83	61.68	89.54	90.29	87.73	61.4	10.16
KiTS23 [23]	65.81	59.8	47.06	70.14	70.04	62.64	51.16	15.49
LAScarQS22 Task1 [43]	78.3	80.45	75.39	77.06	76.95	73.2	/	/
LAScarQS22 Task2 [43]	81.08	80.23	72.58	64.02	78.81	74.24	/	/
LNDb [70]	43.21	45.52	31.24	29.38	/	27.36	/	/
LUNA16 [86]	96.79	94.12	92.42	93.85	94.44	90.03	/	/
MM WHS CT [111]	79.62	75.61	70.1	64.45	73.79	72.95	/	/
MM WHS MRI [111]	72.42	69.32	64.67	23.92	7.74	7.43	/	/
MRSpineSeg [68]	78.25	67.01	68.62	58.82	57.59	56.02	/	/

Table 8 | (Continued) Dataset-wise **NSD** scores of SAT-Ft, SAT-Pro, SAT-Nano, nnU-Nets, U-Mamba, SwinUNETR and MedSAMs on 72 datasets in SAT-DS. Datasets uninvolved in training MedSAM are excluded when evaluating MedSAM and marked as /. ‘SwinU’ stands for SwinUNETR, ‘MS-T’ stands for MedSAM Tight (with Oracle Box as prompt) while ‘MS-L’ stands for MedSAM Loose. ‘TS’ stands for TotalSegmentator.

Dataset	SAT-Ft	SAT-Pro	SAT-Nano	nnU-Net	U-Mamba	SwinUNETR	MS-T	MS-L
MSD Cardiac [4]	85.93	83.14	77.29	64.21	62.63	61.68	60.84	1.49
MSD Colon [4]	34.21	29.79	15.7	51.07	50.42	36.31	63.65	1.52
MSD HepaticVessel [4]	56.89	56.07	46.49	61.85	63.15	59.18	/	/
MSD Hippocampus [4]	96.46	96.46	95.64	97.92	97.7	97.7	/	/
MSD Liver [4]	67.19	62.89	52.66	63.78	63.27	57.17	/	/
MSD Lung [4]	53.59	52.42	38.62	58.32	54.8	50.9	59.58	0.73
MSD Pancreas [4]	46.57	46.84	45.25	53.31	54.77	42.31	52.36	0.96
MSD Prostate [4]	56.09	56.41	49.53	51.1	53.27	37.5	55.07	42.53
MSD Spleen [4]	88.75	84.85	80.46	88.01	84.44	81.11	81.13	45.67
MyoPS2020 [72]	44.08	40.07	40.74	14.05	9.81	9.57	/	/
NSCLC [8]	63.8	62.54	58.51	65.07	65.94	63.9	62.54	25.45
Pancreas CT [82]	76.41	76.25	74.06	78.19	78.91	76.83	/	/
PARSE2022 [52]	80.45	72.94	64.53	90.46	90.53	88.79	/	/
PDDCA [78]	77.65	79.16	74.48	52.98	48.47	46.06	/	/
PROMISE12 [48]	68.92	64.78	57.73	71.9	73.79	65.93	64.89	2.04
SEGA [77]	86.93	74.49	69.4	81.44	82.36	76.82	/	/
SegRap2023 Task1 [53]	91.69	89.25	86.51	80.64	77.32	55.21	/	/
SegRap2023 Task2 [53]	53.43	51.39	44.91	51.3	51.65	46.49	/	/
SegTHOR [37]	80.22	75.36	69.72	82.93	83.47	80.31	54.82	0.85
SKI10 [40]	93.35	91.56	88.06	94.38	94.55	92.16	/	/
SLIVER07 [22]	86.36	86.91	83.4	85.62	85.47	77.38	/	/
ToothFairy [13]	84.02	83.55	67.61	89.31	89.55	85.6	/	/
TotalSegmentator Cardiac [94]	91.94	86.69	72.9	84.83	85.75	80.88	71.71	34.6
TotalSegmentator Muscles [94]	93.65	87.21	79.99	84.53	85.49	81.33	71.04	41.42
TotalSegmentator Organs [94]	88.45	83.97	78.49	86.06	86.3	80.83	71.08	30.52
TotalSegmentator Ribs [94]	94.7	88.66	80.43	91.95	90.68	87.8	76.95	30.55
TotalSegmentator v2 [94]	88.43	79.38	72.98	89.21	87.56	83.51	80.5	59.64
TotalSegmentator Vertebrae [94]	91.84	86.7	82.76	94.7	95.04	92.22	73.41	43.74
VerSe [84]	81.46	60.32	59.34	82.89	70.03	70.59	/	/
WMH Segmentation Challenge [35]	84.53	84.12	76.58	88.88	88.75	86.3	/	/
WORD [54]	81.19	77.56	76.83	78.79	81.3	76.32	/	/

Table 9 | Class-wise **DSC** results of SAT-Ft, SAT-Pro, SAT-Nano, nnU-Nets, U-Mamba and SwinUNETR on common anatomical structures in abdomen, brain, head and neck, and spine.

Region	Modality	Anatomical Target	SAT-Ft	SAT-Pro	SAT-Nano	nnU-Nets	U-Mamba	SwinUNETR
Abdomen	CT	Adrenal gland	82.21	81.54	79.24	84.43	84.76	80.15
	CT	Celiac trunk	87.56	87.56	84.55	86.86	87.57	73.19
	CT	Duodenum	82.55	80.77	79.23	84.38	85.28	78.4
	CT	Gallbladder	81.14	80.37	78.96	83.98	84.96	78.74
	CT	Inferior vena cava	91.91	90.94	89.93	92.24	92.86	89.48
	CT	Intestine	88.78	86.6	86.03	89.41	89.9	87.83
	CT	Kidney	94.03	93.23	91.21	91.69	92.43	90.42
	CT	Liver	96.49	96.21	95.12	94.41	94.48	93.4
	CT	Pancreas	86.79	86.09	85.21	85.08	88.61	84.14
	CT	Small bowel	79.06	76.43	75.52	78.15	79.98	75.46
	CT	Spleen	95.45	94.88	92.54	93.85	93.28	91.39
	CT	Stomach	80.39	76.04	72.01	91.61	92.05	88.21
	MRI	Adrenal gland	66.47	64.16	76.81	69.61	67.92	66.59
	MRI	Kidney	92.47	91.79	69.11	94.28	93.72	88.8
	MRI	Liver	94.31	92.9	44.14	92.98	92.81	91.31
	MRI	Pancreas	86.23	84.2	86.67	89.19	89.41	84.23
	MRI	Spleen	88.94	88.12	81.99	90.45	88.43	83.97
	Brain	CT	Brainstem	84.01	86.29	85.4	88.3	88.96
CT		Hippocampus	78.45	77.96	77.11	65.43	63.1	52.47
CT		Temporal lobe	94.93	93.74	92.71	87.96	84.5	73.34
MRI		Brain ventricle	82.12	80.62	79.76	77.24	76.78	76.95
MRI		Cerebellum	92.24	90.94	64.69	93.23	93.18	92.84
MRI		Parietal lobe	78.12	77.26	78.55	83.62	83.43	83.25
MRI		Optic radiation	61.78	63.52	75.49	65.04	64.22	62.85
MRI		Thalamus	87.96	87.4	80.8	91.09	91.05	90.55
Head and neck	CT	Brain	98.61	98.03	94.78	94.94	97.31	91.04
	CT	Carotid artery	79.8	77.35	72.37	73.51	74.4	64.15
	CT	Cervical esophagus	65.94	67.31	60.06	62.0	62.95	58.76
	CT	Cheek	40.71	40.71	43.16	53.56	48.03	49.47
	CT	Cochlea	71.74	70.34	69.48	67.49	61.03	8.7
	CT	Eustachian tube bone	81.23	80.13	76.22	75.86	70.3	37.84
	CT	Eyeball	86.45	85.15	82.64	54.49	52.42	43.4
	CT	Lacrimal gland	48.12	49.52	48.55	35.26	27.88	31.49
	CT	Lens	77.73	76.97	75.25	75.67	68.38	0.0
	CT	Mandible	94.48	93.31	92.68	73.93	75.24	64.85
	CT	Middle ear	86.76	84.5	81.36	76.7	70.15	46.45
	CT	Optic nerve	71.13	71.71	59.15	57.67	51.09	53.73
	CT	Parotid gland	84.85	85.24	84.51	60.89	60.9	58.73
	CT	Submandibular gland	78.61	80.36	79.68	63.49	63.58	56.66
	CT	Thyroid gland	82.54	81.83	45.02	85.29	84.58	80.87
CT	Tympanic cavity	82.29	78.83	81.43	74.37	69.95	40.57	
MRI	Brain	95.41	94.59	46.42	95.11	95.12	95.3	
Spine	CT	Lumbar vertebrae	80.99	75.85	74.56	88.41	85.92	84.57
	CT	Sacrum	94.15	92.35	89.22	96.63	97.06	93.85
	CT	Spinal canal	94.6	94.6	93.4	95.87	95.99	93.95
	CT	Spinal cord	86.37	83.71	83.14	87.6	87.98	86.31
	CT	Thoracic vertebrae	87.32	79.33	79.18	90.04	85.81	81.72
	MRI	Intervertebral discs	89.17	87.3	90.49	74.72	74.89	74.85
	MRI	Lumbar vertebrae	83.25	79.74	67.96	69.59	69.85	66.48
	MRI	Sacrum	86.47	79.64	80.81	67.31	67.21	66.19
	MRI	Thoracic vertebrae	70.19	53.75	64.37	60.97	56.73	60.63

Table 10 | (Continued) Class-wise **DSC** results of SAT-Ft, SAT-Pro, SAT-Nano, nnU-Nets, U-Mamba and SwinUNETR on common anatomical structures in thorax, limbs, pelvis, whole body and common lesions.

Region	Modality	Anatomical Target	SAT-Ft	SAT-Pro	SAT-Nano	nnU-Nets	U-Mamba	SwinUNETR
Thorax	CT	Autochthon	96.24	95.71	93.82	94.11	93.47	91.97
	CT	Breast	61.82	61.82	58.17	58.45	60.63	42.23
	CT	Heart atrium	92.91	91.17	89.33	92.56	93.7	92.32
	MRI	Heart ventricle	94.01	92.2	88.97	93.72	94.88	92.97
	CT	Lung	94.88	93.65	90.44	95.57	95.38	92.74
	CT	Rib	89.65	85.62	80.47	88.38	89.62	84.95
	CT	Myocardium	92.75	88.8	83.66	92.92	94.33	91.4
	CT	Thoracic cavity	95.97	95.36	94.62	95.56	95.55	95.53
	CT	Thymus	68.15	68.15	70.22	67.47	71.09	45.8
Upper limb	CT	Clavicle	94.55	91.63	90.93	95.0	95.23	93.57
	CT	Humerus	91.47	88.92	87.06	79.67	75.61	76.39
	CT	Scapula	95.27	94.21	91.56	92.92	91.79	89.83
Lower limb	CT	Head of femur	92.44	90.1	91.77	92.78	92.75	92.47
	MRI	Femur bone	96.93	96.33	66.7	98.25	98.27	97.66
	MRI	Femur cartilage	73.77	71.52	90.51	78.87	79.43	77.84
	MRI	Tibia bone	97.63	97.11	63.94	98.19	98.2	97.37
	MRI	Tibia cartilage	70.48	68.5	55.66	77.3	77.18	76.04
Pelvis	CT	Gluteus maximus	96.88	96.37	91.74	82.96	84.12	77.2
	CT	Gluteus medius	95.37	93.33	84.01	89.87	90.42	83.76
	CT	Gluteus minimus	92.51	90.59	92.91	90.35	90.88	82.27
	CT	Hip	94.84	93.29	92.91	82.97	83.85	79.49
	CT	Iliopsoas	94.58	91.19	90.14	93.09	93.04	89.09
	CT	Iliac vena	90.74	89.96	75.48	92.0	93.06	82.72
	CT	Urinary bladder	90.76	89.19	52.89	88.24	89.4	85.59
	CT	Uterocervix	68.95	68.95	51.28	80.85	83.51	65.46
	CT	Uterus	51.64	51.28	89.94	62.2	65.94	50.93
MRI	Prostate	77.97	78.18	77.76	77.17	78.07	68.79	
Whole body	CT	Bone	86.81	79.41	64.72	70.06	70.29	70.13
	CT	Fat	96.43	96.43	95.81	98.66	98.65	97.97
	CT	Muscle	95.84	95.84	95.17	98.1	98.2	97.0
	CT	Skin	87.41	87.41	84.76	95.49	95.39	94.75
	PET	Lymph node	56.76	51.87	62.27	58.68	61.16	56.18
Lesions	CT	Liver tumor	63.3	61.47	45.64	66.0	66.85	62.53
	CT	Lung nodule	36.2	37.08	28.0	24.45	0.0	23.91
	MRI	Brain tumor	58.34	55.46	75.63	60.33	63.0	58.9
	MRI	Myocardial edema	9.23	7.5	19.67	5.37	0.3	0.53
	MRI	Stroke	57.73	58.28	86.84	59.32	66.76	64.39
	PET	Head and neck tumor	67.23	64.72	50.15	70.35	70.19	68.39
	PET	Tumor	71.66	68.56	75.51	74.98	74.48	71.46

Table 11 | Class-wise **NSD** results of SAT-Ft, SAT-Pro, SAT-Nano, nnU-Nets, U-Mamba and SwinUNETR on common anatomical structures in abdomen, brain, head and neck, and spine.

Region	Modality	Anatomical Target	SAT-Ft	SAT-Pro	SAT-Nano	nnU-Nets	U-Mamba	SwinUNETR
Abdomen	CT	Adrenal gland	90.71	90.26	87.83	89.41	89.67	84.17
	CT	Celiac trunk	94.35	94.35	92.7	91.7	92.34	77.82
	CT	Duodenum	77.94	73.62	71.01	77.1	78.91	67.05
	CT	Gallbladder	79.09	77.31	74.73	78.25	81.58	70.8
	CT	Inferior vena cava	90.49	88.77	86.6	87.22	88.24	80.82
	CT	Intestine	80.73	73.51	72.01	81.87	83.34	78.82
	CT	Kidney	92.21	90.28	86.64	88.67	89.56	85.55
	CT	Liver	86.16	84.4	80.99	83.52	84.04	79.75
	CT	Pancreas	78.88	77.55	75.4	74.55	78.79	70.6
	CT	Small bowel	67.32	64.16	61.63	64.8	67.05	58.31
	CT	Spleen	91.96	89.89	86.61	90.47	90.53	86.9
	CT	Stomach	69.09	62.3	56.92	81.04	82.2	72.24
	MRI	Adrenal gland	79.94	76.5	86.54	71.65	70.1	68.28
	MRI	Kidney	78.06	74.17	70.51	78.98	78.84	69.6
	MRI	Liver	70.82	64.37	19.29	68.99	70.12	63.93
	MRI	Pancreas	77.66	72.39	59.8	74.8	75.61	66.92
	MRI	Spleen	71.72	67.22	55.29	75.3	74.96	67.83
	Brain	CT	Brainstem	74.8	73.24	70.3	71.24	73.48
CT		Hippocampus	79.88	78.57	77.24	63.94	62.05	50.96
CT		Temporal lobe	86.46	81.75	77.66	72.15	68.89	54.36
MRI		Brain ventricle	91.58	89.72	82.57	86.26	85.64	85.99
MRI		Cerebellum	90.15	86.0	52.41	93.17	93.04	91.71
MRI		Parietal lobe	64.02	59.57	73.91	72.0	72.38	71.8
MRI		Optic radiation	56.94	56.61	78.4	35.42	35.09	33.84
MRI		Thalamus	90.39	88.97	74.21	93.5	93.39	92.05
Head and neck	CT	Brain	95.88	91.65	88.28	91.68	94.35	86.8
	CT	Carotid artery	91.62	86.27	82.79	81.32	80.27	70.54
	CT	Cervical esophagus	68.43	69.79	61.1	57.53	59.85	57.76
	CT	Cheek	34.49	34.49	38.3	51.12	50.84	44.24
	CT	Cochlea	92.01	91.75	89.93	82.81	73.37	10.98
	CT	Eustachian tube bone	97.01	96.48	94.07	89.23	82.87	48.46
	CT	Eyeball	90.55	88.73	84.02	53.21	51.17	41.7
	CT	Lacrimal gland	68.17	67.06	66.5	43.7	36.77	38.42
	CT	Lens	93.68	93.76	92.53	87.22	79.04	0.0
	CT	Mandible	96.97	95.17	94.38	71.69	73.54	62.26
	CT	Middle ear	93.48	91.93	87.74	85.27	78.23	55.71
	CT	Optic nerve	89.16	89.46	75.78	67.4	59.48	62.63
	CT	Parotid gland	76.82	75.09	73.31	48.79	48.52	44.19
	CT	Submandibular gland	77.39	78.08	76.03	55.14	55.01	47.59
	CT	Thyroid gland	84.79	83.83	44.07	84.65	83.36	77.05
CT	Tympanic cavity	95.31	94.05	85.79	85.61	80.73	48.73	
MRI	Brain	60.14	53.91	42.3	37.75	38.07	38.57	
Spine	CT	Lumbar vertebrae	80.5	74.3	73.34	88.57	86.09	82.77
	CT	Sacrum	93.95	91.94	89.89	96.05	96.55	91.43
	CT	Spinal canal	97.37	97.37	96.09	96.6	97.06	94.07
	CT	Spinal cord	91.54	87.42	86.1	85.36	85.53	83.06
	CT	Thoracic vertebrae	88.46	79.88	79.3	90.35	86.14	79.43
	MRI	Intervertebral discs	92.07	89.29	71.06	63.3	63.56	63.23
	MRI	Lumbar vertebrae	77.06	66.87	57.41	54.02	54.17	50.94
	MRI	Sacrum	83.41	68.22	60.42	55.61	55.53	53.42
	MRI	Thoracic vertebrae	66.97	46.31	58.55	54.57	49.44	53.75

Table 12 | (Continued) Class-wise **NSD** results of SAT-Ft, SAT-Pro, SAT-Nano, nnU-Nets, U-Mamba and SwinUNETR on common anatomical structures in thorax, limbs, pelvis, whole body and common lesions.

Region	Modality	Anatomical Target	SAT-Ft	SAT-Pro	SAT-Nano	nnU-Nets	U-Mamba	SwinUNETR
Thorax	CT	Autochthon	96.65	95.02	91.36	84.73	84.8	77.24
	CT	Breast	61.33	61.33	56.36	53.85	57.3	31.32
	CT	Heart atrium	84.91	82.05	78.34	74.65	78.96	72.99
	MRI	Heart ventricle	87.07	81.78	75.05	77.99	82.09	74.79
	CT	Lung	88.74	85.66	77.8	89.71	89.69	80.8
	CT	Rib	93.0	89.86	84.98	89.48	90.41	85.12
	CT	Myocardium	90.69	83.63	75.39	83.84	87.99	81.16
	CT	Thoracic cavity	76.03	73.15	70.54	76.71	77.25	75.65
	CT	Thymus	73.72	73.72	75.26	70.75	73.81	47.63
Upper limb	CT	Clavicle	96.45	93.6	92.78	93.76	94.26	90.62
	CT	Humerus	92.27	89.53	86.39	72.27	73.55	68.15
	CT	Scapula	98.2	97.58	94.87	92.08	91.39	87.58
Lower limb	CT	Head of femur	85.43	78.75	81.25	84.97	85.59	83.82
	MRI	Femur bone	93.1	91.0	86.39	96.8	96.94	93.54
	MRI	Femur cartilage	91.85	89.84	68.17	91.39	91.69	90.86
	MRI	Tibia bone	96.71	95.16	86.98	97.11	97.38	92.81
	MRI	Tibia cartilage	91.75	90.23	49.93	92.21	92.19	91.43
Pelvis	CT	Gluteus maximus	94.85	93.56	88.25	71.35	71.42	62.41
	CT	Gluteus medius	94.19	90.88	79.62	78.54	80.63	67.04
	CT	Gluteus minimus	91.46	88.44	92.29	85.3	86.29	71.04
	CT	Hip	93.51	91.75	93.55	79.3	83.31	71.94
	CT	Iliopsoas	96.16	91.82	90.19	87.24	87.67	77.81
	CT	Iliac vena	91.59	90.71	76.73	90.58	92.06	77.97
	CT	Urinary bladder	77.21	73.49	51.04	73.56	76.47	68.6
	CT	Uterocervix	67.93	67.93	35.46	78.34	81.56	62.6
	CT	Uterus	36.37	36.29	89.04	45.86	51.5	34.21
MRI	Prostate	58.17	57.58	75.96	58.03	56.6	42.13	
Whole body	CT	Bone	80.27	69.8	54.22	61.78	62.19	61.44
	CT	Fat	96.35	96.35	94.91	98.54	98.65	96.95
	CT	Muscle	93.96	93.96	92.1	97.94	98.13	94.83
	CT	Skin	99.3	99.3	98.56	99.7	99.75	99.53
	PET	Lymph node	44.18	38.66	48.17	38.53	41.23	35.48
Lesions	CT	Liver tumor	47.33	43.83	28.09	50.26	50.98	43.22
	CT	Lung nodule	43.21	45.52	31.24	29.38	0.0	27.36
	MRI	Brain tumor	53.37	50.14	68.96	54.78	57.51	52.74
	MRI	Myocardial edema	15.01	13.34	16.94	9.02	0.85	1.86
	MRI	Stroke	57.83	57.95	67.56	54.52	64.47	61.06
	PET	Head and neck tumor	55.76	52.33	37.01	49.16	49.95	46.29
	PET	Tumor	60.47	56.3	73.76	57.94	58.58	55.37

Table 13 | Class-wise results of SAT-Pro, SAT-Nano and MedSAMs on common anatomical structures and lesions. ‘MS-T’ stands for MedSAM (Tight) while ‘MS-L’ stands for MedSAM (Loose).

Region	Modality	Anatomical Target	DSC \uparrow				NSD \uparrow			
			SAT-Pro	SAT-Nano	MS-T	MS-L	SAT-Pro	SAT-Nano	MS-T	MS-L
Abdomen	CT	Adrenal gland	80.98	78.37	66.8	68.99	89.82	86.78	77.2	71.56
	CT	Duodenum	78.3	77.39	69.33	65.04	71.67	69.59	61.6	55.76
	CT	Gallbladder	80.89	78.69	87.66	82.76	78.07	74.24	83.82	73.54
	CT	Kidney	93.6	90.17	89.1	78.46	90.57	85.68	81.01	53.16
	CT	Liver	94.9	93.07	95.28	76.26	82.4	78.03	77.75	38.13
	CT	Pancreas	86.03	85.06	77.1	60.02	76.96	74.58	61.52	43.42
	CT	Small bowel	80.15	79.82	73.92	67.25	73.3	71.51	61.74	49.34
	CT	Spleen	94.43	91.29	94.44	74.52	89.86	84.73	86.34	45.21
	CT	Stomach	88.53	80.01	89.62	77.77	77.42	65.9	70.96	48.54
	MRI	Adrenal gland	64.16	62.59	58.02	64.4	76.5	73.96	75.12	71.26
	MRI	Kidney	94.57	94.37	93.7	83.4	89.1	88.08	85.35	50.36
	MRI	Liver	96.29	96.1	92.66	71.38	81.88	80.95	66.25	27.24
	MRI	Pancreas	84.2	79.23	76.47	57.0	72.39	66.29	60.74	38.91
	MRI	Spleen	95.19	94.96	91.95	73.73	89.45	88.28	76.35	41.49
MRI	Stomach	85.46	81.99	80.2	73.51	64.78	55.29	50.88	42.84	
Thorax	CT	Autochthon	94.15	90.94	74.65	86.41	91.87	85.89	45.47	62.68
	CT	Heart	88.82	76.4	87.08	83.15	63.88	52.76	47.98	44.62
	CT	Heart atrium	89.47	84.95	85.52	87.74	82.97	76.11	63.76	68.37
	CT	Heart ventricle	91.12	84.84	85.21	83.28	82.26	73.53	59.62	61.88
	CT	Lung	90.59	84.91	77.48	73.8	81.72	69.25	43.71	37.35
	CT	Rib	83.58	75.17	71.8	71.46	88.44	79.73	80.33	76.82
Head and neck	CT	Brain	98.19	91.77	99.08	98.23	96.57	89.89	96.61	93.55
	CT	Esophagus	84.45	82.26	74.38	82.69	85.31	82.27	74.15	81.94
	CT	Trachea	90.1	87.62	76.84	80.21	90.39	87.41	70.82	73.03
	MRI	Esophagus	74.21	71.29	68.24	85.56	75.48	72.15	76.24	93.64
Spine	CT	Lumbar vertebrae	81.86	78.87	80.15	76.72	82.7	79.03	69.99	64.47
	CT	Sacrum	91.77	77.8	84.38	81.4	91.62	77.05	72.73	66.83
	CT	Thoracic vertebrae	86.58	82.79	74.58	73.4	88.29	83.76	67.98	63.45
Limb	CT	Clavicle	86.51	86.7	85.89	83.25	88.35	88.07	83.49	77.31
	CT	Humerus	81.56	79.67	84.69	86.66	82.53	79.56	77.06	78.63
Lesions	CT	Colon cancer	35.29	23.43	71.02	72.3	29.79	15.7	63.65	56.2
	CT	Kidney tumor	63.33	38.81	78.19	86.34	47.08	22.8	58.51	72.86
	CT	Lung tumor	62.65	51.01	68.43	76.3	52.42	38.62	59.58	68.91
	MRI	Brain tumor	55.46	52.12	65.83	66.43	50.14	45.85	65.35	61.15
Pelvis	CT	Gluteus maximus	95.81	86.54	92.97	79.92	92.31	81.65	78.99	64.38
	CT	Gluteus medius	89.62	72.1	87.68	77.24	85.4	65.57	71.81	63.46
	CT	Gluteus minimus	91.22	91.03	81.41	77.61	89.67	87.74	73.63	67.77
	CT	Hip	91.21	85.58	76.86	67.9	91.24	85.17	65.5	58.5
	CT	Prostate	70.4	63.86	92.93	96.6	66.5	59.1	87.84	93.66
	CT	Urinary bladder	85.02	81.57	90.09	85.97	68.5	63.53	74.12	63.52
	MRI	Prostate	78.18	73.28	74.17	80.47	57.58	50.58	56.64	66.36
Brain	MRI	Brainstem	69.18	67.27	73.48	78.55	76.18	73.86	85.35	88.42
	MRI	Cerebellum	74.42	67.47	74.53	75.25	78.04	69.38	79.27	76.01

Table 14 | Detailed comparison of SAT-Pro, SAT-Nano and BiomedParses on each dataset and each category. ‘BP’ denotes BiomedParse. Subregions of anatomical structures are averaged and presented as a whole, *e.g.*, left and right kidney.

Dataset	Anatomical Target	DSC \uparrow				NSD \uparrow				
		SAT-Pro	SAT-Nano	BP (Oracle)	BP	SAT-Pro	SAT-Nano	BP (Oracle)	BP	
ACDC (MRI) [9]	heart ventricle	89.34	87.36	81.97	78.98	72.13	66.63	74.5	68.11	
	myocardium	82.94	79.9	90.26	89.21	73.49	67.2	85.68	83.23	
AMOS22 CT [29]	adrenal gland	75.5	72.81	73.36	4.46	86.12	83.0	68.93	5.37	
	aorta	92.25	92.76	94.12	62.17	91.41	92.24	84.74	40.22	
	duodenum	78.28	75.67	77.66	23.29	69.46	65.45	55.8	13.38	
	esophagus	83.73	82.25	83.47	12.26	85.67	83.8	70.7	9.08	
	gallbladder	78.5	75.06	87.43	18.68	73.01	67.59	71.29	9.95	
	inferior vena cava	89.34	88.72	88.39	36.22	86.35	84.74	67.94	19.72	
	kidney	94.99	94.87	95.35	40.86	91.2	90.17	82.62	27.53	
	liver	95.84	95.84	95.84	95.84	95.84	95.84	95.84	95.84	
	pancreas	84.39	82.63	85.65	39.34	75.63	72.17	64.82	22.1	
	spleen	95.59	95.14	95.52	65.51	90.77	88.15	82.47	39.15	
AMOS22 MRI [29]	stomach	89.4	87.4	90.3	61.73	73.96	68.74	65.05	30.81	
	urinary bladder	82.77	80.3	89.86	28.58	65.22	60.66	72.76	17.27	
	adrenal gland	64.15	62.59	50.07	10.94	76.5	73.95	43.85	9.15	
	aorta	89.35	89.18	75.01	74.52	88.95	88.79	63.48	61.82	
	duodenum	68.42	64.43	53.23	35.36	57.22	53.24	32.8	18.09	
	esophagus	74.21	71.29	53.4	22.39	75.48	72.15	40.66	13.19	
	gallbladder	63.52	58.93	55.25	31.21	51.11	45.66	35.48	11.75	
	inferior vena cava	84.66	83.11	68.32	59.79	80.41	77.44	45.42	37.85	
	kidney	94.57	94.37	88.18	60.69	89.09	88.08	68.47	29.28	
	liver	96.29	96.1	84.3	82.42	81.88	80.95	55.1	51.39	
BTCV Cervix (CT) [38]	pancreas	84.2	79.23	67.26	58.15	72.39	66.29	42.33	31.8	
	spleen	95.19	94.96	86.2	73.88	89.45	88.28	61.51	42.02	
	stomach	85.46	81.99	50.55	46.23	64.78	55.29	22.11	17.44	
	uterus	76.07	77.26	81.0	36.97	48.73	49.31	42.13	10.07	
	MSD Cardiac (MRI) [4]	left heart atrium	92.61	90.28	91.27	73.44	83.14	77.29	49.97	26.44
	MSD HepaticVessel (CT) [4]	liver vessel	60.09	56.01	45.89	32.6	71.01	65.59	49.88	38.62
	MSD Hippocampus (MRI) [4]	hippocampus	89.35	87.99	70.35	66.37	97.54	96.91	43.58	36.65
	MSD Liver (CT) [4]	liver	96.51	96.14	85.68	84.73	79.27	76.52	48.1	43.55
MSD Pancreas (CT) [4]	pancreas	85.31	84.68	69.91	51.56	70.23	68.67	45.82	24.8	
MSD Prostate (MRI) [4]	prostate	87.4	85.17	84.24	74.33	57.75	51.44	40.55	30.77	
MSD Spleen (CT) [4]	spleen	94.12	93.5	91.25	65.08	84.85	80.46	68.72	30.34	

8.2 More Results in External Evaluation

Table 15 | **DSC** results of SAT-Pro, SAT-Nano, nnU-Nets, U-Mamba and SwinUNETR on two held-out dataset AbdomenAtlas 1.1 [74] and LiQA [50]. ‘PV & SV’ stands for Portal Vein And Splenic Vein. The best results are bolded. Note that, MedSAM is interactive and semi-automatic method, while the rest are fully automatic.

Category	SAT-Pro	SAT-Nano	nnU-Nets	U-Mamba	SwinUNETR	MedSAM	Oracle Box
Adrenal Gland	75.63	74.08	72.35	72.08	66.5	60.24	58.55
Aorta	88.27	88.46	81.93	81.59	77.65	85.37	83.61
Colon	65.9	65.64	65.79	65.16	65.2	49.12	45.24
Duodenum	75.48	72.33	69.15	70.04	61.46	64.01	59.71
Esophagus	73.16	73.04	64.35	64.68	58.65	72.26	76.07
Femur	70.52	53.02	64.48	64.9	61.84	81.85	81.33
Gallbladder	72.8	72.86	68.63	70.49	64.72	82.08	78.75
Intestine	76.42	75.8	77.09	77.34	74.79	62.59	55.65
Kidney	93.12	92.93	85.39	87.01	81.5	93.94	88.6
Liver	96.59	96.15	94.72	94.78	91.54	94.8	82.85
Lung	89.59	88.82	85.17	87.53	84.85	60.9	60.61
Pancreas	86.42	84.96	75.99	81.12	70.95	76.92	65.67
PV & SV	55.94	54.32	54.84	55.52	52.96	12.14	11.52
Prostate	25.26	24.26	21.46	22.09	23.39	68.88	72.66
Rectum	63.98	25.25	50.89	59.86	48.92	77.84	80.48
Spleen	94.31	93.64	90.4	92.2	86.43	93.34	82.74
Stomach	81.52	79.26	85.2	86.11	78.6	87.63	80.66
Urinary Bladder	76.31	68.75	70.47	72.77	61.82	85.46	84.16
Liver (MR)	93.5	92.64	68.96	79.19	60.13	90.21	78.13

Table 16 | NSD results of SAT-Pro, SAT-Nano, nnU-Nets, U-Mamba and SwinUNETR on two held-out dataset AbdomenAtlas 1.1 [74] and LiQA [50]. ‘PV & SV’ stands for Portal Vein And Splenic Vein. The best results are bolded. Note that, MedSAM is interactive and semi-automatic method, while the rest are fully automatic.

Category	SAT-Pro	SAT-Nano	nnU-Nets	U-Mamba	SwinUNETR	MedSAM	Oracle Box
Adrenal Gland	85.25	83.42	76.68	76.61	70.26	71.95	65.94
Aorta	87.81	88.29	73.8	73.85	68.25	83.95	78.12
Colon	49.04	48.9	41.08	40.38	40.09	31.7	26.53
Duodenum	64.43	59.31	53.48	54.65	45.49	52.73	46.12
Esophagus	72.86	72.45	57.73	58.42	52.45	72.52	75.63
Femur	60.82	43.97	54.57	55.28	51.69	69.39	66.84
Gallbladder	66.51	65.26	58.86	61.08	53.02	78.01	69.95
Intestine	59.73	59.77	57.15	56.91	55.55	42.14	29.82
Kidney	88.48	87.78	74.74	76.92	69.54	86.87	67.03
Liver	81.61	78.63	72.46	74.1	66.61	73.42	48.79
Lung	80.14	78.0	68.52	73.74	65.37	34.17	29.83
Pancreas	79.2	75.52	60.52	65.72	54.07	62.14	49.06
PV & SV	62.56	60.71	56.58	57.32	55.16	18.51	16.44
Prostate	19.86	17.69	14.76	16.06	15.92	60.28	62.09
Rectum	55.19	25.25	39.48	48.18	37.01	72.25	73.48
Spleen	90.17	87.96	80.48	83.06	73.91	85.0	62.17
Stomach	65.72	60.03	63.46	65.39	54.09	64.53	50.81
Urinary Bladder	67.11	58.57	57.66	60.3	47.86	76.91	71.0
Liver (MR)	68.69	62.79	48.13	52.88	38.64	63.92	43.4

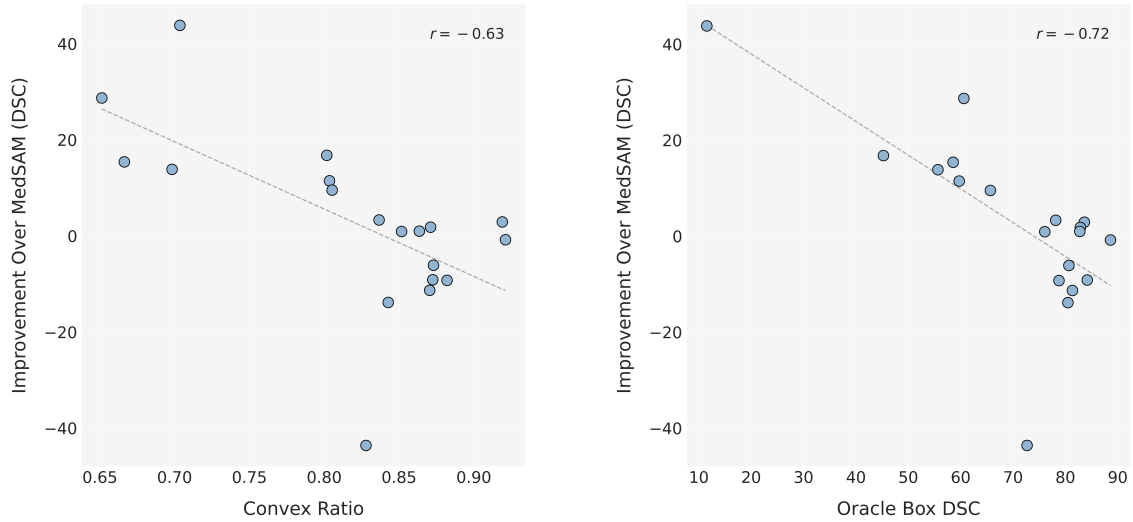


Figure 14 | Scatter plots comparing the performance improvement of SAT-Pro over MedSAM on 19 categories in external evaluation (DSC score), with two irregularity metrics: convex ratio and oracle box DSC. Each point represents an anatomical structure or lesion, with a fitted line illustrating the trend.

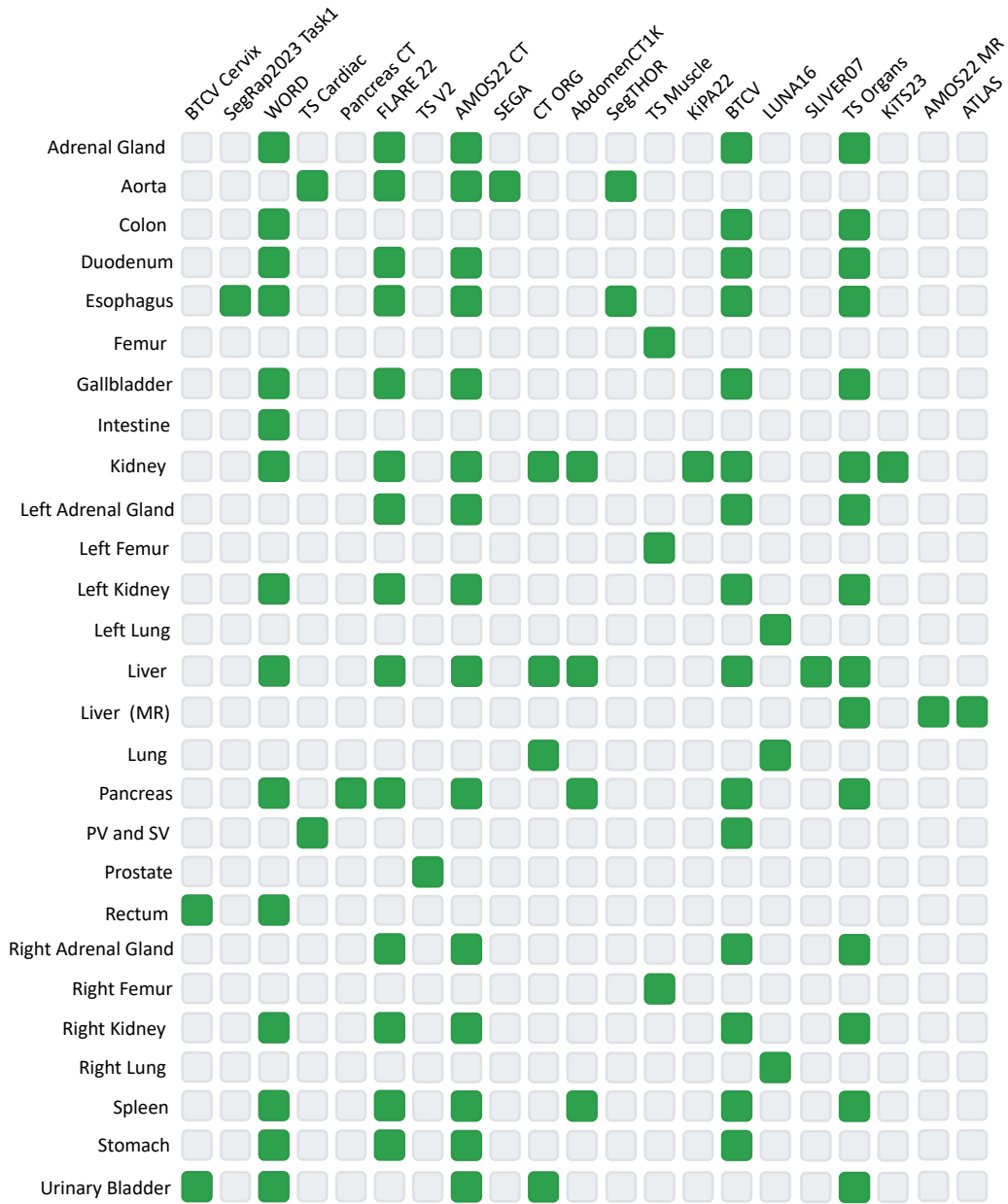


Figure 15 | The detailed transfer mapping of specialist models from 21 datasets to 2 held-out datasets, in the external evaluation. Liver (MR) is from LiQA, while the other categories are from AbdomenAtlas 1.1.

8.3 More Results in Ablation Study

Table 17 | Class-wise results of four SAT-Nano variants with different text encoders on common anatomical structures in thorax, limbs, spine, pelvis, whole body and common lesions. ‘Ours’ denotes the SAT-Nano prompted with the text encoder pre-trained on our multi-modal medical knowledge graph; ‘MedCPT’ denotes the variant with MedCPT as text encoder; ‘Clip’ denotes the variant with Clip text encoder; ‘BB’ denotes the variant with BERT-base as text encoder.

Region	Modality	Anatomical Target	DSC \uparrow				NSD \uparrow			
			Ours	MedCPT	Clip	BB	Ours	MedCPT	Clip	BB
Thorax	CT	Autochthon	93.06	91.97	92.41	92.15	90.33	85.79	87.17	85.95
	CT	Heart atrium	91.13	90.16	90.21	89.29	79.94	76.89	77.48	77.68
	MRI	Heart ventricle	87.49	87.84	88.36	89.31	70.48	71.1	69.71	72.71
	CT	Lung	91.14	90.05	91.38	90.06	84.42	80.81	82.23	80.59
	CT	Rib	86.04	82.54	83.45	83.83	88.76	86.6	87.69	88.45
	CT	Myocardium	84.96	84.28	84.81	86.7	74.58	75.1	72.97	75.97
	CT	Thoracic cavity	95.35	94.64	94.97	94.56	74.4	70.21	71.36	69.38
Lower limb	CT	Head of femur	91.86	88.21	89.02	88.17	81.87	75.11	77.6	74.59
	MRI	Femur bone	95.8	95.43	95.52	95.37	88.57	87.43	87.01	86.9
	MRI	Femur cartilage	68.8	67.85	67.45	66.77	88.03	85.83	86.62	86.15
	MRI	Tibia bone	96.53	96.25	96.42	96.31	93.83	92.24	92.47	92.48
	MRI	Tibia cartilage	67.07	65.47	66.43	65.87	89.48	87.57	88.36	87.98
Spine	CT	Lumbar vertebrae	77.03	73.88	77.84	73.05	76.64	72.58	77.52	71.33
	CT	Sacrum	94.15	92.81	93.39	85.87	94.82	92.75	93.49	85.59
	CT	Spinal cord	82.49	79.99	82.25	76.93	87.46	82.54	87.22	77.93
	CT	Thoracic vertebrae	80.21	79.04	76.04	78.59	80.33	78.67	75.91	78.25
	MRI	Intervertebral discs	88.67	88.21	88.75	88.05	91.43	90.92	91.56	90.42
	MRI	Lumbar vertebrae	81.95	81.49	80.17	81.87	72.96	70.83	72.2	71.08
	MRI	Sacrum	83.71	81.58	82.11	81.4	77.75	73.0	76.27	72.88
Upper limb	MRI	Thoracic vertebrae	64.5	59.57	60.67	64.72	59.06	53.72	55.87	58.12
	CT	Clavicle	92.11	82.82	85.13	85.65	93.24	84.3	86.71	87.04
	CT	Humerus	85.91	80.38	79.3	79.68	86.43	80.17	79.2	79.62
Pelvis	CT	Scapula	92.54	80.47	88.45	88.3	94.7	83.45	91.47	91.46
	CT	Gluteus maximus	94.54	95.39	95.32	94.05	90.96	90.19	90.21	88.63
	CT	Gluteus medius	91.99	90.19	94.07	92.93	88.9	84.74	89.13	87.15
	CT	Gluteus minimus	93.76	91.85	93.01	89.71	93.36	90.26	91.67	87.83
	CT	Hip	95.48	92.95	93.93	93.89	96.14	93.24	94.24	94.13
	CT	Iliopsoas	91.32	89.98	89.95	87.99	91.52	88.72	88.95	86.64
	CT	Iliac vena	90.69	89.17	90.04	85.38	92.32	90.69	91.58	86.72
	CT	Urinary bladder	86.28	83.71	86.97	82.32	69.11	63.38	67.28	61.65
Lesions	MRI	Prostate	83.24	84.23	84.5	82.67	55.04	57.34	57.83	52.78
	CT	Lung nodule	18.91	5.14	6.92	9.96	21.34	8.01	8.15	12.73
	MRI	Myocardial edema	12.24	9.32	13.08	14.41	18.83	14.48	19.43	19.69
	MRI	Stroke	48.14	49.0	49.16	47.83	47.18	46.05	46.34	45.07

Table 18 | Class-wise results of four SAT-Nano variants with different text encoders on common anatomical structures in abdomen, brain, head and neck. ‘Ours’ denotes the SAT-Nano prompted with the text encoder pre-trained on our multi-modal medical knowledge graph; ‘MedCPT’ denotes the variant with MedCPT as text encoder; ‘Clip’ denotes the variant with Clip text encoder; ‘BB’ denotes the variant with BERT-base as text encoder.

Region	Modality	Anatomical Target	DSC \uparrow				NSD \uparrow			
			Ours	MedCPT	Clip	BB	Ours	MedCPT	Clip	BB
Abdomen	CT	Adrenal gland	80.14	78.54	77.98	78.52	88.48	86.94	86.8	86.91
	CT	Duodenum	77.23	75.88	76.65	76.58	68.65	65.15	66.17	66.11
	CT	Gallbladder	81.29	78.48	79.35	79.28	76.4	72.19	72.72	72.76
	CT	Inferior vena cava	89.26	88.41	87.79	87.81	86.06	84.05	83.08	83.26
	CT	Intestine	86.21	82.72	83.41	82.81	72.69	63.93	65.32	64.77
	CT	Kidney	94.08	93.41	93.85	93.34	90.37	88.69	89.12	88.39
	CT	Liver	95.8	94.97	95.03	95.02	83.69	79.47	79.43	79.5
	CT	Pancreas	85.13	82.12	83.72	83.61	76.41	70.91	72.91	72.52
	CT	Small bowel	75.78	78.24	81.51	78.62	68.82	69.27	72.44	69.3
	CT	Spleen	94.71	93.8	93.21	93.57	91.16	88.82	87.86	88.35
	CT	Stomach	85.1	87.93	89.0	89.3	71.75	71.14	71.79	72.39
	MRI	Adrenal gland	61.13	62.99	59.29	60.35	73.1	74.7	70.85	71.36
	MRI	Kidney	91.93	90.34	90.94	90.85	74.61	69.4	71.5	71.03
	MRI	Liver	91.29	90.69	91.63	91.6	64.15	61.02	61.52	60.69
	MRI	Pancreas	81.43	82.78	81.84	82.51	69.09	69.41	68.2	69.02
	MRI	Spleen	84.53	82.11	82.22	82.63	63.45	61.7	61.49	62.31
Brain	CT	Brainstem	86.66	85.2	86.0	84.1	74.95	69.55	72.32	68.18
	CT	Hippocampus	78.36	77.17	78.84	77.02	79.7	77.51	80.48	77.55
	CT	Temporal lobe	94.52	94.26	94.9	94.23	85.6	83.86	86.67	83.86
	MRI	Brain ventricle	77.48	75.86	76.58	76.0	86.27	83.23	84.36	83.26
	MRI	Cerebellum	89.89	88.72	90.23	88.85	84.8	80.23	84.21	80.83
	MRI	Parietal lobe	75.57	74.47	74.77	73.97	57.82	53.83	53.86	53.23
	MRI	Optic radiation	61.06	60.41	62.17	60.99	55.35	52.84	55.41	53.56
	MRI	Thalamus	85.28	84.72	84.14	84.88	85.44	83.69	82.98	83.89
Head and neck	CT	Brain	89.97	96.43	97.91	97.85	86.86	91.38	94.59	93.13
	CT	Carotid artery	66.6	60.76	62.24	60.63	80.1	68.93	71.04	69.05
	CT	Cervical esophagus	61.46	64.13	65.79	61.99	62.33	68.21	67.41	63.18
	CT	Cochlea	70.75	68.99	70.08	69.65	90.59	89.94	90.29	89.88
	CT	Eustachian tube bone	79.42	81.81	81.13	81.71	95.86	97.1	97.11	97.44
	CT	Eyeball	85.84	84.18	84.93	84.88	88.56	85.85	86.48	86.61
	CT	Lacrimal gland	47.62	47.32	41.86	0.0	66.76	65.35	54.39	0.0
	CT	Lens	73.89	73.9	73.15	74.37	90.48	91.87	90.47	91.9
	CT	Mandible	94.3	93.26	93.74	92.79	96.69	95.28	96.23	94.34
	CT	Middle ear	87.04	82.52	86.64	85.11	93.8	88.51	93.66	91.96
	CT	Optic nerve	61.67	70.52	69.7	71.01	78.05	88.25	87.85	88.48
	CT	Parotid gland	85.27	83.89	84.65	84.09	76.23	73.01	74.93	72.81
	CT	Submandibular gland	79.94	78.91	78.24	78.25	77.51	75.9	75.23	74.39
	CT	Tympanic cavity	82.53	81.4	80.53	81.0	95.28	94.7	92.93	94.48
	CT	Thyroid gland	85.61	82.79	84.98	82.49	87.85	82.09	86.55	80.97
	MRI	Brain	95.21	94.72	94.83	94.36	58.25	55.57	57.14	53.53

Table 19 | Dataset-wise results of four SAT-Nano variants with different text encoders on 49 datasets in SAT-DS. ‘Ours’ denotes the SAT-Nano prompted with the text encoder pre-trained on our multi-modal medical knowledge graph; ‘MedCPT’ denotes the variant with MedCPT as text encoder; ‘Clip’ denotes the variant with CLIP text encoder; ‘BB’ denotes the variant with BERT-base as text encoder.

Dataset	DSC \uparrow				NSD \uparrow			
	Ours	MedCPT	Clip	BB	Ours	MedCPT	Clip	BB
AbdomenCT1K [59]	93.14	92.49	92.35	92.41	85.31	82.49	82.44	82.23
ACDC [9]	86.1	85.3	85.88	85.03	69.39	66.39	68.24	65.82
AMOS22 CT [29]	85.81	84.48	84.47	84.31	82.25	79.07	79.28	78.84
AMOS22 MRI [29]	80.58	80.77	80.24	75.44	76.79	75.39	74.93	70.12
ATLAS [75]	62.62	67.9	61.37	69.7	38.47	39.22	36.11	40.53
ATLASR2 [46]	55.15	53.8	55.2	53.39	54.49	49.68	51.41	50.18
Brain Atlas [85]	76.35	74.77	75.15	75.57	76.11	72.64	73.34	73.59
BrainPTM [5]	65.85	66.25	66.13	65.57	53.8	51.95	53.12	51.35
CHAOS MRI [31]	85.06	82.59	83.81	83.67	52.41	46.68	49.08	48.21
CMRxMotion [92]	88.57	87.01	87.41	86.81	75.15	68.85	70.18	67.8
Couinaud Liver [87]	79.28	81.36	72.85	80.44	53.89	54.62	49.25	53.78
CrossMoDA2021 [14]	73.62	71.91	72.27	71.78	93.59	90.98	91.3	91.93
CT ORG [79]	87.02	89.82	90.92	89.15	74.49	75.9	77.46	75.0
CTPelvic1K [49]	95.72	94.76	95.02	94.79	97.37	95.91	96.21	95.84
FeTA2022 [69]	72.19	68.98	70.42	68.69	79.61	75.31	77.42	75.12
FLARE22 [58]	88.42	88.97	88.54	89.19	86.26	85.37	84.69	85.57
FUMPE [61]	35.16	36.11	36.98	30.14	35.83	31.91	37.52	28.93
HAN Seg [71]	70.63	68.95	69.64	65.37	76.56	73.44	74.13	67.88
Instance22 [45]	52.49	61.0	56.67	56.56	42.54	51.65	46.37	46.67
ISLES2022 [24]	41.14	44.2	43.12	42.27	39.87	42.41	41.26	39.96
KiPA22 [21]	63.98	67.52	65.54	67.46	62.13	65.89	62.63	66.51
KiT23 [23]	60.09	53.49	52.9	55.22	51.63	43.66	42.84	45.42
LAScarQS22 Task1 [43]	67.8	65.6	67.2	66.44	79.54	73.42	75.94	74.5
LAScarQS22 Task2 [43]	91.66	88.78	90.14	89.09	79.28	69.87	72.84	69.73
LNDb [70]	18.91	5.14	6.92	9.96	21.34	8.01	8.15	12.73
LUNA16 [86]	96.52	95.92	96.23	96.02	94.85	93.02	92.89	93.25
MM WHS CT [111]	87.79	88.23	87.75	89.08	68.79	69.85	69.05	72.82
MM WHS MRI [111]	84.97	85.82	84.02	85.38	65.32	66.85	63.81	65.89
MRSpineSeg [68]	77.25	76.21	76.64	76.97	74.14	72.45	73.91	72.67
MyoPS2020 [72]	59.55	59.54	60.85	59.68	41.64	40.68	42.94	40.9
NSCLC [8]	75.21	74.17	75.57	75.42	60.88	56.99	59.52	57.3

Table 20 | (Continued) Dataset-wise results of four SAT-Nano variants with different text encoders on 49 datasets in SAT-DS. ‘Ours’ denotes the SAT-Nano prompted with the text encoder pre-trained on our multi-modal medical knowledge graph; ‘MedCPT’ denotes the variant with MedCPT as text encoder; ‘Clip’ denotes the variant with CLIP text encoder; ‘BB’ denotes the variant with BERT-base as text encoder.

Dataset	DSC \uparrow				NSD \uparrow			
	Ours	MedCPT	Clip	BB	Ours	MedCPT	Clip	BB
Pancreas CT [82]	86.47	83.79	84.47	83.89	79.27	72.39	73.61	72.31
PARSE2022 [52]	73.73	68.56	69.29	68.04	70.03	54.16	56.97	51.62
PDDCA [78]	72.98	73.44	72.78	72.9	75.45	74.29	74.46	73.57
PROMISE12 [48]	83.24	84.23	84.5	82.67	55.04	57.34	57.83	52.78
SEGA [77]	80.08	77.68	79.02	79.32	69.56	63.48	66.88	65.51
SegRap2023 Task1 [53]	85.22	85.12	85.7	84.93	90.29	89.72	90.94	89.54
SegRap2023 Task2 [53]	67.35	64.95	64.56	65.69	46.51	43.85	42.52	43.86
SegTHOR [37]	86.17	84.59	85.79	84.8	72.19	67.75	70.74	68.62
SKI10 [40]	82.05	81.25	81.46	81.08	89.98	88.27	88.61	88.38
SLIVER07 [22]	97.41	96.59	96.88	96.74	86.63	80.76	82.39	81.89
TotalSegmentator Cardiac [94]	88.99	86.96	87.96	85.93	86.64	83.04	84.38	81.99
TotalSegmentator Muscles [94]	90.32	87.04	88.35	87.93	89.49	85.15	86.65	85.95
TotalSegmentator Organs [94]	87.18	84.13	86.02	85.37	83.27	78.71	80.77	79.8
TotalSegmentator Ribs [94]	86.27	82.72	83.67	84.0	89.03	86.86	87.99	88.7
TotalSegmentator Vertebrae [94]	85.99	83.25	80.3	81.57	86.73	83.5	80.64	81.77
VerSe [84]	78.19	76.51	70.62	70.77	77.7	75.56	70.32	69.69
WMH Segmentation Challenge [35]	64.61	62.07	62.58	61.59	78.89	75.69	76.48	75.14
WORD [54]	86.49	84.79	85.16	84.79	76.96	72.42	73.42	72.4

Table 21 | Ablation study on knowledge data in knowledge injection, and comparison with variants with other text encoder. ‘Multi-Modal Knowledge’ stands for using both visual and textual knowledge data, *i.e.*, the whole knowledge tree. While ‘Text Knowledge Only’ stands for using the textual knowledge data only. Results are merged by different regions of the human body and lesions. H&N: head and neck, LL: lower limb, UL: upper limb, All: average over all the 429 classes. The best results are **bolded**.

Metric	Method	Brain	H&N	UL	Thorax	Spine	Abdomen	LL	Pelvis	Lesion	All
DSC \uparrow	Multi-Modal Knowledge	75.56	78.46	89.89	87.51	79.44	81.31	83.22	91.77	42.72	79.48
	Text Knowledge Only	75.65	78.34	87.75	84.61	78.80	79.42	82.65	89.52	42.92	78.5
	MedCPT	74.02	77.33	81.32	85.22	77.82	81.28	81.98	89.84	41.95	77.94
	CLIP	74.45	77.75	83.78	85.96	75.67	78.82	81.26	91.27	41.32	77.84
	BERT-Base	74.59	75.48	84.08	85.96	76.10	80.97	81.90	85.60	42.65	77.52
NSD \uparrow	Multi-Modal Knowledge	75.50	84.75	91.06	83.19	78.30	71.86	82.73	88.56	38.68	78.35
	Text Knowledge Only	75.29	84.67	89.22	80.29	78.06	69.77	81.89	85.88	38.68	77.33
	MedCPT	72.13	82.80	82.54	80.64	76.10	70.35	80.01	85.49	36.45	75.70
	CLIP	73.01	83.26	85.27	81.66	74.62	68.49	79.83	87.21	36.61	75.99
	BERT-Base	72.86	79.99	85.36	81.74	74.06	70.08	80.04	80.98	37.33	75.18

Table 22 | Class-wise comparison of three SAT-Nano variants with different visual backbones on common anatomical structures in abdomen, brain, spine, and pelvis. ‘U-Net’ denotes the SAT-Nano based on U-Net; ‘U-Mamba’ denotes the variant based on U-Mamba; ‘SwinUNETR’ denotes the variant based on SwinUNETR.

Region	Modality	Anatomical Target	DSC \uparrow			NSD \uparrow		
			U-Net	U-Mamba	SwinUNETR	U-Net	U-Mamba	SwinUNETR
Abdomen	CT	Adrenal gland	78.54	79.03	71.97	86.94	87.41	79.02
	CT	Duodenum	75.88	73.89	66.05	65.15	63.77	50.51
	CT	Gallbladder	78.48	77.9	67.31	72.19	71.51	54.17
	CT	Inferior vena cava	88.41	87.35	79.98	84.05	82.96	66.37
	CT	Intestine	82.72	83.04	65.65	63.93	65.84	37.69
	CT	Kidney	93.41	93.25	90.74	88.69	88.64	82.23
	CT	Liver	94.97	95.42	92.35	79.47	81.66	65.55
	CT	Pancreas	82.12	83.44	77.43	70.91	73.35	60.9
	CT	Small bowel	78.24	71.92	57.71	69.27	62.77	41.44
	CT	Spleen	93.8	94.36	90.25	88.82	90.02	76.55
	CT	Stomach	87.93	87.39	79.88	71.14	71.46	48.43
	MRI	Adrenal gland	62.99	63.86	59.31	74.7	75.85	69.1
	MRI	Kidney	90.34	90.6	88.76	69.4	70.8	65.11
	MRI	Liver	90.69	90.34	89.57	61.02	61.67	55.64
MRI	Pancreas	82.78	81.32	75.76	69.41	68.49	58.7	
MRI	Spleen	82.11	78.48	81.21	61.7	61.9	55.71	
Brain	CT	Brainstem	85.2	84.33	82.35	69.55	68.91	61.72
	CT	Hippocampus	77.17	70.85	74.46	77.51	71.06	72.25
	CT	Temporal lobe	94.26	93.81	91.0	83.86	82.51	71.79
	MRI	Brain ventricle	75.86	76.04	65.04	83.23	83.34	70.19
	MRI	Cerebellum	88.72	89.18	80.13	80.23	82.15	57.62
	MRI	Parietal lobe	74.47	73.52	64.93	53.83	54.02	42.72
	MRI	Optic radiation	60.41	59.83	61.32	52.84	51.7	52.9
	MRI	Thalamus	84.72	83.77	79.08	83.69	81.27	72.55
Spine	CT	Lumbar vertebrae	73.88	73.37	67.38	72.58	72.01	61.53
	CT	Sacrum	92.81	91.31	89.01	92.75	91.47	85.08
	CT	Spinal cord	79.99	82.07	63.82	82.54	86.83	61.75
	CT	Thoracic vertebrae	79.04	75.64	62.92	78.67	75.49	58.4
	MRI	Intervertebral discs	88.21	87.76	85.97	90.92	89.81	87.49
	MRI	Lumbar vertebrae	81.49	81.15	74.77	70.83	69.76	59.43
	MRI	Sacrum	81.58	81.45	74.59	73.0	74.14	61.25
	MRI	Thoracic vertebrae	59.57	65.46	52.99	53.72	58.69	43.84
Pelvis	CT	Gluteus maximus	95.39	94.64	92.54	90.19	89.45	81.87
	CT	Gluteus medius	90.19	91.09	91.19	84.74	84.93	80.59
	CT	Gluteus minimus	91.85	90.92	86.39	90.26	88.97	80.41
	CT	Hip	92.95	92.91	92.99	93.24	93.1	90.72
	CT	Iliopsoas	89.98	82.42	83.17	88.72	81.21	74.85
	CT	Iliac vena	89.17	89.31	84.71	90.69	90.6	83.26
	CT	Urinary bladder	83.71	84.94	78.64	63.38	64.83	52.45
	MRI	Prostate	84.23	80.32	79.52	57.34	49.03	44.69

Table 23 | Class-wise comparison of three SAT-Nano variants with different visual backbones on common anatomical structures in head and neck, lower limb, upper limb and whole body, and on common lesions. ‘U-Net’ denotes the SAT-Nano based on U-Net; ‘U-Mamba’ denotes the variant based on U-Mamba; ‘SwinUNETR’ denotes the variant based on SwinUNETR.

Region	Modality	Anatomical Target	DSC \uparrow			NSD \uparrow		
			U-Net	U-Mamba	SwinUNETR	U-Net	U-Mamba	SwinUNETR
Head and neck	CT	Brain	96.43	91.95	95.61	91.38	88.45	82.17
	CT	Carotid artery	60.76	62.78	31.49	68.93	72.42	33.11
	CT	Cervical esophagus	64.13	59.58	41.62	68.21	59.77	41.72
	CT	Cochlea	68.99	69.07	66.73	89.94	89.45	89.35
	CT	Eustachian tube bone	81.81	82.44	78.51	97.1	97.6	96.08
	CT	Eyeball	84.18	84.34	79.12	85.85	86.24	76.38
	CT	Lacrimal gland	47.32	48.27	0.0	65.35	66.95	0.0
	CT	Lens	73.9	75.35	63.77	91.87	91.69	82.36
	CT	Mandible	93.26	93.58	88.38	95.28	95.52	85.75
	CT	Middle ear	82.52	83.53	81.2	88.51	89.91	88.92
	CT	Optic nerve	70.52	70.77	62.75	88.25	88.33	78.39
	CT	Parotid gland	83.89	84.66	80.64	73.01	74.85	63.7
	CT	Submandibular gland	78.91	79.45	75.78	75.9	76.93	68.87
	CT	Tympanic cavity	81.4	80.87	76.85	94.7	93.91	92.3
	CT	Thyroid gland	82.79	83.96	74.85	82.09	84.53	64.63
	MRI	Brain	94.72	94.92	94.41	55.57	57.45	54.3
Lower limb	CT	Head of femur	88.21	89.21	85.96	75.11	77.22	66.86
	MRI	Femur bone	95.43	95.24	94.15	87.43	85.94	81.78
	MRI	Femur cartilage	67.85	66.98	63.02	85.83	85.94	82.27
	MRI	Tibia bone	96.25	96.02	94.26	92.24	91.13	84.68
	MRI	Tibia cartilage	65.47	67.24	63.09	87.57	89.2	85.46
Thorax	CT	Autochthon	91.97	90.26	87.01	85.79	83.89	72.14
	CT	Heart atrium	90.16	87.1	86.02	76.89	72.57	65.35
	MRI	Heart ventricle	87.84	83.78	84.54	71.1	64.83	61.81
	CT	Lung	90.05	88.22	85.26	80.81	78.71	66.04
	CT	Rib	82.54	84.08	68.12	86.6	87.62	71.14
	CT	Myocardium	84.28	80.6	79.67	75.1	68.33	62.09
	CT	Thoracic cavity	94.64	94.82	93.81	70.21	69.91	68.41
Upper limb	CT	Clavicle	82.82	78.93	86.24	84.3	80.15	85.73
	CT	Humerus	80.38	77.63	65.62	80.17	78.08	58.56
	CT	Scapula	80.47	80.98	75.47	83.45	83.91	77.06
Abnormal	CT	Lung nodule	5.14	14.9	14.17	8.01	19.03	15.67
	MRI	Myocardial edema	9.32	12.79	15.9	14.48	18.75	20.06
	MRI	Stroke	49.0	49.95	47.74	46.05	47.35	43.42

Table 24 | Dataset-wise Results of three SAT-Nano variants with different visual backbones on 49 datasets in SAT-DS-Nano. ‘U-Net’ denotes the SAT-Nano based on U-Net; ‘U-Mamba’ denotes the variant based on U-Mamba; ‘SwinUNETR’ denotes the variant based on SwinUNETR.

Dataset	DSC \uparrow			NSD \uparrow		
	U-Net	U-Mamba	SwinUNETR	U-Net	U-Mamba	SwinUNETR
AbdomenCT1K [59]	92.49	92.67	89.88	82.49	83.6	74.1
ACDC [9]	85.3	83.82	82.3	66.39	63.68	59.04
AMOS22 CT [29]	85.81	84.71	78.05	82.25	79.65	66.03
AMOS22 MRI [29]	80.77	80.53	75.47	75.39	75.63	66.96
ATLAS [75]	67.9	64.5	63.82	39.22	39.33	36.07
ATLASR2 [46]	53.8	55.96	51.66	49.68	52.06	46.06
Brain Atlas [85]	74.77	75.05	64.99	72.64	73.53	59.49
BrainPTM [5]	66.25	65.09	64.96	51.95	51.08	49.48
CHAOS MRI [31]	82.59	81.14	81.5	46.68	48.2	42.96
CMRxMotion [92]	87.01	86.47	85.48	68.85	67.58	63.75
Couinaud [87]	81.36	80.87	75.58	54.62	54.21	44.92
CrossMoDA2021 [14]	71.91	73.37	68.7	90.98	92.04	89.86
CT-ORG [79]	89.82	88.75	87.65	75.9	75.4	70.02
CTPelvic1K [49]	94.76	95.24	92.58	95.91	96.29	90.89
FeTA2022 [69]	68.98	69.84	60.57	75.31	76.54	65.0
FLARE22 [58]	88.97	89.44	83.05	85.37	86.02	73.77
FUMPE [61]	36.11	34.21	26.01	31.91	32.15	24.98
HAN Seg [71]	68.95	69.89	55.67	73.44	74.97	55.62
Instance22 [45]	61.0	58.64	36.44	51.65	46.78	26.63
ISLES2022 [24]	44.2	43.95	43.82	42.41	42.63	40.77
KiPA22 [21]	67.52	66.34	61.49	65.89	63.84	57.35
KiTS23 [23]	53.49	54.5	49.75	43.66	45.48	38.41
LAScarQS2022 Task1 [43]	65.6	67.08	64.35	73.42	75.82	69.96
LAScarQS2022 Task2 [43]	88.78	87.52	86.06	69.87	68.91	62.89
LNDb [70]	5.14	14.9	14.17	8.01	19.03	15.67
LUNA16 [86]	95.92	96.37	95.28	93.02	93.39	87.52
MMWHS CT [111]	88.23	85.58	85.67	69.85	64.93	62.98
MMWHS MRI [111]	85.82	85.17	82.15	66.85	66.85	59.54
MRSpineSeg [68]	76.21	76.0	68.33	72.45	71.54	61.29
MyoPS2020 [72]	59.54	60.16	59.79	40.68	41.59	40.49
NSCLC [8]	74.17	75.28	73.66	56.99	57.81	55.93
Pancreas CT [82]	83.79	84.52	80.61	72.39	74.27	64.5
PARSE2022 [52]	68.56	68.98	66.84	54.16	62.3	50.61
PDDCA [78]	73.44	74.41	66.88	74.29	76.28	62.7
PROMISE12 [48]	84.23	80.32	79.52	57.34	49.03	44.69

Table 25 | (Continued) Dataset-wise results of three SAT-Nano variants with different visual backbones on 49 datasets in SAT-DS-Nano. ‘U-Net’ denotes the SAT-Nano based on U-Net; ‘U-Mamba’ denotes the variant based on U-Mamba; ‘SwinUNETR’ denotes the variant based on SwinUNETR.

Dataset	DSC \uparrow			NSD \uparrow		
	U-Net	U-Mamba	SwinUNETR	U-Net	U-Mamba	SwinUNETR
SEGA [77]	77.68	78.54	77.95	63.48	66.03	65.03
SegRap2023 Task1 [53]	85.12	84.71	80.8	89.72	89.12	83.27
SegRap2023 Task2 [53]	64.95	65.61	60.77	43.85	44.5	38.78
SegTHOR [37]	84.59	84.73	79.84	67.75	69.23	59.19
SKI10 [40]	81.25	81.37	78.63	88.27	88.06	83.55
SLIVER07 [22]	96.59	96.94	94.96	80.76	84.35	69.25
TS Cardiac [94]	86.96	83.72	81.52	83.04	79.93	72.13
TS Muscles [94]	87.04	85.07	84.61	85.15	83.08	78.19
TS Organs [94]	84.13	82.36	77.69	78.71	76.86	65.08
TS Ribs [94]	82.72	84.1	68.65	86.86	87.7	71.88
TS Vertebrae [94]	83.25	82.04	70.25	83.5	82.43	66.1
VerSe [84]	76.51	70.91	68.36	75.56	70.0	65.09
WMH [35]	62.07	63.85	61.82	75.69	77.98	75.58
WORD [54]	84.79	85.25	78.6	72.42	73.89	59.68

8.4 Detailed Architecture of Specialist Models

Table 26 | The configurations of 72 nnU-Nets trained on each dataset. All nnU-Nets are planned under ‘3d_fullres’ setting. The total size of all the nnU-Nets is around 2247M.

Dataset	Input Size	#Stage	#Depth	#Width	Model Size
AbdomenCT1K [59]	[96 160 160]	6	[2 2 2 2 2 2]	[32 64 128 256 320 320]	31M
ACDC [9]	[10 256 224]	6	[2 2 2 2 2 2]	[32 64 128 256 320 320]	31M
AMOS22 CT [29]	[64 192 160]	6	[2 2 2 2 2 2]	[32 64 128 256 320 320]	31M
AMOS22 MRI [29]	[64 160 224]	6	[2 2 2 2 2 2]	[32 64 128 256 320 320]	31M
ATLASR2 [46]	[128 128 128]	6	[2 2 2 2 2 2]	[32 64 128 256 320 320]	31M
ATLAS [75]	[48 192 224]	6	[2 2 2 2 2 2]	[32 64 128 256 320 320]	31M
autoPET [16]	[80 192 160]	6	[2 2 2 2 2 2]	[32 64 128 256 320 320]	31M
Brain Atlas [85]	[112 128 112]	5	[2 2 2 2 2]	[32 64 128 256 320]	17M
BrainPTM [5]	[112 144 112]	5	[2 2 2 2 2]	[32 64 128 256 320]	17M
BraTS2023 GLI [62]	[128 160 112]	6	[2 2 2 2 2 2]	[32 64 128 256 320 320]	31M
BraTS2023 MEN [36]	[128 160 112]	6	[2 2 2 2 2 2]	[32 64 128 256 320 320]	31M
BraTS2023 MET [64]	[128 160 112]	6	[2 2 2 2 2 2]	[32 64 128 256 320 320]	31M
BraTS2023 PED [32]	[128 128 128]	6	[2 2 2 2 2 2]	[32 64 128 256 320 320]	31M
BraTS2023 SSA [2]	[128 160 112]	6	[2 2 2 2 2 2]	[32 64 128 256 320 320]	31M
BTCV Cervix [38]	[64 192 160]	6	[2 2 2 2 2 2]	[32 64 128 256 320 320]	31M
BTCV Abdomen [38]	[48 192 192]	6	[2 2 2 2 2 2]	[32 64 128 256 320 320]	31M
CHAOS CT [31]	[48 224 192]	6	[2 2 2 2 2 2]	[32 64 128 256 320 320]	31M
CHAOS MRI [31]	[32 192 288]	6	[2 2 2 2 2 2]	[32 64 128 256 320 320]	31M
CMRxMotion [92]	[10 448 384]	7	[2 2 2 2 2 2 2]	[32 64 128 256 320 320 320]	45M
Couinaud [87]	[64 192 192]	6	[2 2 2 2 2 2]	[32 64 128 256 320 320]	31M
COVID-19 CT Seg [57]	[56 192 192]	6	[2 2 2 2 2 2]	[32 64 128 256 320 320]	31M
CrossMoDA2021 [14]	[48 224 192]	6	[2 2 2 2 2 2]	[32 64 128 256 320 320]	31M
CT-ORG [79]	[128 128 128]	6	[2 2 2 2 2 2]	[32 64 128 256 320 320]	31M
CTPelvic1K [49]	[96 160 160]	6	[2 2 2 2 2 2]	[32 64 128 256 320 320]	31M
DAP Atlas [28]	[80 128 128]	6	[2 2 2 2 2 2]	[32 64 128 256 320 320]	31M
FeTA2022 [69]	[96 112 96]	5	[2 2 2 2 2]	[32 64 128 256 320]	17M
FLARE22 [58]	[40 224 192]	6	[2 2 2 2 2 2]	[32 64 128 256 320 320]	31M
FUMPE [61]	[80 192 160]	6	[2 2 2 2 2 2]	[32 64 128 256 320 320]	31M
HAN Seg [71]	[40 224 192]	6	[2 2 2 2 2 2]	[32 64 128 256 320 320]	31M
Hecktor2022 [3]	[128 128 128]	6	[2 2 2 2 2 2]	[32 64 128 256 320 320]	31M
Instance22 [45]	[16 320 320]	7	[2 2 2 2 2 2 2]	[32 64 128 256 320 320 320]	45M
ISLES2022 [24]	[80 96 80]	5	[2 2 2 2 2]	[32 64 128 256 320]	17M
KiPA22 [21]	[160 128 112]	6	[2 2 2 2 2 2]	[32 64 128 256 320 320]	31M
KiTS23 [23]	[128 128 128]	6	[2 2 2 2 2 2]	[32 64 128 256 320 320]	31M
LAScarQS22 Task1 [43]	[24 256 256]	7	[2 2 2 2 2 2 2]	[32 64 128 256 320 320 320]	45M
LAScarQS22 Task2 [43]	[40 256 224]	6	[2 2 2 2 2 2]	[32 64 128 256 320 320]	31M
LNDb [70]	[96 160 160]	6	[2 2 2 2 2 2]	[32 64 128 256 320 320]	31M

Table 27 | (Continued) The configurations of 72 nnU-Nets trained on each dataset. All nnU-Nets are planned under ‘3d_fullres’ setting. The total size of all the nnU-Nets is around 2247M.

Dataset	Input Size	#Stage	#Depth	#Width	Model Size
LUNA16 [86]	[80 192 160]	6	[2 2 2 2 2 2]	[32 64 128 256 320 320]	31M
MM-WHS CT [111]	[80 192 160]	6	[2 2 2 2 2 2]	[32 64 128 256 320 320]	31M
MM-WHS MR [111]	[96 160 160]	6	[2 2 2 2 2 2]	[32 64 128 256 320 320]	31M
MRSpineSeg [68]	[8 640 320]	7	[2 2 2 2 2 2 2]	[32 64 128 256 320 320 320]	43M
MSD Colon [4]	[56 192 192]	6	[2 2 2 2 2 2]	[32 64 128 256 320 320]	31M
MSD Heart [4]	[80 192 160]	6	[2 2 2 2 2 2]	[32 64 128 256 320 320]	31M
MSD HepaticVessel [4]	[64 192 192]	6	[2 2 2 2 2 2]	[32 64 128 256 320 320]	31M
MSD Hippocampus [4]	[40 56 40]	4	[2 2 2 2]	[32 64 128 256]	6M
MSD Liver [4]	[128 128 128]	6	[2 2 2 2 2 2]	[32 64 128 256 320 320]	31M
MSD Lung [4]	[80 192 160]	6	[2 2 2 2 2 2]	[32 64 128 256 320 320]	31M
MSD Pancreas [4]	[40 224 224]	6	[2 2 2 2 2 2]	[32 64 128 256 320 320]	31M
MSD Prostate [4]	[16 320 320]	7	[2 2 2 2 2 2 2]	[32 64 128 256 320 320 320]	45M
MSD Spleen [4]	[64 192 160]	6	[2 2 2 2 2 2]	[32 64 128 256 320 320]	31M
MyoPS2020 [72]	[48 224 224]	6	[2 2 2 2 2 2]	[32 64 128 256 320 320]	31M
NSCLC [8]	[48 224 192]	6	[2 2 2 2 2 2]	[32 64 128 256 320 320]	31M
Pancreas CT [82]	[80 192 160]	6	[2 2 2 2 2 2]	[32 64 128 256 320 320]	31M
PARSE2022 [52]	[96 160 160]	6	[2 2 2 2 2 2]	[32 64 128 256 320 320]	31M
PDDCA [78]	[48 192 192]	6	[2 2 2 2 2 2]	[32 64 128 256 320 320]	31M
PROMISE12 [48]	[20 320 256]	7	[2 2 2 2 2 2 2]	[32 64 128 256 320 320 320]	45M
SEGA [77]	[72 160 160]	6	[2 2 2 2 2 2]	[32 64 128 256 320 320]	31M
SegRap2023 Task1 [53]	[28 256 224]	6	[2 2 2 2 2 2]	[32 64 128 256 320 320]	31M
SegRap2023 Task2 [53]	[28 256 256]	7	[2 2 2 2 2 2 2]	[32 64 128 256 320 320 320]	45M
SegTHOR [37]	[64 192 160]	6	[2 2 2 2 2 2]	[32 64 128 256 320 320]	31M
SKI10 [40]	[64 192 160]	6	[2 2 2 2 2 2]	[32 64 128 256 320 320]	31M
SLIVER07 [22]	[80 192 160]	6	[2 2 2 2 2 2]	[32 64 128 256 320 320]	31M
ToothFairy [13]	[80 192 160]	6	[2 2 2 2 2 2]	[32 64 128 256 320 320]	31M
TS Heart [94]	[128 128 128]	6	[2 2 2 2 2 2]	[32 64 128 256 320 320]	31M
TS Muscles [94]	[128 128 128]	6	[2 2 2 2 2 2]	[32 64 128 256 320 320]	31M
TS Organs [94]	[128 128 128]	6	[2 2 2 2 2 2]	[32 64 128 256 320 320]	31M
TS Ribs [94]	[128 128 128]	6	[2 2 2 2 2 2]	[32 64 128 256 320 320]	31M
TS Vertebrae [94]	[128 128 128]	6	[2 2 2 2 2 2]	[32 64 128 256 320 320]	31M
TS V2 [94]	[128 128 128]	6	[2 2 2 2 2 2]	[32 64 128 256 320 320]	31M
VerSe [84]	[160 128 112]	6	[2 2 2 2 2 2]	[32 64 128 256 320 320]	31M
WMH [35]	[48 224 192]	6	[2 2 2 2 2 2]	[32 64 128 256 320 320]	31M
WORD [54]	[64 192 160]	6	[2 2 2 2 2 2]	[32 64 128 256 320 320]	31M

8.5 All classes in SAT-DS

Table 28 | Detailed name list of the 497 classes involved in SAT-DS.

Name List 1	Name List 2	Name List 3
(ct) abdominal tissue	(ct) adrenal gland	(ct) anterior eyeball
(ct) aorta	(ct) arytenoid	(ct) autochthon
(ct) bone	(ct) brachiocephalic trunk	(ct) brachiocephalic vein
(ct) brain	(ct) brainstem	(ct) breast
(ct) bronchie	(ct) buccal mucosa	(ct) carotid artery
(ct) caudate lobe	(ct) celiac trunk	(ct) cervical esophagus
(ct) cervical vertebrae	(ct) cervical vertebrae 1 (c1)	(ct) cervical vertebrae 2 (c2)
(ct) cervical vertebrae 3 (c3)	(ct) cervical vertebrae 4 (c4)	(ct) cervical vertebrae 5 (c5)
(ct) cervical vertebrae 6 (c6)	(ct) cervical vertebrae 7 (c7)	(ct) cheek
(ct) clavicle	(ct) cochlea	(ct) colon
(ct) colon cancer	(ct) common carotid artery	(ct) costal cartilage
(ct) covid-19 infection	(ct) cricopharyngeal inlet	(ct) duodenum
(ct) esophagus	(ct) eustachian tube bone	(ct) eyeball
(ct) fat	(ct) femur	(ct) gallbladder
(ct) gluteus maximus	(ct) gluteus medius	(ct) gluteus minimus
(ct) gonad	(ct) head of femur	(ct) head of left femur
(ct) head of right femur	(ct) heart	(ct) heart ascending aorta
(ct) heart atrium	(ct) heart tissue	(ct) heart ventricle
(ct) hip	(ct) hippocampus	(ct) humerus
(ct) iliac artery	(ct) iliac vena	(ct) iliopsoas
(ct) inferior alveolar nerve	(ct) inferior vena cava	(ct) internal auditory canal
(ct) internal carotid artery	(ct) internal jugular vein	(ct) intestine
(ct) intracranial hemorrhage	(ct) kidney	(ct) kidney cyst
(ct) kidney tumor	(ct) lacrimal gland	(ct) larynx
(ct) larynx glottis	(ct) larynx supraglottis	(ct) left adrenal gland
(ct) left anterior eyeball	(ct) left auricle of heart	(ct) left autochthon
(ct) left brachiocephalic vein	(ct) left breast	(ct) left carotid artery
(ct) left cheek	(ct) left clavicle	(ct) left cochlea
(ct) left common carotid artery	(ct) left eustachian tube bone	(ct) left eyeball
(ct) left femur	(ct) left gluteus maximus	(ct) left gluteus medius
(ct) left gluteus minimus	(ct) left heart atrium	(ct) left heart ventricle
(ct) left hip	(ct) left hippocampus	(ct) left humerus
(ct) left iliac artery	(ct) left iliac vena	(ct) left iliopsoas
(ct) left internal auditory canal	(ct) left internal carotid artery	(ct) left internal jugular vein
(ct) left kidney	(ct) left kidney cyst	(ct) left lacrimal gland
(ct) left lateral inferior segment of liver	(ct) left lateral superior segment of liver	(ct) left lens
(ct) left lobe of liver	(ct) left lung	(ct) left lung lower lobe
(ct) left lung upper lobe	(ct) left mandible	(ct) left mastoid process
(ct) left medial segment of liver	(ct) left middle ear	(ct) left optic nerve
(ct) left parotid gland	(ct) left posterior eyeball	(ct) left rib
(ct) left rib 1	(ct) left rib 10	(ct) left rib 11
(ct) left rib 12	(ct) left rib 2	(ct) left rib 3
(ct) left rib 4	(ct) left rib 5	(ct) left rib 6
(ct) left rib 7	(ct) left rib 8	(ct) left rib 9
(ct) left scapula	(ct) left subclavian artery	(ct) left submandibular gland
(ct) left temporal lobe	(ct) left temporomandibular joint	(ct) left thyroid
(ct) left tympanic cavity	(ct) left vestibule semicircular canal	(ct) lens
(ct) lips	(ct) liver	(ct) liver tumor
(ct) liver vessel	(ct) lumbar vertebrae	(ct) lumbar vertebrae 1 (l1)
(ct) lumbar vertebrae 2 (l2)	(ct) lumbar vertebrae 3 (l3)	(ct) lumbar vertebrae 4 (l4)
(ct) lumbar vertebrae 5 (l5)	(ct) lumbar vertebrae 6 (l6)	(ct) lung
(ct) lung effusion	(ct) lung lower lobe	(ct) lung nodule

Table 29 | (Continued) Detailed name list of the 497 classes involved in SAT-DS.

Name List 1	Name List 2	Name List 3
(ct) lung tumor	(ct) lung upper lobe	(ct) mandible
(ct) manubrium of sternum	(ct) mastoid process	(ct) mediastinal tissue
(ct) middle ear	(ct) muscle	(ct) myocardium
(ct) nasal cavity	(ct) nasopharyngeal lymph node	(ct) nasopharyngeal tumor
(ct) optic chiasm	(ct) optic nerve	(ct) oral cavity
(ct) pancreas	(ct) pancreas tumor	(ct) parotid gland
(ct) pharynx constrictor muscle	(ct) pituitary gland	(ct) portal vein and splenic vein
(ct) posterior eyeball	(ct) prostate	(ct) pulmonary artery
(ct) pulmonary embolism	(ct) pulmonary vein	(ct) rectum
(ct) renal artery	(ct) renal vein	(ct) rib
(ct) rib 1	(ct) rib 10	(ct) rib 11
(ct) rib 12	(ct) rib 2	(ct) rib 3
(ct) rib 4	(ct) rib 5	(ct) rib 6
(ct) rib 7	(ct) rib 8	(ct) rib 9
(ct) rib cartilage	(ct) right adrenal gland	(ct) right anterior eyeball
(ct) right anterior inferior segment of liver	(ct) right anterior superior segment of liver	(ct) right autochthon
(ct) right brachiocephalic vein	(ct) right breast	(ct) right carotid artery
(ct) right cheek	(ct) right clavicle	(ct) right cochlea
(ct) right common carotid artery	(ct) right eustachian tube bone	(ct) right eyeball
(ct) right femur	(ct) right gluteus maximus	(ct) right gluteus medius
(ct) right gluteus minimus	(ct) right heart atrium	(ct) right heart ventricle
(ct) right hip	(ct) right hippocampus	(ct) right humerus
(ct) right iliac artery	(ct) right iliac vena	(ct) right iliopsoas
(ct) right internal auditory canal	(ct) right internal carotid artery	(ct) right internal jugular vein
(ct) right kidney	(ct) right kidney cyst	(ct) right lacrimal gland
(ct) right lens	(ct) right lobe of liver	(ct) right lung
(ct) right lung lower lobe	(ct) right lung middle lobe	(ct) right lung upper lobe
(ct) right mandible	(ct) right mastoid process	(ct) right middle ear
(ct) right optic nerve	(ct) right parotid gland	(ct) right posterior eyeball
(ct) right posterior inferior segment of liver	(ct) right posterior superior segment of liver	(ct) right rib
(ct) right rib 1	(ct) right rib 10	(ct) right rib 11
(ct) right rib 12	(ct) right rib 2	(ct) right rib 3
(ct) right rib 4	(ct) right rib 5	(ct) right rib 6
(ct) right rib 7	(ct) right rib 8	(ct) right rib 9
(ct) right scapula	(ct) right subclavian artery	(ct) right submandibular gland
(ct) right temporal lobe	(ct) right temporomandibular joint	(ct) right thyroid
(ct) right tympanic cavity	(ct) right vestibule semicircular canal	(ct) sacral vertebrae 1 (s1)
(ct) sacrum	(ct) scapula	(ct) skin
(ct) skull	(ct) small bowel	(ct) spinal canal
(ct) spinal cord	(ct) spleen	(ct) sternum
(ct) stomach	(ct) subclavian artery	(ct) submandibular gland
(ct) superior vena cava	(ct) temporal lobe	(ct) temporomandibular joint
(ct) thoracic cavity	(ct) thoracic vertebrae	(ct) thoracic vertebrae 1 (t1)
(ct) thoracic vertebrae 10 (t10)	(ct) thoracic vertebrae 11 (t11)	(ct) thoracic vertebrae 12 (t12)
(ct) thoracic vertebrae 2 (t2)	(ct) thoracic vertebrae 3 (t3)	(ct) thoracic vertebrae 4 (t4)
(ct) thoracic vertebrae 5 (t5)	(ct) thoracic vertebrae 6 (t6)	(ct) thoracic vertebrae 7 (t7)
(ct) thoracic vertebrae 8 (t8)	(ct) thoracic vertebrae 9 (t9)	(ct) thymus
(ct) thyroid gland	(ct) trachea	(ct) tympanic cavity
(ct) urinary bladder	(ct) uterocervix	(ct) uterus
(ct) vertebrae	(ct) vestibule semicircular canal	(mri) adrenal gland
(mri) amygdala	(mri) anterior hippocampus	(mri) aorta

Table 30 | (Continued) Detailed name list of the 497 classes involved in SAT-DS.

Name List 1	Name List 2	Name List 3
(mri) basal ganglia	(mri) brain	(mri) brain edema
(mri) brain tumor	(mri) brain ventricle	(mri) brainstem
(mri) brainstem excluding substantia nigra	(mri) cerebellum	(mri) cingulate gyrus
(mri) cochlea	(mri) corpus callosum	(mri) corticospinal tract
(mri) deep grey matter	(mri) duodenum	(mri) enhancing brain tumor
(mri) esophagus	(mri) external cerebrospinal fluid	(mri) femur bone
(mri) femur cartilage	(mri) frontal lobe	(mri) gallbladder
(mri) grey matter	(mri) heart ascending aorta	(mri) heart atrium
(mri) heart ventricle	(mri) hippocampus	(mri) inferior vena cava
(mri) insula	(mri) intervertebral disc between lumbar vertebrae 1 (l1) and lumbar vertebrae 2 (l2)	(mri) intervertebral disc between lumbar vertebrae 2 (l2) and lumbar vertebrae 3 (l3)
(mri) intervertebral disc between lumbar vertebrae 3 (l3) and lumbar vertebrae 4 (l4)	(mri) intervertebral disc between lumbar vertebrae 4 (l4) and lumbar vertebrae 5 (l5)	(mri) intervertebral disc between lumbar vertebrae 5 (l5) and sacrum
(mri) intervertebral disc between thoracic vertebrae 10 (t10) and thoracic vertebrae 11 (t11)	(mri) intervertebral disc between thoracic vertebrae 11 (t11) and thoracic vertebrae 12 (t12)	(mri) intervertebral disc between thoracic vertebrae 12 (t12) and lumbar vertebrae 1 (l1)
(mri) intervertebral disc between thoracic vertebrae 9 (t9) and thoracic vertebrae 10 (t10)	(mri) intervertebral discs	(mri) kidney
(mri) lateral ventricle	(mri) left adrenal gland	(mri) left amygdala
(mri) left angular gyrus	(mri) left anterior cingulate gyrus	(mri) left anterior orbital gyrus
(mri) left anterior temporal lobe lateral part	(mri) left anterior temporal lobe medial part	(mri) left caudate nucleus
(mri) left cerebellum	(mri) left corticospinal tract	(mri) left cuneus
(mri) left fusiform gyrus	(mri) left heart atrium	(mri) left heart atrium scar
(mri) left heart ventricle	(mri) left hippocampus	(mri) left inferior frontal gyrus
(mri) left insula anterior inferior cortex	(mri) left insula anterior long gyrus	(mri) left insula anterior short gyrus
(mri) left insula middle short gyrus	(mri) left insula posterior long gyrus	(mri) left insula posterior short gyrus
(mri) left kidney	(mri) left lateral orbital gyrus	(mri) left lateral remainder occipital lobe
(mri) left lateral ventricle excluding temporal horn	(mri) left lateral ventricle temporal horn	(mri) left lingual gyrus
(mri) left medial orbital gyrus	(mri) left middle and inferior temporal gyrus	(mri) left middle frontal gyrus
(mri) left nucleus accumbens	(mri) left optic radiation	(mri) left pallidum
(mri) left parahippocampal and ambient gyrus	(mri) left postcentral gyrus	(mri) left posterior cingulate gyrus
(mri) left posterior orbital gyrus	(mri) left posterior temporal lobe	(mri) left pre-subgenual frontal cortex
(mri) left precentral gyrus	(mri) left putamen	(mri) left straight gyrus
(mri) left subcallosal area	(mri) left subgenual frontal cortex	(mri) left substantia nigra
(mri) left superior frontal gyrus	(mri) left superior parietal gyrus	(mri) left superior temporal gyrus anterior part
(mri) left superior temporal gyrus middle part	(mri) left supramarginal gyrus	(mri) left thalamus
(mri) liver	(mri) liver tumor	(mri) lumbar vertebrae
(mri) lumbar vertebrae 1 (l1)	(mri) lumbar vertebrae 2 (l2)	(mri) lumbar vertebrae 3 (l3)
(mri) lumbar vertebrae 4 (l4)	(mri) lumbar vertebrae 5 (l5)	(mri) myocardial edema
(mri) myocardial scar	(mri) myocardium	(mri) necrotic brain tumor core
(mri) occipital lobe	(mri) optic radiation	(mri) pancreas
(mri) parietal lobe	(mri) peripheral zone of prostate	(mri) posterior hippocampus

Table 31 | (Continued) Detailed name list of the 497 classes involved in SAT-DS.

Name List 1	Name List 2	Name List 3
(mri) prostate	(mri) pulmonary artery	(mri) right adrenal gland
(mri) right amygdala	(mri) right angular gyrus	(mri) right anterior cingulate gyrus
(mri) right anterior orbital gyrus	(mri) right anterior temporal lobe lateral part	(mri) right anterior temporal lobe medial part
(mri) right caudate nucleus	(mri) right cerebellum	(mri) right corticospinal tract
(mri) right cuneus	(mri) right fusiform gyrus	(mri) right heart atrium
(mri) right heart ventricle	(mri) right hippocampus	(mri) right inferior frontal gyrus
(mri) right insula anterior inferior cortex	(mri) right insula anterior long gyrus	(mri) right insula anterior short gyrus
(mri) right insula middle short gyrus	(mri) right insula posterior long gyrus	(mri) right insula posterior short gyrus
(mri) right kidney	(mri) right lateral orbital gyrus	(mri) right lateral remainder occipital lobe
(mri) right lateral ventricle excluding temporal horn	(mri) right lateral ventricle temporal horn	(mri) right lingual gyrus
(mri) right medial orbital gyrus	(mri) right middle and inferior temporal gyrus	(mri) right middle frontal gyrus
(mri) right nucleus accumbens	(mri) right optic radiation	(mri) right pallidum
(mri) right parahippocampal and ambient gyrus	(mri) right postcentral gyrus	(mri) right posterior cingulate gyrus
(mri) right posterior orbital gyrus	(mri) right posterior temporal lobe	(mri) right pre-subgenual frontal cortex
(mri) right precentral gyrus	(mri) right putamen	(mri) right straight gyrus
(mri) right subcallosal area	(mri) right subgenual frontal cortex	(mri) right substantia nigra
(mri) right superior frontal gyrus	(mri) right superior parietal gyrus	(mri) right superior temporal gyrus anterior part
(mri) right superior temporal gyrus middle part	(mri) right supramarginal gyrus	(mri) right thalamus
(mri) sacrum	(mri) spleen	(mri) stomach
(mri) stroke	(mri) temporal lobe	(mri) thalamus
(mri) third ventricle	(mri) thoracic vertebrae	(mri) thoracic vertebrae 10 (t10)
(mri) thoracic vertebrae 11 (t11)	(mri) thoracic vertebrae 12 (t12)	(mri) thoracic vertebrae 9 (t9)
(mri) tibia bone	(mri) tibia cartilage	(mri) transition zone of prostate
(mri) urinary bladder	(mri) vertebrae	(mri) vestibular schwannoma
(mri) white matter	(mri) white matter hyperintensities	(pet) head and neck tumor
(pet) lymph node	(pet) tumor	

8.6 Dataset Details of SAT-DS

Table 32 | The 72 datasets we collect to build up SAT-DS. Dataset not marked with * are included in SAT-DS-Nano.

Dataset Name	#Scans	#Classes	#Annotations	Region
CT Data				
AbdomenCT1K [59]	988	4	3,950	Abdomen
ACDC [9]	300	4	1,200	Thorax
AMOS22 CT [29]	300	16	4,765	Abdomen
BTCV Abdomen * [38]	30	15	448	Abdomen
BTCV Cervix * [38]	30	4	118	Abdomen
CHAOS CT * [31]	20	1	20	Abdomen
Couinaud [87]	161	10	1,599	Abdomen
COVID-19 CT Seg * [57]	20	4	80	Thorax
CrossMoDA2021 [14]	105	2	210	Head and Neck
CT-ORG [79]	140	6	680	Whole Body
CTPelvic1K [49]	117	5	585	Lower Limb
DAP Atlas * [28]	533	179	93072	Whole Body
FLARE22 [58]	50	15	750	Abdomen
FUMPE [61]	35	1	33	Thorax
HAN Seg [71]	41	41	1,681	Head and Neck
INSTANCE [45]	100	1	100	Brain
KiPA22 [21]	70	4	280	Abdomen
KiTS23 [23]	489	3	1226	Abdomen
LNDb [70]	236	1	206	Thorax
LUNA16 [86]	888	4	3,551	Thorax
MM-WHS CT [111]	40	9	180	Thorax
MSD Colon * [4]	126	1	126	Abdomen
MSD HepaticVessel * [4]	303	2	606	Abdomen
MSD Liver * [4]	131	2	249	Abdomen
MSD Lung * [4]	63	1	63	Thorax
MSD Pancreas * [4]	281	2	562	Abdomen
MSD Spleen * [4]	41	1	41	Abdomen
NSCLC [8]	85	2	162	Thorax
Pancreas CT [82]	80	1	80	Abdomen
Parse2022 [52]	100	1	100	Thorax
PDDCA [78]	48	12	543	Head and Neck
SEGA [77]	56	1	56	Thorax
SegRap2023 Task 1 [53]	120	61	7320	Head and Neck
SegRap2023 Task 2 [53]	120	2	240	Head and Neck
SegTHOR [37]	40	4	160	Thorax
SLIVER07 [22]	20	1	20	Abdomen

Table 33 | (Continued) The 72 datasets we collect to build up SAT-DS. Dataset not marked with * are included in SAT-DS-Nano.

Dataset Name	#Scans	#Classes	#Annotations	Region
ToothFairy * [13]	153	1	153	Head and Neck
TotalSegmentor Cardiac [94]	1,202	17	13,264	Whole Body
TotalSegmentor Muscles [94]	1,202	31	21,510	Whole Body
TotalSegmentor Organs [94]	1,202	24	20,361	Whole Body
TotalSegmentor Ribs [94]	1,202	39	32,666	Whole Body
TotalSegmentor Vertebrae [94]	1,202	29	19,503	Whole Body
TotalSegmentor V2 * [94]	1,202	24	15,729	Whole Body
VerSe [84]	96	29	1,295	Spine
WORD [54]	150	18	2,700	Abdomen
MRI Data				
AMOS22 MRI [29]	60	16	896	Abdomen
ATLAS [75]	60	2	120	Abdomen
ATLASR2 [46]	654	1	652	Brain
Brain Atlas [85]	30	108	3,240	Brain
BrainPTM [5]	60	7	408	Brain
BraTS2023 GLI * [62]	5004	4	19680	Brain
BraTS2023 MEN * [36]	4000	4	11420	Brain
BraTS2023 MET * [64]	951	4	3476	Brain
BraTS2023 PED * [32]	396	4	1328	Brain
BraTS2023 SSA * [2]	240	4	940	Brain
CHAOS MRI [31]	60	5	300	Abdomen
CMRxMotion [92]	138	4	536	Thorax
FeTA2022 [69]	80	7	560	Brain
ISLES2022 [24]	500	1	492	Brain
LAScarQS2022 Task 1 [43]	60	2	120	Thorax
LAScarQS2022 Task 2 [43]	130	1	130	Thorax
MM-WHS MRI [111]	40	9	180	Thorax
MRSpineSeg [68]	91	23	1,783	Spine
MSD Cardiac * [4]	20	1	20	Thorax
MSD Hippocampus * [4]	260	3	780	Brain
MSD Prostate * [4]	64	2	124	Pelvis
MyoPS2020 [72]	135	6	450	Thorax
PROMISE12 [48]	50	1	50	Pelvis
SKI10 [40]	99	4	396	Upper Limb
WMH [35]	170	1	170	Brain
PET Data				
autoPET * [16]	501	1	501	Whole Body
HECKTOR2022 * [3]	524	2	972	Head and Neck
Summary	22,186	497	302,033	/

8.7 Examples From the Knowledge Tree

Table 34 | Textual knowledge examples from the constructed knowledge tree. *Def* indicates the definition of the concept; *Rel* indicates the relationship with other concept.

Concept	Knowledge
Brain	<i>Rel</i> : Situated above, cerebellum
Caudate lobe	<i>Rel</i> : Connected to (via caudate process), the right lobe
Cingulate gyrus	<i>Rel</i> : Connected to, parahippocampal gyrus
Femur	<i>Rel</i> : Surrounded by, strong ligaments
Heart atrium	<i>Rel</i> : Spatially related to, Right Ventricle (for the Right Atrium)
Iliac artery	<i>Rel</i> : Runs posterior to, inguinal ligament
Lateral ventricle	<i>Rel</i> : Forms a frame around, thalamus
Left femur	<i>Rel</i> : Articulates with, patella
Left heart ventricle	<i>Rel</i> : Located in, bottom left portion of the heart
Left lens	<i>Rel</i> : Located within, left eye
Left rib 6	<i>Rel</i> : Articulates posteriorly with, vertebral column
Lung	<i>Rel</i> : Posteriorly related to, vertebra
Optic chiasm	<i>Rel</i> : Closely associated with, anterior cerebral artery
Optic nerve	<i>Rel</i> : Passes through, posterior orbit
Oral cavity	<i>Rel</i> : Bounded externally by, lips and cheek mucosa
Pulmonary artery	<i>Rel</i> : Carries, deoxygenated blood to the lungs
Pulmonary artery	<i>Rel</i> : Lies anterior to, the right mainstem bronchus
Pulmonary embolism	<i>Rel</i> : Affects, main pulmonary artery (for larger obstructions)
Right amygdala	<i>Rel</i> : Part of, limbic system
Right clavicle	<i>Rel</i> : Extends between, acromion of the scapula
Right hippocampus	<i>Rel</i> : Involved in, storage of long-term memory
Right kidney	<i>Rel</i> : Close proximity to, liver, intestines, diaphragm
Spinal cord	<i>Rel</i> : Extends from, C1 vertebra
Temporomandibular joint	<i>Rel</i> : Coated with, fibrocartilage (articulating surfaces)
Urinary bladder	<i>Rel</i> : Located posterior to, symphysis pubis
Thoracic vertebrae 3 (T3)	<i>Rel</i> : Articulates with, heads of the ribs (via demi-facets)
Bronchie	<i>Def</i> : These structures are crucial airways leading into the lungs, forming a part of the lower respiratory system and facilitating the movement of air to and from the bronchopulmonary segments. The walls are composed of respiratory mucosa, which includes mucous-secreting cells, alongside cartilage plates that provide structural support. Furthermore, smooth muscle fibers are present to regulate the airway's diameter, with an outer layer, known as the adventitia, anchoring these airways to the surrounding lung tissues. The trachea, situated at the neck's front, divides into the right and left primary branches of these airways. Each branch serves as a conduit for air into the smaller subdivisions within the lungs. The structural components are quite similar to those of the trachea, with modifications in the form of cartilage plates instead of complete rings, ensuring flexibility and support. In conclusion, these air passages are pivotal for respiratory function, distinguished by their structural composition and their role in air delivery to lung segments. Originating from the trachea, they extend into the lungs, demonstrating significant anatomical relationships with nearby structures, ensuring efficient lung ventilation.

Table 35 | (Continued) Examples of textual knowledge from the constructed knowledge tree. *Def* indicates the definition of the concept; *Rel* indicates the relationship with other concept.

Concept	Knowledge
Eyeball	<i>Def</i> : This spheroidal structure, present in all vertebrates, functions similarly to a simple camera by housing the retina - a layer rich in photoreceptors necessary for vision. It resides within the skull's orbit, bordered by various facial bones and cushioned by fat. This bilateral and spherical organ features a tough exterior known as the sclera, which is overlaid anteriorly by the conjunctiva to prevent drying. Comprising three layers, its fibrous exterior encompasses the sclera and cornea for shape and support, while the vascular and inner layers include crucial components for blood supply and neural functions, respectively. It connects to the brain via the optic nerve, facilitating the transfer of visual information, and houses the lens and vitreous cavity, crucial for focusing light and maintaining shape, filled with vitreous humor.
Head of right femur	<i>Def</i> : This structure is found at the proximal end of the femur, engaging with the pelvis's acetabulum to establish the hip joint. It adopts a nearly spherical form, positioned superomedially and extending anteriorly from the femur's neck. Its smooth convex surface is interrupted by a depression, the fovea for the ligament, on its posteroinferior aspect. Its surface is mostly smooth and coated with articular cartilage, excluding the fovea where the ligamentum teres finds its attachment. This organ interacts with the acetabulum to create the hip joint and is linked to the neck of the femur, which connects its shaft and head at an angle conducive to efficient walking. Additionally, the ligamentum teres femoris bridges the gap between the acetabulum and a pit located on this structure.
Lateral ventricle	<i>Def</i> : Situated within the cerebral hemispheres, these C-shaped structures span the cerebrum, extending throughout the occipital, frontal, and parietal lobes. They consist of a central part and three horns extending anteriorly, posteriorly, and inferiorly. The central section of this structure is elongated in an anteroposterior direction and showcases a triangular cross-section. It is topped by the corpus callosum's trunk. Composed of five sections: the frontal horn, the body, the atrium, the occipital horn, and the temporal horn, they are surrounded by significant anatomical structures including the putamen, globus pallidus, thalamus, fornix, septum pellucidum, hippocampus, amygdala, and deep cerebral white matter.
Left lacrimal gland	<i>Def</i> : This structure, recognized as the tear gland, finds its position atop the eyeball, nestled in the lacrimal fossa of the orbit's anterior upper outer quadrant - a niche carved out by the orbital plate of the frontal bone. Compact, stretching about 2cm, it comprises two interlinked sections: the predominant orbital portion and the diminutive palpebral section. The former claims the territory above the lateral edge of the levator palpebrae superioris muscle, mirroring the dimensions and form of an almond, peculiarly resembling a J-shaped serous gland. Tasked with a continuous flow, this organ secretes a fluid that bathes the eye, simultaneously cleansing and safeguarding its surface while providing essential lubrication.
Liver	<i>Def</i> : A large organ found in the upper right quadrant of the abdomen, it stands as the largest gland within the human body, with a weight of about 1.5 kilograms. This structure exhibits a reddish-brown hue and is cone or wedge-shaped, having the smaller end positioned near the spleen and stomach while the larger end is over the small intestine. Except for its bare area where it meets the diaphragm, this organ is entirely enveloped by visceral peritoneum. It is comprised of several lobes, namely the right lobe, left lobe, caudate lobe, and quadrate lobe, while essentially being divided into two main lobes which include eight segments housing 1,000 lobules each. These lobules are linked to small ducts, merging into larger ones to eventually form the common hepatic duct. This duct is crucial for transporting bile produced by the organ's cells to the gallbladder and duodenum via the common bile duct. Positioned beneath the diaphragm and resting atop the stomach, right kidney, and intestines, this organ is predominantly intraperitoneal, stretching from the fifth intercostal space in the midclavicular line to the right costal margin. Its superior posterior portion presents a bare area where it interfaces directly with the diaphragm and the inferior vena cava. In terms of structure, the organ is made up of hepatocytes arranged in hexagonally shaped lobules, with each lobule centering around a central vein. Between these hepatocyte cords are vascular spaces known as sinusoids, characterized by their thin fenestrated endothelium and a discontinuous membrane.
Lumbar vertebrae	<i>Def</i> : Positioned in the lower back, this structure forms part of the spine, comprising five cylindrical bones labeled L1 to L5. These segments are the largest in the vertebral column and are designed for weight-bearing, with their kidney-shaped bodies growing in size from top to bottom. Their pedicles and laminae are robust, supporting the attachment of strong back muscles through short, sturdy spinous processes. Compared to other spinal vertebrae, these bones are distinct because they do not possess features like transverse foramina or bifid spinous processes. Their spinous processes are compact and do not extend beneath their body level. Facing medially, the superior articular facets, and laterally, the inferior articular facets, provide unique spatial relationships, including the presence of accessory and mammillary processes. The fifth bone is notably the largest and plays a pivotal role in transferring the torso's weight to the base of the sacrum, where the spinal cord ends around the L1/L2 level. This organ is essential for weight support while standing and is designed for a high degree of extension due to the size of its corresponding intervertebral discs. Furthermore, its ability to facilitate needle access for procedures like epidural anesthesia highlights its clinical significance.

Table 36 | (Continued) Textual knowledge examples from the constructed knowledge tree. *Def* indicates the definition of the concept; *Rel* indicates the relationship with other concept.

Concept	Knowledge
Occipital lobe	<i>Def</i> : Positioned at the brain's rear, right behind the temporal and parietal regions, and beneath the skull's occipital bone, this organ is the brain's smallest by area, representing roughly 12% of the cerebral cortex. Its boundaries, somewhat arbitrarily determined, give it a triangular shape, situating it posterior to the parietal and temporal regions. It hosts a series of folds, including gyri and sulci, and features different functional areas. The primary and secondary visual cortices, alongside specific other areas, contribute to the ongoing visual representation based on retinal inputs. Separated from the temporal region by an imaginary line aligning with the parietooccipital sulcus, its extent reaches from its pole to the mentioned sulcus. This structure finds itself beneath the parietal region, above the temporal one towards the brain's back, sitting on the tentorium cerebelli which itself segregates it from the cerebellum below. It stands as the visual processing center, deciphering color, form, and movement.
Scapula	<i>Def</i> : Located in the upper thoracic region on the dorsal surface of the rib cage, this triangular-shaped, flat bone is found. It sits adjacent to the posterior surface of ribs 2-7 and forms joints with the humerus and clavicle, contributing to the shoulder joint's structure. On its anterior aspect, a smooth, concave area - primarily the subscapular fossa - is present, from which the subscapularis muscle takes its origin. The coracoid process, resembling a beak, protrudes anterolaterally from the superior border here. Meanwhile, the posterior aspect is characterized by a convex, ridge-divided area that separates into the superior supraspinous fossa and the larger inferior infraspinous fossa. Noteworthy are two processes: the coracoid and the acromion, with the latter articulating with the clavicle. This structure bridges the upper limb to the trunk, offering attachment points for a multitude of muscles such as the levator scapulae, teres major, and the muscles of the rotator cuff, thereby playing an essential role in shoulder joint stability and movement.
Spleen	<i>Def</i> : Located in the left hypochondriac region, specifically in the left upper quadrant, this organ is found posterior to the stomach and anterior to the left hemidiaphragm, nestled at the level of the 9th to 11th ribs. Medially, it is close to the left kidney, and below it directly contacts the left colic flexure. This structure, resembling the size of a clenched fist, possesses a smooth, convex surface facing the diaphragm and is distinguished by a ridge that divides it into an anterior gastric portion and a posterior renal portion. The anterior surface is broad, concave, and aims forward and upwards, while the posterior is rounded, targeting upwards and backwards. Its spongy nature and reddish-purple appearance are attributed to intense vascularization. The structure is comprised of both red and white pulp, each playing crucial roles in filtering blood, immune response, recycling iron, storing blood, and extramedullary hematopoiesis. It is linked to the stomach and kidney through parts of the greater omentum, namely the gastrosplenic and splenorenal ligaments, and its principal venous drainage is provided by the splenic vein, which travels behind the pancreas before joining.
Spinal cord	<i>Def</i> : Originating at the lower part of the brainstem, specifically the medulla oblongata, this structure extends down to the lower back, terminating in a cone-shaped end known as the conus medullaris. It is positioned from the topmost neck bone, the C1 vertebra, down to roughly the L1 vertebra at the upper portion of the lower back, just beneath the ribcage. Measuring around 18 inches (45 centimeters) in length, its cylindrical form encompasses a collection of nerve fibers safeguarded within the vertebral column. Segmented with pairs of roots (dorsal and ventral), these join to form the spinal nerves, while its composition includes an external white matter layer surrounding an internal gray matter core. This organ is encased by the central nervous system's three protective membranes: the dura mater, arachnoid, and pia mater, further shielded by the vertebral column's bony architecture. As an essential component of the central nervous system, it serves as the primary conduit for signaling between the brain and the body, as well as the site for initiating reflexes and processing sensory information, closely associated with the spinal nerves emerging at each of its segments.
Stomach	<i>Def</i> : Positioned to the left of the midline and centrally in the upper abdomen area, this J-shaped organ exhibits a lesser and greater curvature, with its anterior and posterior surfaces smoothly coated by peritoneum. Residing primarily in the epigastric and umbilical regions, its size, shape, and position exhibit variability among individuals and change with position and respiration. This hollow, muscular structure can significantly vary in its capacity, designed to store food temporarily. It comprises four main regions: the cardia, fundus, body, and pylorus, with the fundus being the rounded area adjacent to the cardia and the body constituting the largest portion. It can expand or contract, featuring numerous folds (rugae) when empty that smooth out when distended. A dense layer of small gastric glands within the mucous-membrane lining secretes enzymes and hydrochloric acid for the partial digestion of proteins and fats. It consists of layers including mucosa, submucosa, muscularis externa, and serosa, adapting its shape and size based on its contents. Located between the esophagus and the duodenum, and resting below the diaphragm as part of the gastrointestinal (GI) tract, its positions are explored through radiology and endoscopy, revealing its spatial differences and general appearance. This organ is instrumental in the initial stages of digestion, its structure finely tuned for effective performance.